

ESD-TR-77-71

ESD ADVISORY BOARD

DRI Cell No. 87416

Copy No. 1 of 2 cys.

Semiannual Technical Summary

Seismic Discrimination

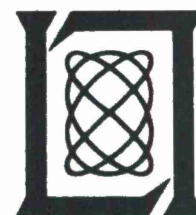
31 March 1977

Prepared for the Defense Advanced Research Projects Agency
under Electronic Systems Division Contract F19628-76-C-0002 by

Lincoln Laboratory

MASSACHUSETTS INSTITUTE OF TECHNOLOGY

Lexington, Massachusetts



Approved for public release; distribution unlimited.


The work reported in this document was performed at Lincoln Laboratory, a center for research operated by Massachusetts Institute of Technology. This research is a part of Project Vela Uniform, which is sponsored by the Defense Advanced Research Projects Agency under Air Force Contract F19628-76-C-0002 (ARPA Order 512).

This report may be reproduced to satisfy needs of U.S. Government agencies.

The views and conclusions contained in this document are those of the contractor and should not be interpreted as necessarily representing the official policies, either expressed or implied, of the United States Government.

This technical report has been reviewed and is approved for publication.

FOR THE COMMANDER


Raymond L. Loiselle, Lt. Col., USAF
Chief, ESD Lincoln Laboratory Project Office

Non-Lincoln Recipients

PLEASE DO NOT RETURN

Permission is given to destroy this document
when it is no longer needed.

MASSACHUSETTS INSTITUTE OF TECHNOLOGY
LINCOLN LABORATORY

SEISMIC DISCRIMINATION

SEMIANNUAL TECHNICAL SUMMARY REPORT
TO THE
DEFENSE ADVANCED RESEARCH PROJECTS AGENCY

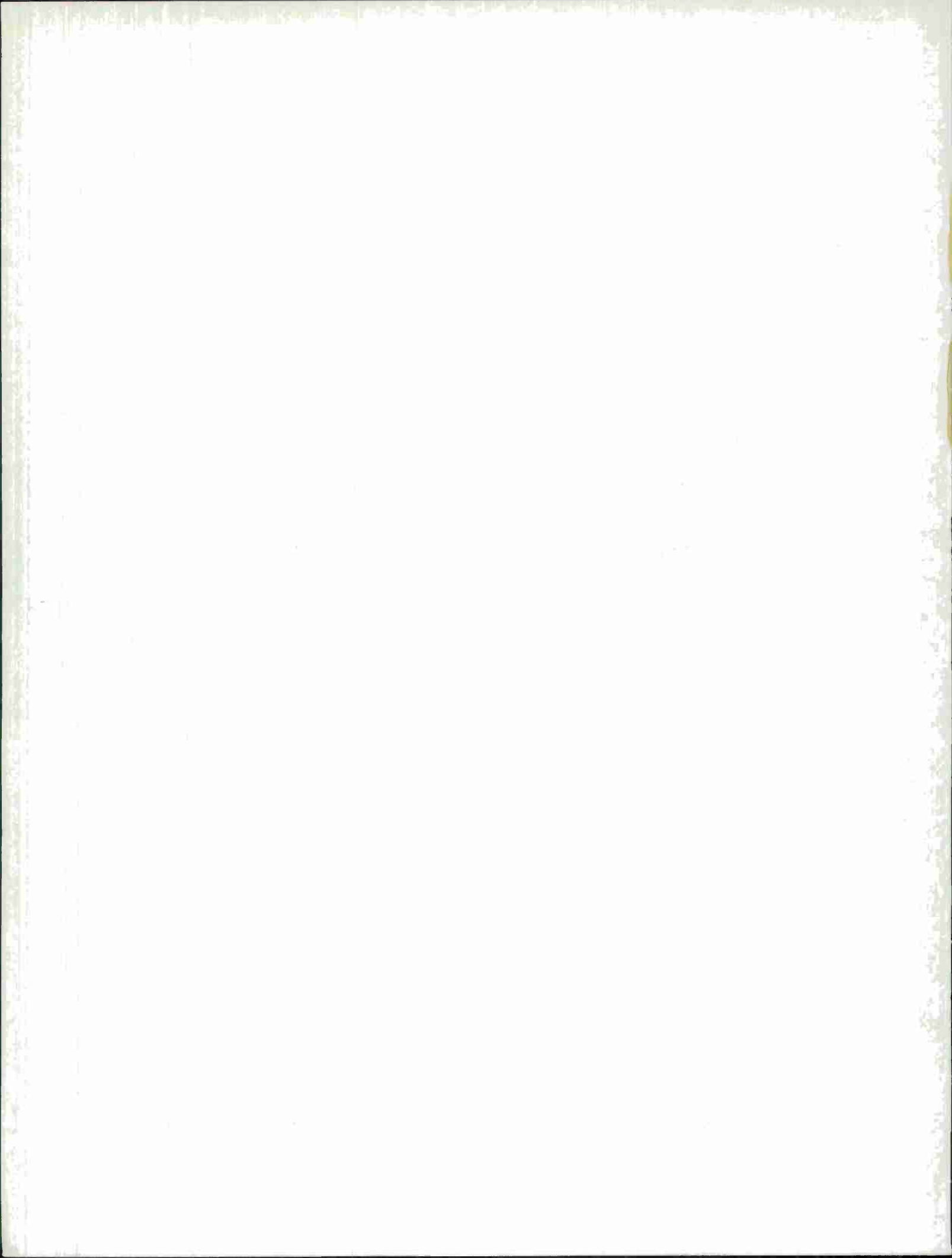
1 JULY 1976 - 31 MARCH 1977

ISSUED 7 JULY 1977

Approved for public release; distribution unlimited.

LEXINGTON

MASSACHUSETTS



ABSTRACT

This report describes 31 investigations in the field of seismic discrimination. These are grouped as follows: body-wave studies (6 contributions), surface-wave studies (5 contributions), studies of long- and short-period magnitude, explosion yield, and seismic energy (9 contributions), miscellaneous studies (9 contributions), and recent developments in our data and computer systems (2 contributions).

CONTENTS

Abstract	iii
Summary	vii
 I. BODY-WAVE STUDIES	 1
A. Short-Period P-Waveforms from Large Events Recorded at SRO Sites	1
B. P-Wave Travel-Time Anomalies and Gravity Anomalies in a Study of the Upper Mantle Beneath the United States	1
C. Travel-Time Residuals for P Phases: A Search for Source Anomalies	2
D. <u>In Situ</u> Compressional Velocities: Refinements to the Inversion Scheme and an Evaluation of Station-Source Bias	4
E. <u>In Situ</u> Ratios of Compressional-to-Shear Velocity in Shallow- and Deep-Source Regions	7
F. A Moment-Tensor Representation of Body-Wave Displacement Vectors on the Focal Sphere	9
 II. SURFACE-WAVE STUDIES	 21
A. An Efficient Algorithm for Determining Phase and Group Velocities of Surface Seismic Waves	21
B. Group-Velocity Measurements Across Eurasia from Mashad SRO	22
C. Group-Velocity Dispersion Measurements at Near-In Distances	23
D. A Rayleigh-Wave Structure for Novaya Zemlya	25
E. Pure Path Dispersion of Overtones of Surface Waves	28
 III. MAGNITUDE, YIELD, AND ENERGY	 41
A. Azimuthal P-Wave Amplitude Variations from Large Explosions	41
B. Seismic Scaling Information from SRO Data	42
C. A Rapid and Inexpensive Procedure for Measuring the Response of the WWSSN SP Instrument	43
D. Estimation of Station Detection Characteristics from Bulletin Data	44
E. Computer Simulation of Network Performance	46
F. An Application of the Energy-Moment Tensor Relation to Estimation of Seismic Energy Radiated by Line Sources	47
G. Rayleigh-Wave Explosive Moments and Seismic Energies for Six U.S. Explosions	51
H. Yield Verification Using Long-Period P Waves from Explosions	55
I. Anomalous m_b vs Yield for Longshot, Milrow, and Cannikin	57

IV. MISCELLANEOUS STUDIES	79
A. Multiple-Channel Maximum-Entropy Spectra	79
B. A Multiple Event at Semipalatinsk	81
C. Splitting of the pP Phase from Suboceanic Events	83
D. Polarization Filtering of Long-Period SRO Data	86
E. An Exact Solution to the Problem of Excitation of Normal Modes by a Propagating Fault	88
F. Dissipation of Shear and Compressional Energy in the Mantle from Normal-Mode Data	90
G. Velocity-Dispersion Kernels for Frequency-Dependent Q	92
H. Finite-Strain Earth Model with Consideration of Velocity Dispersion Due to Anelasticity	94
I. Correlation of Seismic Activity with Changes in the Rate of Rotation of the Earth	99
V. DATA SYSTEMS	123
A. PDP-11 Computer Facility	123
B. Interactions with the Datacomputer	125
VI. PUBLICATIONS LIST	127
Glossary	129

SUMMARY

This is the twenty-sixth Semiannual Technical Summary report describing the activities of Lincoln Laboratory, M.I.T., in the field of seismic discrimination. Due to the recent change in fiscal year, this report covers the period 1 July 1976 to 31 March 1977. The objective of the Lincoln Laboratory program is to carry out fundamental research into the seismological problems associated with the detection, location, and identification of earthquakes and nuclear explosions, and with the estimation of explosion yields. In order to investigate these problems, we are continuously improving our ability to manipulate and process seismic data from a global network of high-quality digital stations and arrays.

During the period covered by this report, data have become available from the first Seismic Research Observatories (SROs). At the time of writing, data are being received on a routine basis from six of these stations: ANMO (Albuquerque), MAIO (Mashad), GUMO (Guam), NWA0 (Australia), SNZO (New Zealand), and TATO (Taiwan). Fairly extensive data are now available for the first three of these, and several contributions in this report describe our first attempts to use these new data for seismological research. The quality of these data is very high, and we expect them to make a major impact on seismology as more stations become operational.

In the area of general body-wave studies, several investigations are described in this report. We note the presence of small emergent phases ahead of larger, more-impulsive phases in many cases of shallow earthquakes, using the short-period (SP) SRO data. This clearly complicates the selection of onset times from conventional WWSSN film-chip data. Other studies have used P-wave travel times to investigate the variation in crust and upper-mantle structure across the United States, and to determine velocities in the source region by a master event technique. It appears possible to directly measure P- and S-wave velocity in source areas such as downgoing lithosphere slabs, and make conclusions about anomalous zones within these slabs. Earlier work on the representation of the seismic source by the moment tensor has been extended to body-wave sources.

Surface-wave studies described include a new rapid algorithm for the determination of group and phase velocity, a series of observations of Rayleigh-wave dispersion at the Mashad SRO, and a determination of structure in the Novaya Zemlya area using a pair of events. In another study, observations of NTS explosions at Albuquerque SRO are analyzed for group velocity dispersion using a data adaptive prediction error algorithm. A study of surface-wave overtones is also included, and a technique is described for the problem of mode separation.

A series of investigations continuing our research into the determination of magnitude and yield are described. A study of the variation with azimuth of the long-period (LP) P-wave amplitudes from two explosions shows features that are consistent with an earlier study of station magnitude bias using short-period data. An initial application of SRO data to the problem of seismic scaling, and a new technique for measuring the amplitude and phase response of the WWSSN SP instrument are described. We have continued our investigation of methods for the determination of station-detection characteristics. We are particularly concerned about the inclusion of saturation parameters, and the proper evaluation of the parameters describing seismicity. A series of stations with known parameters are then used as a model of a global network, and a synthetic earthquake catalog for the network has been generated using a simulation program. A theoretical development describes how the seismic energy radiated by a

finite propagating line source can be evaluated using the moment tensor formulism, and a similar approach is used to calculate the explosive moments and radiated Rayleigh-wave energies for a set of U.S. explosions. In another study, the LP P-waves observed from Longshot, Milrow, and Cannikin are compared with observed SP data. It appears that LP data may provide a much more stable measure of yield.

A wide variety of miscellaneous studies is included. These range from an extension of maximum entropy spectral analysis to the study of multichannel cross spectra, to studies of Q structure in the earth. Cepstral analysis is applied to an event near Semipalatinsk, and it is shown to be a multiple event. An attempt to use the same analysis to detect the splitting of the pP phase due to double reflection in oceanic areas is described. The application of polarization filtering to LP SRO data is discussed, and it appears to be a promising technique for separating interfering phases. A theoretical development for the excitation of normal modes by a propagating fault is included. The determination of the dissipation parameter Q is of considerable current interest. Direct measurement of Q for a number of normal modes of the earth is outlined, and the effects of a frequency-dependent Q on velocity dispersion are discussed. An attempt at carrying out a simultaneous inversion of normal-mode data to obtain both elastic and inelastic parameters is described, using finite strain theory. A possible correlation between variations in the level of seismic activity with time and changes in the rate of rotation of the earth is discussed.

We continue to develop our data-handling facilities. Our PDP-11 system is now a general-purpose time-sharing facility, and we are building up our applications software library for seismic research. The system allows us to connect with the ARPANET, to larger computers, and to the datacomputer. Interaction with the datacomputer using newly developed software is increasing.

M. A. Chinnery

SEISMIC DISCRIMINATION

I. BODY-WAVE STUDIES

A. SHORT-PERIOD P-WAVEFORMS FROM LARGE EVENTS RECORDED AT SRO SITES

As part of an evaluation of the SRO system, a study has been made of short-period (SP) P-waveforms recorded at SRO sites from large ($m_b \geq 5.6$) events during January and February 1976. The stations operating at this time were ANMO (Albuquerque), MAIO (Mashad), and GUMO (Guam). The data quality at ANMO and MAIO is generally excellent, but at GUMO extremely high noise levels (predominant period ~ 1 sec, amplitude frequently exceeding 100 $m\mu$) severely degrade recording capability. Noise levels at ANMO and MAIO appear to be generally less than 2 $m\mu$ in the SP band.

This difference in noise levels is reflected in the detection capability of the stations. The SP data are saved only when triggered by the detection algorithm. There were 55 events of $m_b \geq 5.6$ during the first 2 months of 1976: restricting observations to only events of $20^\circ \leq \Delta \leq 100^\circ$, the number of these which should have been detected at ANMO, MAIO, and GUMO were 20, 19, and 33, respectively. Actual detections were 19, 17, and 9, discarding periods during which the stations were not operating (3 days at ANMO, 6 at MAIO, 0 at GUMO). The above give detection rates for events of $m_b \geq 5.6$ of 95 percent at ANMO, 89 percent at MAIO, and a distressingly low 27 percent at GUMO.

The nature of the waveforms recorded is also of interest. Figure I-1 shows P-waves [(1) - (20)] recorded at the SRO sites from sources of varying source depth, distance, and size. Waveforms from deep ($h \geq 70$ km) earthquakes [(1) - (7)] all have extremely sharp and impulsive onsets. Those from shallow events often show a small emergent phase up to 4 sec prior to a more impulsive larger arrival [(8), (12), (14), (15), and (19)]. The larger arrival is probably the stopping phase, which occurs virtually simultaneously on the edges of the fault plane; the smaller precursive arrival is due to the onset of faulting at a point of nucleation.

Previous work at Lincoln Laboratory¹ attempted to predict such complicated waveforms on WWSSN records using a Savage-type source;² the advent of the SROs gives us a high-quality digital dataset which we intend to test against the source model. An interesting feature of these complicated waveforms is that the gradual onset may frequently be masked by noise, and that time picks made from such data may consequently often be in error by several seconds.

R.G. North

B. P-WAVE TRAVEL-TIME ANOMALIES AND GRAVITY ANOMALIES IN A STUDY OF THE UPPER MANTLE BENEATH THE UNITED STATES

According to recent studies,³⁻⁵ gravity anomalies in the wavelength range of 500 to 2000 km may well be due to lateral inhomogeneities in density, to depths of a few hundred kilometers. On the other hand, the analysis of station anomalies for body-wave travel times on a similar scale^{6,7} shows that the corresponding velocity anomalies must originate deeper than in the crust.

This study is part of a more extensive project attempting to correlate gravity data and body-wave travel-time data in relation to the structure of the upper mantle beneath the continental United States.

In order to invert travel times for P-velocity structure, the upper mantle of the U.S., to a depth of 800 km, was divided into $5^\circ \times 5^\circ$ blocks of adjustable thickness, and a selection of P-wave travel-time data was made so as to optimize the sampling of these blocks by the corresponding rays. From the ISC catalogs for the years 1964 to 1973, 102 seismic stations were selected in the U.S. and southern Canada, on the basis that they reported more than 200 events in that period of time. Then 2653 events were chosen, using the following criteria:

Magnitude $m_b \geq 5.8$, event observed by at least 50 stations in the world

Event observed by at least 15 North American stations (in order to remove the source effect, common to all stations), in the distance range of 30° to 100°

Accurate location of epicenter

standard error in latitude $\leq 0.05^\circ$

standard error in longitude $\leq 0.06^\circ$

No further constraints on focal depth or origin time determination, as these effects are common to all stations.

The travel-time anomalies were then computed, as referred to two different laterally homogeneous models: Jeffreys-Bullen,⁸ and "PEM" of Dziewonski, Hales, and Lapwood.⁹ Anomalies of magnitude greater than ± 2 sec were considered as bad readings and rejected. Then, the station anomalies were computed by taking out the average over all stations for each particular event.

For each station, an analysis was made of the dependence of the anomaly on azimuth from station and on distance from station to event. For that purpose, the anomalies were averaged over azimuth ranges of 45° and distance ranges of 10° . As expected from previous studies,⁷ three major regions can be distinguished in the U.S. [see Figs. I-2(a) and (b)]: strongly positive anomalies in the west, strongly negative in the center, and a more complicated pattern in the east.

By drawing profiles across aligned stations and comparing the azimuthal dependence between stations on a profile, one can attempt to put some bounds on the depths and locations of the velocity anomalies.

NW-SE and W-E profiles across western and central U.S. suggest depths as large as 600 to 700 km for the large fast anomaly in the central U.S., shallower and weaker towards the east, and extending south into the Gulf of Mexico.

The next step in this study is to perform the mathematical inversion¹⁰ of these travel-time anomalies for velocity structure and relate them to the gravity data and density structure.

B. A. Romanowicz

C. TRAVEL-TIME RESIDUALS FOR P PHASES: A SEARCH FOR SOURCE ANOMALIES

P and S velocities in mantle seismic zones are anomalously high by 6 to 7 percent when averaged over nearly the entire length of the Japanese zone¹¹ or the Tonga Zone.^{12,13} There is a growing need to know how this anomaly is distributed along the slab-like bodies containing the seismic earthquakes, and whether or not the anomaly exists below the depth of the deepest earthquakes. This depth varies between 650 and 700 km for the deepest zones.

In situ P-wave velocities reported in Fitch^{14,15} and in this SATS show that positive anomalies as large as 10 percent exist in the region of the deepest mantle earthquakes. In contrast, no significant anomaly was resolved in the depth range from 450 to 550 km in the Tonga Zone. Fitch¹⁵ suggested that the deep positive anomaly resulted from an elevated "650 km discontinuity," a major transition zone that can be taken as the boundary between the upper and lower mantles. If this interpretation were correct, then the deepest earthquakes would be below the top of this transition zone and thus in the lower mantle. The question to be resolved is whether or not the anomalous material containing the mantle earthquakes descends to great depth into the lower mantle, albeit without seismic activity.

The seismological approach to this problem has been to analyze travel-time residuals. Jordan and Lynn¹⁶ and Engdahl¹⁷ reported residuals of ScS and P times, respectively, that could be explained by lithospheric material that had descended into the lower mantle. More recently, Jordan¹⁸ has proposed the existence of a slab-like body extending to possibly 1000 km beneath the sea of Okhotsk. He analyzed residuals of S, ScS, and ScS-S times from one deep earthquake.

We have begun a study similar to Jordan's; however, our data are the times of P phases reported in the Bulletin of the International Seismological Center (ISC). This data base includes times for the years 1964 through 1973. Because most deep seismic zones are nearly linear for distances of more than 1000 km along the strike of the various island arcs, residuals from each zone can be superposed on a single focal sphere as was done for the Tonga earthquakes in Figs. I-3(a) through (c). About 40,000 residuals are represented in these figures. The residuals were computed with the J-B tables as a standard, and have been averaged in blocks of 5° in azimuth by 5° in angle of incidence. Raw residuals were adjusted for station bias and the Earth's ellipticity by using the results in Sengupta and Julian¹⁹ and Dziewonski and Gilbert,²⁰ respectively. Most of these station corrections lie in the range ±1 sec, whereas ellipticity corrections tend to make the raw residuals more negative because the source region is closer to the equator than to the pole.

Figure I-3(a) shows a band of negative residuals that has an orientation consistent with a seismic zone inclined between 30° and 40° toward the west (the overall strike of the seismic zone is shown by the heavy bars in these diagrams). The minimum residual is -3 sec and the average negative residual in this band is between -1.5 and -2.0 sec.

The path length for rays in the anomalous body can be crudely estimated from the equation

$$\langle \Delta T \rangle = \frac{-f_v d}{\langle v \rangle (1 + f_v)}$$

where $\langle \Delta T \rangle$ is the average travel-time residual corrected for all but the source effect, f_v is the fractional velocity anomaly, $\langle v \rangle$ is the average velocity for the depth range d in the anomalous body. Taking -1.75 sec to be the corrected average residual from the shallow earthquakes, an average v_p of 8.5 km/sec for the upper part of the slab and a velocity anomaly of 6 percent yield a path length of about 260 km, which is less than 1/2 the length of the inclined seismic zone.

Residuals from earthquakes in the depth range from 200 to 400 km [Fig. I-3(b)] and from depths greater than 550 km [Fig. I-3(c)] within the same seismic zone show negative residuals

as large as -2 sec that map onto the same region of the focal sphere occupied by the band of negative residuals in Fig. I-3(a). The mean negative residual in this region of the focal sphere is about -1.0 . An average velocity anomaly of $+10$ percent in the depth range 550 to 600 km can account for a travel-time residual of -1 sec; however, this comparison of the residual pattern for near-surface and deep events may not be valid because of a steepening of the seismic zone at depths greater than about 400 km. Little evidence for such steepening can be inferred from these residual maps. Estimates of absolute time residuals are required in order to place more accurate bounds on the velocity anomalies from deep earthquakes. Similar analyses will be carried out for the other mantle earthquake zones to show to what extent the anomaly pattern for the Tonga-Fiji region is typical of such zones.

T. J. Fitch
A. M. Dziewonski

D. IN SITU COMPRESSIONAL VELOCITIES: REFINEMENTS TO THE INVERSION SCHEME AND AN EVALUATION OF STATION-SOURCE BIAS

Arrival-time differences between a master and a number of secondary events can be simultaneously solved for the relative locations, in situ seismic velocities, and the direction cosines for ray paths at the focus of the master.¹⁴ In contrast to many problems in geophysics, this one contains a set of model parameters that is completely known a priori, although the data may be able to resolve only a small subset of these parameters.

In Fitch,¹⁴ direction cosines pertaining to the azimuths of the ray paths were taken to be those of the great-circle paths, and cosines pertaining to the angles of incidence were refined only for paths that lay almost completely in the upper mantle. In situ V_p 's 5- to 10-percent higher than global average velocities for the corresponding depth ranges were computed for three groups of deep earthquakes. Ray paths that lay primarily in the lower mantle and core were defined by ray parameters computed from the classical earth model of Jeffreys²¹ or the modern models B1 by Jordan and Anderson²² and the Parameterized Earth Model (PEM) of Dziewonski *et al.*⁹ In subsequent work, the classical model was used exclusively because the bias imposed by a particular model was no more than a few percent in velocity.

Fitch¹⁵ showed that in the depth range from 450 to 650 in the Tonga seismic zone, in situ V_p is anomalously high only at depths greater than 550 to 600 km. These results have now been confirmed with improved data sets and damped least-square solutions^{10,23,24} akin to a stochastic inverse proposed by Franklin²⁵ and Jordan and Franklin.²⁶

The P arrival times were taken from the Bulletin of the ISC. Chi-square tests of the residuals of the differential times are consistent with standard deviations of about 0.6 sec, when grossly incorrect times are eliminated. The corresponding errors in the individual arrival times are about 0.4 sec. Solutions with synthetic data consistent with the J-B travel times, actual station-source configurations, and the above-mentioned level of uncertainty show that the separations between master and secondary events should be no less than about 30 km and no more than about 100 km to be reasonably confident that the computed in situ V_p lies within two standard deviations of the correct value. The latest compilation of P times from the Tonga seismic zone (carried out while the author was still at the Australian National University) reduced the largest separation between master and secondary earthquakes to about 100 km for each of the stable solutions in Table I-1.

TABLE I-1 COMPARISON OF OBSERVED AND CALCULATED VELOCITIES				
Depth of Master Earthquake (km)	Largest Separation from Master (km)	V_p from Synthetic Data (km/sec)	V_p from Real Data (km/sec)	V_p from Jeffreys ²¹ (km/sec)
493	102	9.4 ± 0.2	9.7 ± 0.2	9.60
520	92	Unstable	Unstable	9.76
535	75	10.1 ± 0.2	9.4 ± 0.2 (marginally stable)	9.88
572	126	9.8 ± 0.2	Unstable	10.09
597	93	9.9 ± 0.2	10.7 ± 0.2	10.23
608	144	Unstable	Unstable	10.29
624	107	10.2 ± 0.2	10.7 ± 0.2	10.37
650	91	9.8 ± 0.2	11.2 ± 0.2	10.47

These solutions include refined estimates of the azimuths as well as the angles of incidence for ray paths to the stations shown in Fig. I-4. Rather than a simple least-squares solution that minimizes $|b - Ax|^2$ where x and b are the data and model vectors, respectively, and A is the matrix of partial derivatives, these solutions were damped by the addition of a small component to the diagonal elements of the solution matrix. This is equivalent to minimizing $|b - Ax|^2 + \Theta^2 x^2$, where Θ^2 is the vector containing the damping coefficients. Following Aki et al.¹⁰ these coefficients were initially set equal to σ^2/σ_x^2 , where σ^2 is the variance of the random errors in the data, and the σ_x^2 are estimates of the variance in the model parameters. To achieve more rapid convergence to a solution, the initial damping coefficients were multiplied by 0.1.

Damped solutions are preferred to the simple solutions because more rigorous account is taken of errors in the data that inevitably limit the resolution of the model parameters. The least-resolved parameters are the angles defining the direction cosines and the separation between events. The in situ velocity in all cases was resolved to greater than 95 percent.

Solutions with synthetic data reveal a bias in the in situ velocities that is imposed by the particular station-source configuration in the real earth. This bias was thought to be negligible in Fitch;¹⁵ however, the results in Table I-1 and Fig. I-5 show that this bias could be as great as 5 percent for these particular data sets. The in situ velocities pertaining to the master earthquakes at depths of 650 and 597 km are significantly less than the corresponding Jeffreys velocities in the solutions with synthetic data, and greater in the solutions with real data. The bias in the solutions with synthetic data results from the locations of these master earthquakes which are below all of their secondary events (Fig. I-5).

The higher velocities computed with the real data cannot be explained by station-source bias. Consequently these solutions, as well as less-sophisticated solutions reported by Fitch,^{14,15} reveal a positive velocity anomaly near the base of this mantle seismic zone. The highest in situ velocity was computed for a group of events with the master at 650 km, which is

TABLE I-2
STRUCTURE-DEPENDENT RAY PATHS†

Azimuth (deg)		Angles of Incidence (deg)		
	JB	Refined	Jeffreys ²¹	Refined
AFI				
493	37.2	39.2 ± 4.7 (0.859)	75.2	75.3 ± 5.3 (0.765)
597	58.3	58.8 ± 6.0 (0.830)	109.6	128.2 ± 5.8 (0.903)
624	60.3	43.1 ± 3.1 (0.940)	107.7	121.1 ± 5.4 (0.618)
650	46.1	46.0 ± 4.9 (0.873)	96.8	109.5 ± 4.6 (0.876)
GNZ				
493	186.4	189.4 ± 6.6 (0.710)	73.8	79.3 ± 5.7 (0.705)
597	187.9	183.6 ± 6.7 (0.552)	67.4	66.8 ± 6.5 (0.709)
624	186.4	199.1 ± 3.3 (0.767)	69.2	66.2 ± 7.1 (0.907)
WEL				
493	193.5	202.5 ± 6.5 (0.981)	66.9	69.7 ± 5.4 (0.952)
624	191.5	197.1 ± 3.7 (0.779)	65.8	60.9 ± 7.5 (0.924)
650	192.9	187.8 ± 5.1 (0.236)	64.0	83.2 ± 5.0 (0.773)
RAO				
493	157.5	156.0 ± 4.8 (0.886)	122.6	109.2 ± 5.8 (0.851)
597	177.8	162.0 ± 7.9 (0.894)	92.7	88.3 ± 5.8 (0.947)
650	172.3	185.0 ± 5.8 (0.876)	112.2	124.6 ± 5.2 (0.955)
† Corresponding diagonal element of the resolution matrix is given in parentheses.				

nominally the depth of a major transition zone between the upper and lower mantles. The PEM velocities in Fig. I-5 illustrate the size of the velocity contrast that is consistent with a combination of seismological and petrological prejudice.

By definition, deep earthquakes occur in anomalous mantle. A map view of the Tonga deep seismic zone is shown in Fig. I-6 along with the epicenters of the master earthquakes. A significant fraction of the paths to the stations AFI, RAO, GNZ, and WEL (Fig. I-4) lie within or closely parallel the seismic zone and thus are expected to show the greatest deviations from the paths predicted by symmetrical earth models.

In Table I-2 the refined azimuths that differ from the predicted azimuths by more than one standard deviation (underscored in the table) reveal rotations of ray paths toward the strike of the seismic zone. (The azimuth for the path WEL650 is an apparent exception; however, it is essentially unresolved by the data.) Similarly the angles of incidence from the deeper master earthquakes to AFI (Fig. I-4) are rotated toward the upward vertical, and thus a larger fraction of the corresponding ray paths will lie in the seismic zone.

Taken together, the in situ velocities and the direction cosines for ray paths to the closer stations are consistent with other seismological and geophysical evidence for a body of anomalous material containing mantle earthquakes. However, the in situ velocities show that the velocity anomaly associated with this body is not uniformly distributed in the depth range from 450 to 600 km. One way to explain the anomaly pattern is by an elevated 650-km discontinuity as proposed in Fitch.¹⁵

T. J. Fitch

E. IN SITU RATIOS OF COMPRESSIONAL-TO-SHEAR VELOCITY IN SHALLOW- AND DEEP-SOURCE REGIONS

The seismic velocities V_p and V_s and their ratio are being reported in many studies both within and outside the Earth's major earthquake zones. The inferred velocities or velocity ratios are, in almost every case, based on less than ten arrival times of the P and S phases from a single event. These inferences from such a limited data set are vulnerable to various pathologies that may exist within an active fault zone or between the source region and the receivers.²⁸ For example, anomalously high attenuation of weak signals may lead to arrival times which are picked systematically late, and thus anomalously low velocities, or S-to-P conversions, may be misinterpreted as the S phase, in which case the inferred shear velocity will be too fast.

A major advantage of the inversion scheme proposed by Fitch and Rynn²⁹ and promoted here is that the velocity ratio is computed from a large data set. Several hundred arrival times from 10 to 15 events are simultaneously inverted for relative locations and elevation angles for ray paths, as well as the velocity ratio. With such a data set, large reading errors contained in a subset of the data are likely to be discovered. Other advantages of this scheme are that the velocity ratio pertains to the source region and, in principle, does not require any knowledge of the velocity structure outside that region.

The inversion scheme reported by Fitch and Rynn²⁹ is generalized so that P and S waves traveling between each source and receiver are represented by independent ray paths. Resolution must be sacrificed to achieve this generalization for the case of data from crustal earthquakes that are only locally recorded. The loss of resolution occurs mainly in the relative depths and in the direction cosines for ray paths at the focus of the master earthquake. V_p/V_s

TABLE I-3
A SAMPLE SOLUTION

Secondary Event No.	Differential Origin Time (sec)	Relative Locations of Secondary Events		
		Distance (km)	Azimuth (deg)	Elevation Angle (deg)
1	10.04 ± 0.03	1.06 ± 0.15	41.64 ± 4.58	62.62 ± 8.59
2	10.02 ± 0.03	0.87 ± 0.16	27.35 ± 5.73	58.74 ± 8.02
3	10.47 ± 0.02	1.83 ± 0.14	174.81 ± 4.58	142.33 ± 2.86
4	10.15 ± 0.02	1.05 ± 0.09	344.86 ± 6.30	108.42 ± 8.02
5	10.49 ± 0.02	1.77 ± 0.14	171.79 ± 4.01	133.92 ± 2.86
6	10.02 ± 0.02	2.04 ± 0.15	30.22 ± 3.44	53.69 ± 3.44
7	10.11 ± 0.03	1.47 ± 0.12	2.51 ± 4.01	83.56 ± 6.30
8	10.33 ± 0.02	1.06 ± 0.13	146.50 ± 7.45	135.95 ± 4.58
9	10.02 ± 0.02	1.65 ± 0.14	30.39 ± 2.86	58.28 ± 3.44
10	9.99 ± 0.02	1.06 ± 0.11	116.50 ± 6.88	36.18 ± 5.16
11	10.27 ± 0.02	1.08 ± 0.07	39.15 ± 5.16	131.16 ± 8.59
12	10.45 ± 0.02	1.55 ± 0.11	166.02 ± 4.01	117.93 ± 4.01
13	9.99 ± 0.02	2.02 ± 0.14	25.78 ± 2.86	52.88 ± 2.86
Station	Ray-Path Elevation Angles†			
	Initial V_p/V_s (deg)	Refined V_p/V_s (deg)		
		P Wave	S Wave	
LIV	168	165.88 ± 3.95	170.54 ± 4.52	
TAB	156	155.84 ± 2.87	166.16 ± 3.04	
DAM	155	157.81 ± 2.67	158.64 ± 2.80	
ORV	154	155.05 ± 2.02	156.45 ± 2.18	
BID	143	141.86 ± 5.00	—	
WYN	140	141.61 ± 7.34	122.23 ± 6.57	
LON	136	120.38 ± 5.07	—	
CAM	137	133.55 ± 4.46	—	
FOR	131	141.10 ± 2.03	—	
RAT	130	136.74 ± 4.52	126.29 ± 4.32	
FIG	127	128.15 ± 5.45	124.12 ± 8.19	
KAT	120	128.92 ± 4.46	—	
HON	114	106.07 ± 6.22	—	
STI	118	104.10 ± 4.36	—	

Initial $\sqrt{3}$.
Refined 1.60 ± 0.02 with the corresponding element of the resolution matrix 0.999.
 $\chi^2 = 105$ and $\langle \chi^2 \rangle = 149$.
71 of 74 eigenvalues retained.
† 0° is the downward vertical.

is nearly perfectly resolved in solutions with real and synthetic data of high quality, i.e., arrival times with random errors no larger than, say, 0.05 sec. Several data sets, each containing between 200 and 300 arrival times, were compiled from the better-recorded earthquakes in the NW corner of the aftershock zone of the 1 August 1975 Oroville, California earthquake.

The preferred estimate of *in situ* V_p/V_s lies in the range 1.65 to 1.60, which is significantly less than 1.70 — the ratio assumed by the Office of Earthquake Research at Menlo Park, California for computing the absolute locations of these events. The solution summarized in Table I-3 is typical. The data for this solution come from a source region that is annular in shape, with the master located in the center. The inner radius of about 1 km is limited by the errors in reading arrival times, and the outer radius is limited by the condition that the separation between master and secondary events be small by comparison with the length of the ray path to the nearest station (Fig. I-7). The standard errors in high-quality P and S times were found to be between ± 0.01 to ± 0.02 sec and between ± 0.03 to ± 0.04 sec, respectively. These levels of uncertainty are consistent with chi-square tests on residuals of the differential P and S times.

The relative locations projected on a focal mechanism solution for the main shock (Fig. I-8) define a broad band from north to south between the nodal planes. The relative locations pertain to activity near the base of the aftershock zone at a depth between 8 and 10 km. Apparently, in this depth range the seismic zone has nearly the same strike as shallower parts of the zone, but is inclined nearly vertically. This can also be seen in the vertical distribution of aftershocks reported by Lahr *et al.*³⁰

The stability of the inversion scheme increases as the distance between master and secondary events increases. However, these distances must be sufficiently small to avoid making assumptions about the geometry of the ray paths outside the source region. Larger source regions are permitted at greater depth; consequently, the inversion scheme becomes a more robust estimator of the velocity ratio as source depth increases. This is demonstrated by solutions with synthetic data from a hypothetical source region centered at a depth of 100 km.

Computations reported here were carried out at the computer center of the Australian National University.

T. J. Fitch
A. G. Lindh†

F. A MOMENT-TENSOR REPRESENTATION OF BODY-WAVE DISPLACEMENT VECTORS ON THE FOCAL SPHERE

Presently two point-source moment-tensor representation theorems exist; the original free oscillation expansion by Gilbert,³¹ and the Love- and Rayleigh-wave expansion done by McCowan.³² The advantages to the moment-tensor approach are well known. These expansions represent nonpropagating point sources in their most general form, including all three possible mechanisms: explosive, double couple, and compensated linear vector dipole. Furthermore, the resulting vector displacement is always a linear combination of the moment-tensor elements thereby making the determination of an unknown source mechanism amenable to linear-estimation theory. The purpose here is to extend the moment-tensor formulation to body-wave displacement vectors on the focal sphere.

The problem is solved in spherical coordinates using the geometry shown in Fig. I-9. The source is assumed to act at the center of a homogeneous elastic solid where it is described by the fixed Cartesian coordinate system (x,y,z) with associated unit vectors ($\hat{i}, \hat{j}, \hat{k}$). The displacement vector resulting from this source at a distance r from the origin oriented at the angles

† National Center for Earthquake Research, USGS, Menlo Park, CA.

Θ and φ from the source coordinate system will be represented by its radial, polar, and azimuthal components: s_r , s_Θ , and s_φ with respect to the unit vectors \hat{l}_r , \hat{l}_Θ , \hat{l}_φ . Then the usual arguments lead to the point-source moment-tensor solution:

$$\vec{s}(\vec{r}) = \left[\frac{\partial G(\vec{r}, \vec{r}')}{\partial x^i} \frac{\partial G(\vec{r}, \vec{r}')}{\partial y^j} \frac{\partial G(\vec{r}, \vec{r}')}{\partial z^k} \right]_{r'=0} \text{MA} \begin{bmatrix} 1 \\ 0 \\ 0 \\ 0 \\ 0 \\ 1 \\ 0 \\ 0 \\ 0 \\ 0 \\ 1 \end{bmatrix} \quad (\text{I-1})$$

Here, $\vec{s}(\vec{r})$ is the vector of the three displacement components mentioned above, $G(\vec{r}, \vec{r}')$ is the Green's tensor in \hat{l}_r , \hat{l}_Θ , \hat{l}_φ components (Morse and Feshbach³³), M is the source moment tensor in \hat{i} , \hat{j} , \hat{k} components, and A is the following tensor:

$$\begin{pmatrix} \sin \Theta \cos \varphi & \sin \Theta \sin \varphi & \cos \Theta \\ \cos \Theta \cos \varphi & \cos \Theta \sin \varphi & -\sin \Theta \\ -\sin \varphi & \cos \varphi & 0 \end{pmatrix}. \quad (\text{I-2})$$

The last column vector is necessary to perform the remaining indicial sum.

As shown by Morse and Feshbach³³ (Chap. 13), the Green's tensor can be decomposed into longitudinal and transverse parts which propagate P and S waves, respectively. The correct infinite domain expressions for these are, respectively,

$$\begin{aligned} L &= \frac{1}{\rho \alpha^2} \left[\left(\frac{1 + ik_\alpha R}{k_\alpha^2 R^2} \right) I - \frac{\vec{R}\vec{R}^T}{R^2} \left(\frac{3 + 3ik_\alpha R - k_\alpha^2 R^2}{k_\alpha^2 R^2} \right) \right] \frac{e^{-ik_\alpha R}}{R} \\ T &= \frac{1}{\rho \beta^2} \left[- \left(\frac{1 + ik_\beta R - k_\beta^2 R^2}{k_\beta^2 R^2} \right) I + \frac{\vec{R}\vec{R}^T}{R^2} \left(\frac{3 + 3ik_\beta R - k_\beta^2 R^2}{k_\beta^2 R^2} \right) \right] \frac{e^{-ik_\beta R}}{R}. \end{aligned} \quad (\text{I-3})$$

It is easiest to refer to Morse and Feshbach for an explanation of the symbols and conventions in these expressions. The solutions can now be obtained by substituting L and T from Eqs. (I-3) for G in Eq. (I-1) and performing the indicated operations.

After discarding the terms which decay faster than $1/r$, the following are obtained:

$$\begin{aligned} \vec{s}_P(r, t) &= \frac{P(M, \Theta, \varphi)}{2\pi \rho \alpha^3 r} \int_{-\infty}^{+\infty} i\omega g(\omega) \hat{l}^{i\omega(t-r/\alpha)} d\omega \hat{l}_r \\ \vec{s}_S(r, t) &= \frac{1}{2\pi \rho \beta^3 r} \int_{-\infty}^{+\infty} i\omega g(\omega) \hat{l}^{i\omega(t-r/\beta)} d\omega [S_\Theta(M, \Theta, \varphi) \hat{l}_\Theta + S_\varphi(M, \Theta, \varphi) \hat{l}_\varphi]. \end{aligned} \quad (\text{I-4})$$

Here α represents the P-wave velocity, β the shear-wave velocity, ρ the density, and $g(\omega)$ the source-excitation function. The angular functions are:

$$\begin{aligned}
 P(M, \Theta, \varphi) &= M_{xx} \sin^2 \Theta \cos^2 \varphi + M_{yy} \sin^2 \Theta \sin^2 \varphi + M_{zz} \cos^2 \Theta \\
 &\quad + M_{xy} \sin^2 \Theta \sin 2\varphi + M_{xz} \sin 2\Theta \cos \varphi + M_{yz} \sin 2\Theta \sin \varphi \\
 S_{\Theta}(M, \Theta, \varphi) &= \frac{M_{xx}}{2} \sin 2\Theta \cos^2 \varphi + \frac{M_{yy}}{2} \sin 2\Theta \sin^2 \varphi - \frac{M_{zz}}{2} \sin 2\Theta \\
 &\quad + \frac{M_{xy}}{2} \sin 2\Theta \sin 2\varphi + M_{xy} \cos 2\Theta \cos \varphi + M_{yz} \cos 2\Theta \sin \varphi \\
 S_{\varphi}(M, \Theta, \varphi) &= -\frac{M_{xx}}{2} \sin \Theta \sin 2\varphi + \frac{M_{yy}}{2} \sin \Theta \sin 2\varphi + M_{zz} \cdot 0 \\
 &\quad + M_{xy} \sin \Theta \cos 2\varphi - M_{xz} \cos \Theta \sin \varphi + M_{yz} \cos \Theta \cos \varphi
 \end{aligned} \tag{I-5}$$

For the case of a step-source time function $g(\omega) = -1/i\omega$, Eqs. (I-4) reduce to:

$$\begin{aligned}
 \vec{s}_P(r, t) &= \frac{P(M, \Theta, \varphi)}{\rho \alpha^3 r} \delta(t - r/\alpha) \hat{l}_r \\
 \vec{s}_S(r, t) &= \frac{\delta(t - r/\beta)}{\rho \beta^3 r} [S_{\Theta}(M, \Theta, \varphi) \hat{l}_{\Theta} + S_{\varphi}(M, \Theta, \varphi) \hat{l}_{\varphi}]
 \end{aligned} \tag{I-6}$$

As can be seen in Eqs. (I-5), an isotropic moment tensor $M = mI$ produces monopole radiation. Furthermore, a double-couple moment tensor

$$M = m(\vec{p}\vec{d}^T + \vec{d}\vec{p}^T) \tag{I-7}$$

where \vec{p} and \vec{d} are the normal and slip unit vectors, respectively, yields solutions which agree with those of Ben-Menahem and Singh.³⁴ Equations (I-5), however, are the most general solution to the point-source problem because they include all three possible source mechanisms. Extended sources may be constructed by integrating these solutions over the source volume.

D. W. McCowan

REFERENCES

1. Seismic Discrimination SATS, Lincoln Laboratory, M.I.T. (31 December 1974), DDC AD-A006194/5, and (30 June 1975), DDC AD-A014793/4.
2. J. Savage, "Radiation from a Realistic Model of Faulting," *Bull. Seismol. Soc. Am.* 56, 557-592 (1966).
3. J.G. Sclater, L.A. Lawyer, and B. Parsons, "Comparison of Long Wavelength Residual Evaluation and Free Air Gravity Anomalies in the North Atlantic and Possible Implications for the Thickness of the Lithospheric Plate," *J. Geophys. Res.* 80, 1031-1053 (1975).
4. F.M. Richter and B. Parsons, "On the Interactions of Two Scales of Convection in the Mantle," *J. Geophys. Res.* 80, 2529-2541 (1975).
5. B.D. Marsh and J.G. Marsh, "On Global Gravity Anomalies and Two Scale Mantle Convection," *J. Geophys. Res.* 81, 5267-5280 (1976).
6. A. Hales, J. Cleary *et al.*, "P Wave Station Anomalies and the Structure of the Upper Mantle," *J. Geophys. Res.* 73, 3885-3896 (1968).
7. A. L. Hales and E. Herin, "Travel Times of Seismic Waves," in *The Nature of the Solid Earth*, E.C. Robertson, Ed. (McGraw-Hill, New York, 1972).
8. H. Jeffreys and K. E. Bullen, *Seismological Tables*, reprinted 1970, London Office of the British Association.
9. A.M. Dziewonski, A.L. Hales, and E.R. Lapwood, "Parametrically Simple Earth Models Consistent with Geophysical Data," *Phys. Earth Planet. Int.* 10, 12-48 (1975).
10. K. Aki, A. Christoffersson, and E.S. Husebye, "Three-Dimensional Seismic Structure of the Lithosphere Under Montana LASA," *Bull. Seismol. Soc. Am.* 66, 501-524 (1976), DDC AD-A028458/8.
11. T. Utsu, "Anomalies in Seismic Wave Velocity and Attenuation Associated with a Deep Earthquake Zone, 1," *J. Fac. Sci. Hakkaido Univ. Jap.*, Ser. 7, 3, 1 (1967).
12. J. Oliver and B. Isacks, "Deep Earthquake Zones, Anomalous Structures in the Upper Mantle, and Lithosphere," *J. Geophys. Res.* 72, 4259 (1967).
13. W. Mitronovas and B.L. Isacks, "Seismic Velocity Anomalies in the Upper Mantle Beneath the Tonga-Kermadec Island Arc," *J. Geophys. Res.* 76, 7154 (1971).
14. T.J. Fitch, "Compressional Velocity in Source Regions of Deep Earthquakes: An Application of the Master Earthquake Technique," *Earth Planet. Sci. Ltrs.* 26, 156 (1975).
15. T.J. Fitch, "*In Situ* P-wave Velocities in Deep Earthquake Zones of the SW Pacific: Evidence for a Phase Boundary between the Upper and Lower Mantle," *Ewing Symposium*, Vol. I, AGU Monograph (1977).
16. T.H. Jordan and W.S. Lynn, "A Velocity Anomaly in the Lower Mantle," *J. Geophys. Res.* 79, 2679 (1974).
17. E.R. Engdahl, "Effects of Plate Structure and Dilatancy on Relative Teleseismic P-wave Residuals," *Geophys. Res. Lett.* 2, 420 (1975).
18. T.H. Jordan, "Lithospheric Slab Penetration into the Lower Mantle Beneath the Sea of Okhotsk," *J. Geophys.* (in press).
19. M.K. Sengupta and B.R. Julian, "P-Wave Travel Times from Deep Earthquakes," *Bull. Seismol. Soc. Am.* 66, 1555 (1976).
20. A.M. Dziewonski and F. Gilbert, "The Effect of Small, Aspherical Perturbations on Travel Times and a Re-examination of the Corrections for Ellipticity," *Geophys. J. R. Astron. Soc.* 44, 7 (1976).
21. H. Jeffreys, "The Times of P, S and SKS and the Velocities of P and S," *Monthly Notices R. Astr. Soc. Geophys. Suppl.* 4, 498 (1939).

22. T. H. Jordan and D. L. Anderson, "Earth Structure from Free Oscillations and Travel Times," *Geophys. J. R. Astron. Soc.* 36, 411 (1974).
23. K. Levenberg, "A Method for the Solution of Certain Non-linear Problems in Least Squares," *Quart. Appl. Math.* 2, 164 (1944).
24. M. Foster, "An Application of the Wiener-Kolmogorov Smoothing Theory to Matrix Inversion," *J. Soc. Indust. Appl. Math.* 9, 387 (1961).
25. J. N. Franklin, "Well-posed Stochastic Extensions of Ill-posed Linear Problems," *J. Math. Anal. Appl.* 31, 682 (1970).
26. T. H. Jordan and J. N. Franklin, "Optimal Solutions to a Linear Inverse Problem in Geophysics," *Proc. Natl. Acad. Sci. USA* 68, 291 (1971).
27. L. R. Sykes, "The Seismicity and Deep Structure of Island Arcs," *J. Geophys. Res.* 71, 2981 (1966).
28. D. T. Griggs, D. D. Jackson, L. Knopoff, and R. L. Shreve, "Earthquake Prediction: Modeling the Anomalous V_p/V_s Source Region," *Science* 187, 532 (1975).
29. T. J. Fitch and J. M. W. Rynn, "Inversion for V_p/V_s in Shallow Source Regions," *Geophys. J. R. Astron. Soc.* 44, 253 (1976).
30. K. M. Lahr, J. C. Lahr, A. G. Lindh, C. G. Bufe, and F. W. Lester, "The August 1975 Oroville Earthquakes," *Bull. Seismol. Soc. Am.* 66, 1085-1099 (1976).
31. F. Gilbert, "Excitation of the Normal Modes of the Earth by Earthquake Sources," *Geophys. J. R. Astron. Soc.* 22, 223-226 (1971).
32. D. W. McCowan, "Moment Tensor Representation of Surface Wave Sources," *Geophys. J. R. Astron. Soc.* 44, 595-599 (1976).
33. P. M. Morse and H. Feshbach, Methods of Theoretical Physics (McGraw-Hill, New York, 1953).
34. A. Ben-Menahem and S. J. Singh, "Computation of Models of Elastic Dislocations in the Earth," in Methods in Computational Physics, v. 12 (Academic Press, New York, 1972).

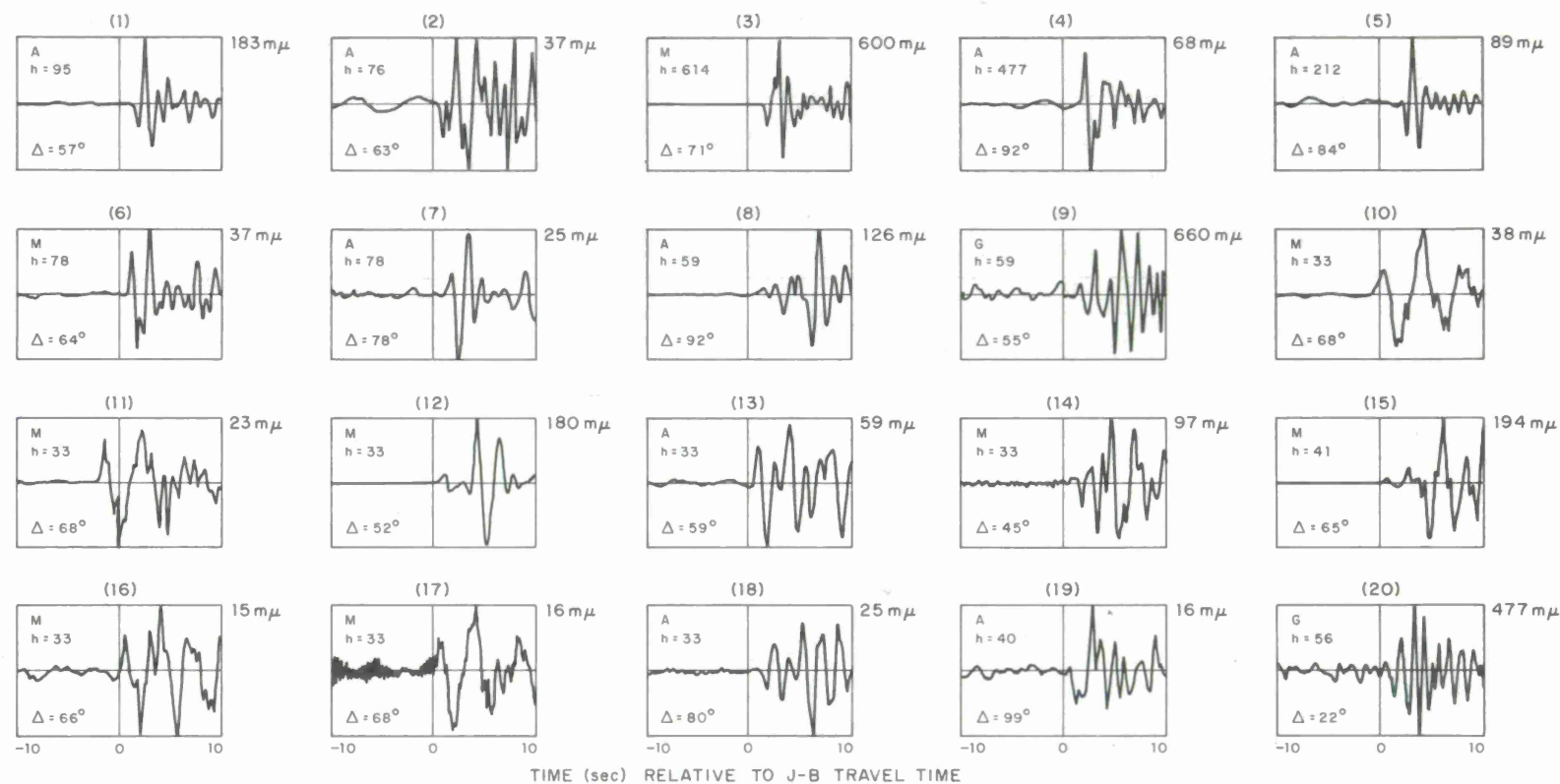


Fig. I-1. Short-period waveforms recorded at SRO stations. Each seismogram is identified by station (A = AMNO, M = MAIO, G = GUMO), depth h (km), and distance Δ (deg). Maximum amplitude of signal is also given. Each seismogram is of 20-sec duration, centered at arrival time predicted by J-B tables.

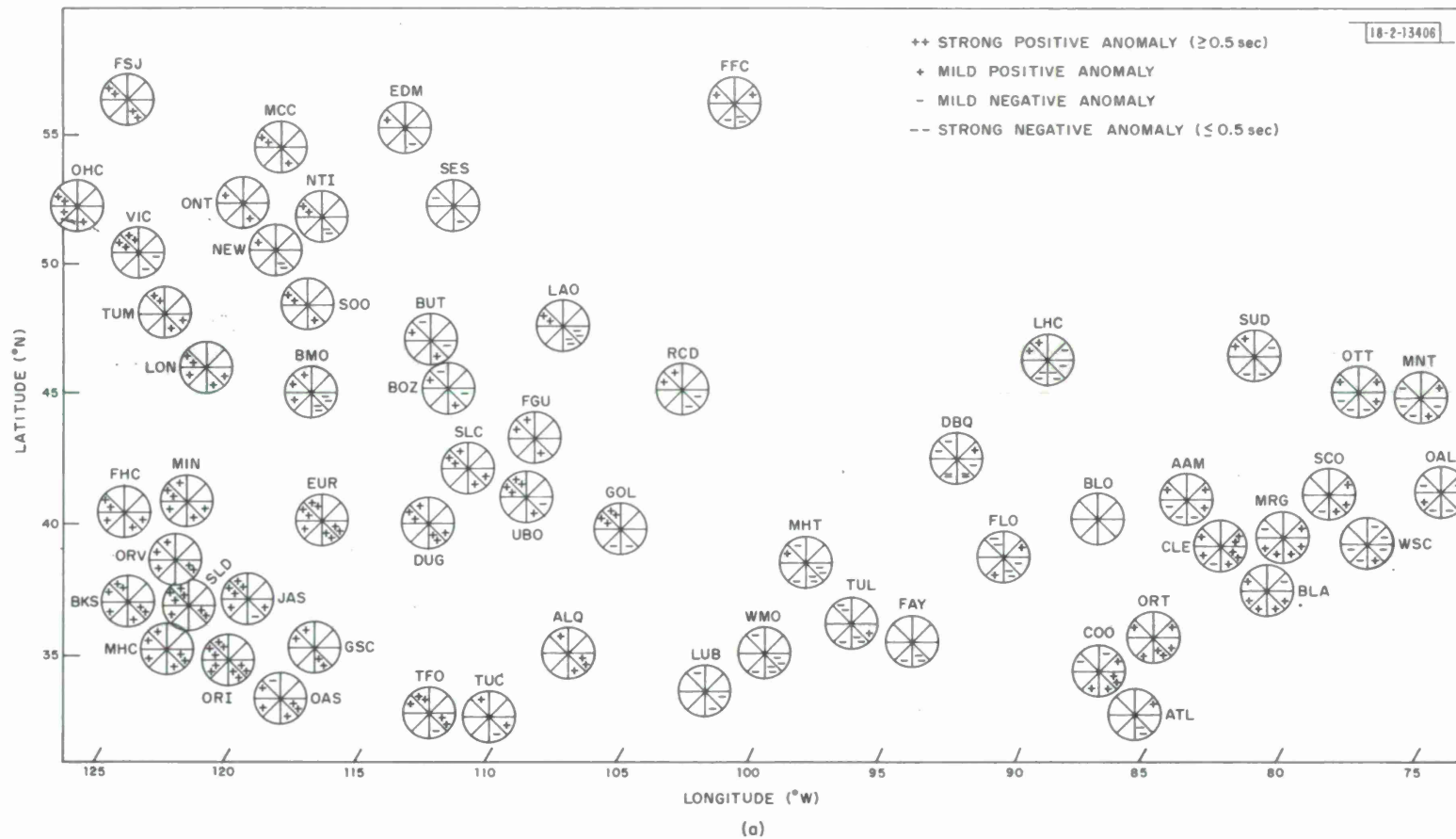


Fig. I-2(a). Azimuthal dependence of P travel-time anomalies for western and central U.S., as referred to model PEM, for distance ranges $\Delta = 30^{\circ}$ to 40° . Azimuth range is divided into 45° regions. Blanks indicate no, or not enough, data.

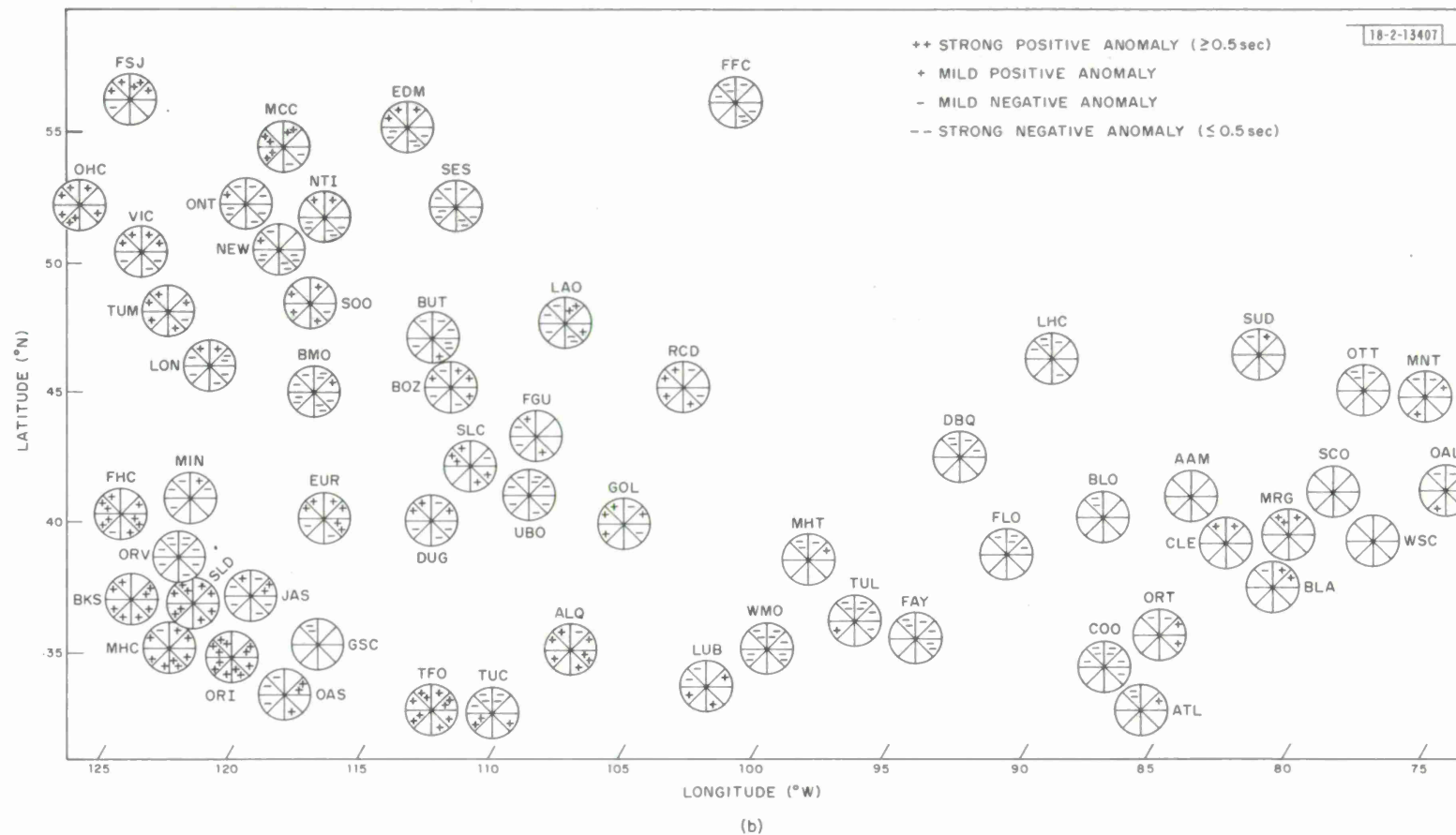


Fig. I-2(b). Azimuthal dependence of P travel-time anomalies for western and central U.S., as referred to model PEM, for distance ranges $\Delta = 80^{\circ}$ to 90° . Azimuth range is divided into 45° regions. Blanks indicate no, or not enough, data.

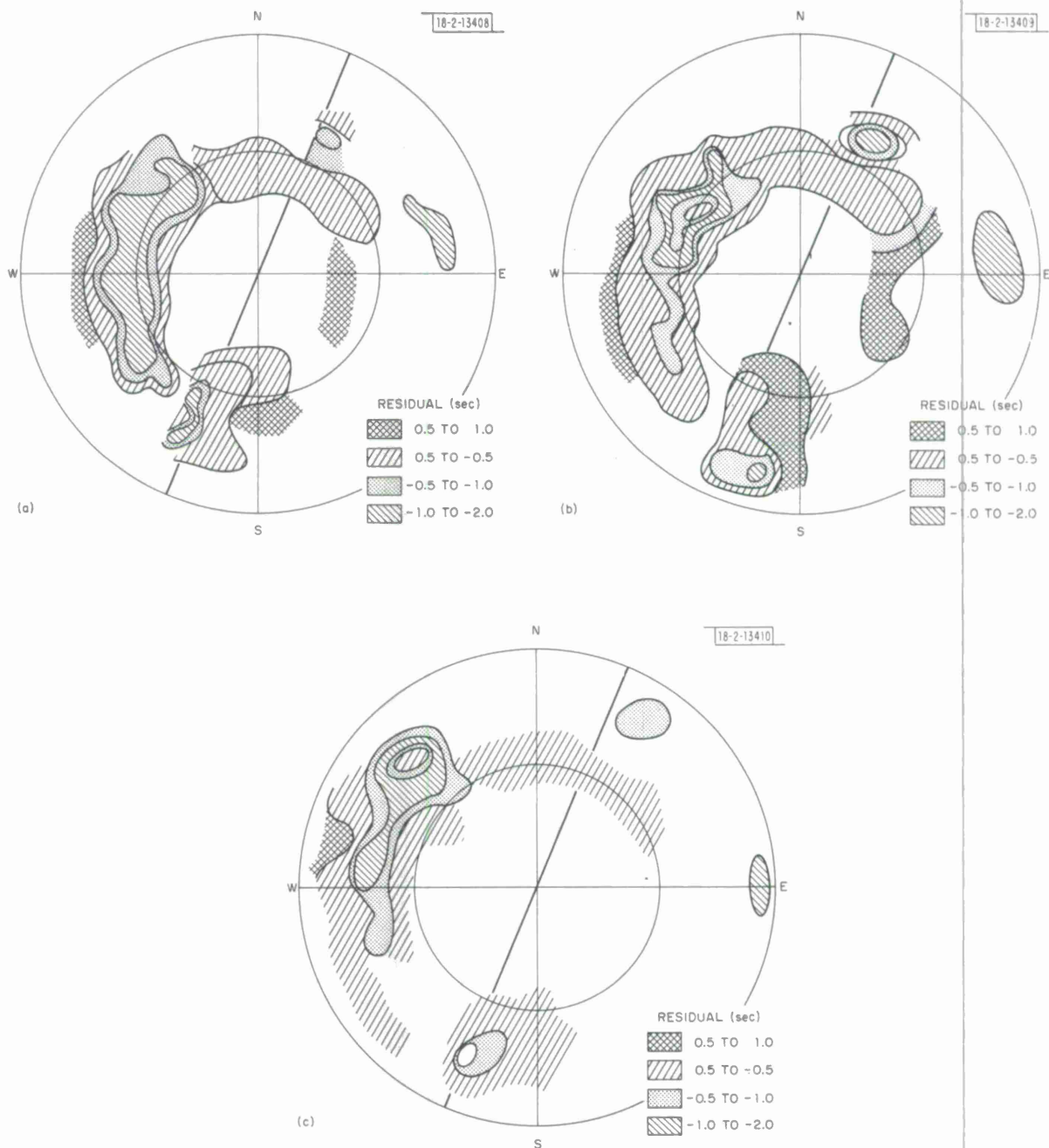


Fig. I-3. Residual spheres. Residuals in seconds are mapped in an equal area sense onto lower half of focal sphere. Data have been taken from events with latitude range 15°S to 35°S and longitudes greater than 177°E in Tonga-Kermadec region, and station corrections due to Sengupta and Julian¹⁹ have been included. Strike of seismic zone is shown by heavy line oriented $\text{N}23^{\circ}\text{E}$. Depth ranges shown are (a) depth < 100 km, (b) $200 < \text{depth} < 400$ km, and (c) depth > 550 km.

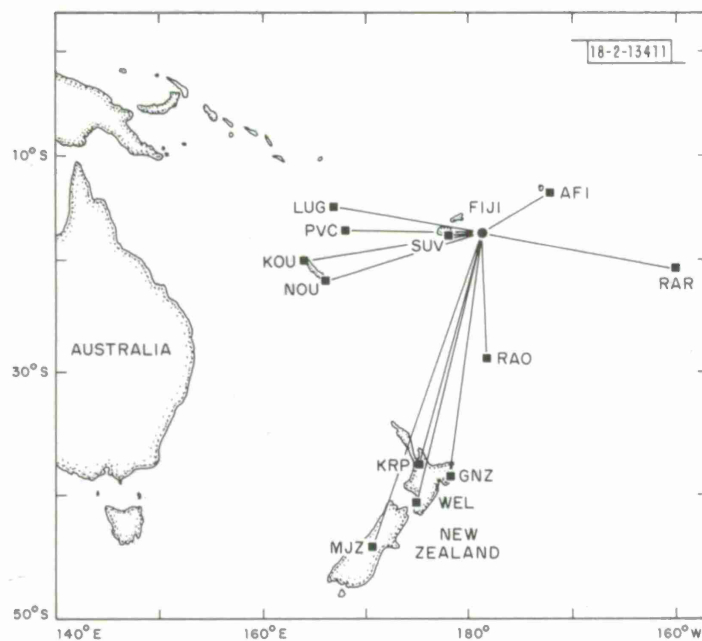


Fig.I-4. Southwest Pacific and ray paths to island stations.

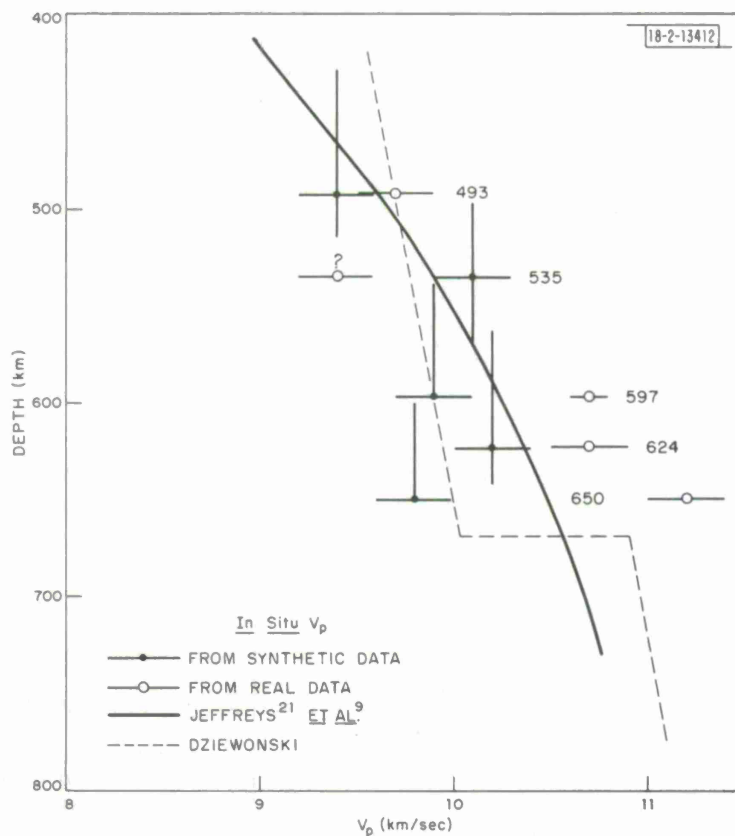


Fig.I-5. V_p vs depth. Error bars on in situ V_p 's are one standard deviation. Vertical line attached to each synthetic datum gives depth range for particular group of secondary events.

Fig.I-6. Deep seismic zone: a map view. Dashed line indicates location of epicenters of earthquakes with depth 500 km (after Sykes²⁷).

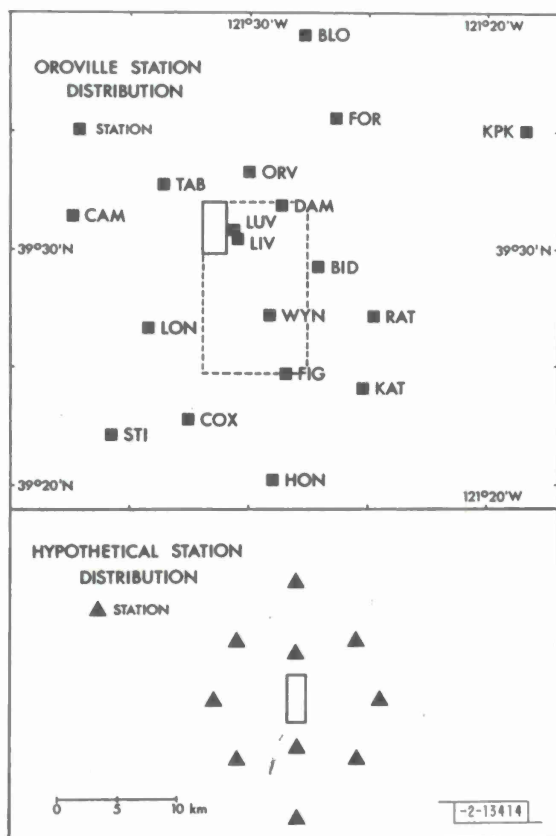
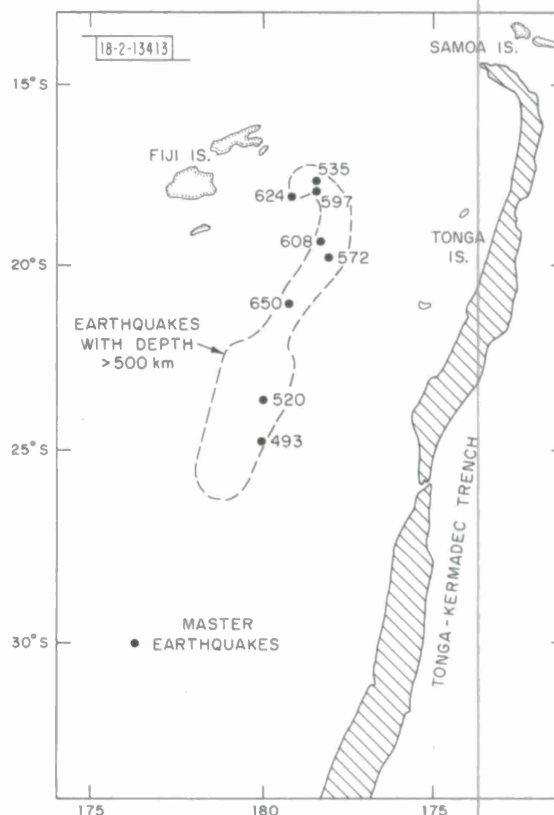


Fig.I-7. Station-source configuration for real and synthetic data.

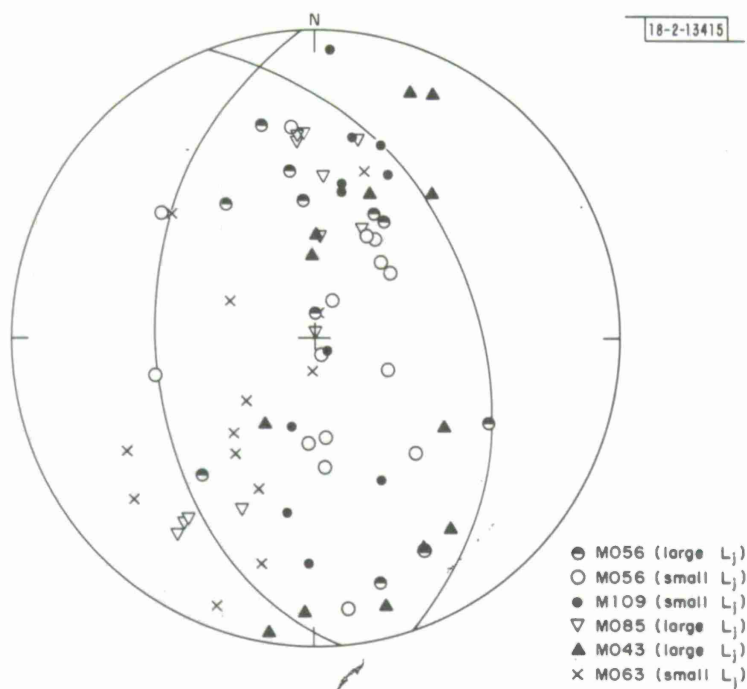


Fig. I-8. Relative locations projected on focal mechanism for main shock. Nodal planes and relative locations are projected in an equal area sense onto lower half of focal sphere. L_j refers to separation between master and j^{th} secondary events.

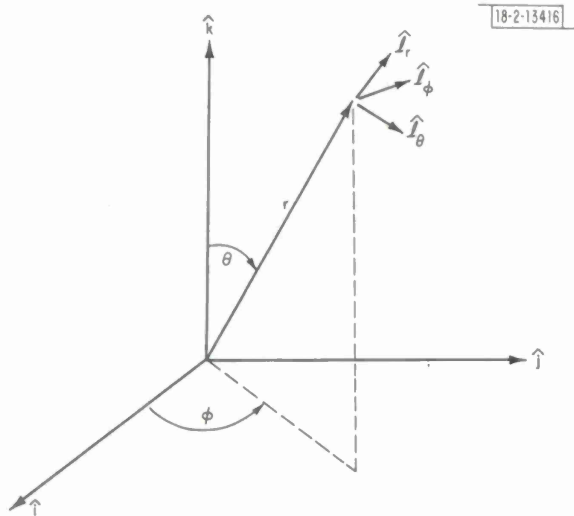


Fig. I-9. Source coordinate geometry.

II. SURFACE-WAVE STUDIES

A. AN EFFICIENT ALGORITHM FOR DETERMINING PHASE AND GROUP VELOCITIES OF SURFACE SEISMIC WAVES

The method of bandpass filtering in the frequency domain has become a powerful tool for the determination of phase- and group-velocity plots of surface seismic waves. The original seismic signal is first filtered to remove all frequencies except a narrow positive frequency band centered about some frequency ω_c . The group arrival time at frequency ω_c is then defined as the time of maximum amplitude in the envelope of the complex filtered waveform, and the phase velocity can be determined from the phase relationship at the time of maximum amplitude. The process is repeated for several center frequencies spanning the range from approximately 0.007 to 0.06 Hz to construct group- and phase-velocity curves. The method is particularly useful in situations when the signal is not well-dispersed, as in typical oceanic paths or short continental paths, for in these cases a simple peak and trough method is impossible.¹⁻⁴

Since we have available to us an extensive database of high-quality digital SRO surface-wave data, it would be worthwhile to construct group- and phase-velocity curves for a large number of paths, both continental and oceanic. The limitation of the method is that it requires an excessive amount of computation time, and since we plan to run a large data set through the processing, it is advantageous to reduce the computation time, if at all possible. Therefore, we have developed a slight modification to the original algorithm which results in a greater than 10:1 savings in computation time.

In the original algorithm, the Fourier transform of the original waveform is multiplied by the Fourier transform of the bandpass filter, and an inverse Fourier transform of the product yields the filtered seismic signal. The FFT size must be large to obtain adequate frequency resolution. (We used a 2048-point FFT for data sampled at 2-sec intervals to obtain 0.00025-Hz resolution.) The spectrum of the filter is zero everywhere except in a narrow band about ω_c . We used the Gaussian filter suggested by Dziewonski:¹

$$H(\omega) = \exp \left\{ -\alpha \left[(\omega - \omega_c) / \omega_c \right]^2 \right\}$$

where α is typically 50. However, our proposed modification is suitable for any narrow band-pass filter.

Since the spectrum of the filtered seismogram is zero outside of a narrow frequency range, a considerable reduction in bandwidth can be achieved by simply shifting the spectrum by an amount $-\omega_c$ (Fig. II-1). A frequency shift of $-\omega_c$ is equivalent to multiplication of each sample $s(n)$ of the time-domain signal by $\exp[-j\omega_c n t]$, where t is the sampling interval. The advantage of such a step is that the size of the IFFT can now be reduced to include only the nonzero samples near ω_c , without effecting any loss of information. Whereas a 2048-point IFFT previously was needed for each ω_c , now only a 128- or, at most, 256-point IFFT is needed. The large forward FFT is computed only once, whereas the IFFT must be computed once for each center frequency. We have found it necessary to include 75 center frequencies in order to resolve phase ambiguities; hence, the forward FFT time is insignificant by comparison.

The output of the modified Dziewonski algorithm is a signal with slowly varying amplitude and slowly varying phase relationship (Fig. II-2). Group velocity is computed as:

$$U_g = r / (\text{delay} + n_{pk}t - t_{inst})$$

where r is the great-circle distance between earthquake epicenter and receiver, delay is the time between the event and the first sample of the seismogram, $n_{pk}t$ is the time between the origin and the peak amplitude in the filtered seismogram, and t_{inst} is the instrument time delay. The peak amplitude location is determined by matching a parabola to the three samples surrounding the peak and choosing the interpolated peak time as follows:

$$y_1 = A(n-1) - A(n) \quad n = \text{peak location}$$

$$y_3 = A(n+1) - A(n) \quad A(n) = \text{amplitude at peak}$$

$$n_{pk} = n + \frac{(y_1 - y_3)}{2(y_1 + y_3)} \quad .$$

Figure II-3 shows a typical group-velocity curve for a well-dispersed continental path.

The computation of phase velocity is slightly more complicated. The phase at peak amplitude in the original Dziewonski algorithm is defined approximately as (ignoring, for the moment, instrument and source phase):

$$\phi_c(n_{pk}) = \omega_c n_{pk}t + \omega_c \cdot \text{delay} - k_c r \pm 2\pi i$$

where k_c is the wavenumber corresponding to frequency ω_c , and $2\pi i$ is an unknown number of full cycles. In the modified algorithm, the first term, $\omega_c n_{pk}t$, is removed by the frequency shift of ω_c , and hence the equation is somewhat simplified. The first step is to compile a sequence of phase values corresponding to maximum envelope amplitude for 75 consecutive frequencies ω_c . Then, this sequence is unraveled to resolve ambiguities of 2π (made continuous) and corrected for instrument response, and, if possible, source phase. Next, $c(\omega_c)$ is evaluated at a low frequency for several values of i :

$$\phi_c(n_{pk}) = \omega_c \cdot \text{delay} - k_c r \pm 2\pi i$$

$$c(\omega_c) = \frac{\omega_c}{k_c} = \frac{\omega_c r}{k_c r} = \frac{\omega_c r}{\omega_c \cdot \text{delay} - \phi_c(n_{pk}) \pm 2\pi i} \quad .$$

The first reasonable choice for i (e.g., velocity less than 4.6) is kept, and phase velocities are then computed for all 75 frequencies using i , $i+1$, and $i+2$ to construct three possible phase-velocity curves. The correct curve can then usually be selected by eye, given a knowledge of what is reasonable (Fig. II-3).

S. Seneff

B. GROUP-VELOCITY MEASUREMENTS ACROSS EURASIA FROM MASHAD SRO

During January-March 1976, some 100 events within or on the margins of Eurasia were sufficiently well-recorded at Mashad SRO such that well-dispersed surface-wave trains were observable. The wide dynamic range of the instrument is particularly well-suited to dispersion studies since small events from regions of low seismicity produce usable data. The three-component data have been rotated into the source azimuth and this, in general, produces good separation of Love- and Rayleigh-wave radiation into the transverse and radial components. To date, only the vertical (Rayleigh) component has been studied; in the future, we intend to utilize the polarization properties of surface waves to reduce body-wave contamination.

Figure II-4 shows the events to which Rayleigh-wave dispersion has been calculated from Mashad. Many more events during the remainder of 1976, giving more complete coverage in distance and azimuth, remain to be analyzed. A new adaption of the multiple-filtering technique⁵ (see Sec. A above), permitting rapid and simultaneous determination of group and phase velocities, has been used to produce dispersion curves for these paths.

Although the phase-velocity resolution is much better than that in group velocity, the smallness of many of the events means that the crucial initial source phase is virtually impossible to determine because of the difficulty of obtaining both source mechanism and depth. For events in regions where the relative motion of the plates, and thus the dominant slip vector, is known (such as the western boundary of the Pacific plate), it is possible to make an intelligent guess as to the source mechanism; but, within continental Asia, the variety of observed faulting even within small source regions makes this very difficult.

Figure II-5 shows group-velocity dispersion determined for some of the paths shown in Fig. II-4. By far, the most notable effect is that of the very thick low-velocity crust in Tibet and Western China, which lowers group velocities to below 3.0 km/sec even at periods of 40 to 50 sec. Dispersion to Siberia, Mongolia, and the Kuriles is somewhat faster than expected, considering the varied tectonic regimes crossed. The highest group velocities are those to Iceland and Svalbard in the north-west quadrant, crossing the Russian platform and Baltic Shield.

Many more events remain to be analyzed, and when sufficient data have been obtained we intend to carry out an inversion to determine group velocity as a function of geographical position within the region, without making any prior assumptions as to the connection between surface geology and dispersion.

R. G. North

C. GROUP-VELOCITY DISPERSION MEASUREMENTS AT NEAR-IN DISTANCES

Of the three commonly used methods for measuring the group-velocity dispersion of a wavetrain – instantaneous frequency analysis, narrowband filtering, and moving-window spectral computation – only the latter is easily adaptable for use on compact waveforms. The inherent weakness in the moving-window method has always been obtaining adequate spectral bandwidth from short segments of data. If the data sample is long, the computed spectrum is characteristic of the whole window, and, if the data sample is short, it is difficult to resolve low frequencies. However, recently, the addition of Maximum Entropy Spectral Analysis (MESA)⁶ to data-adaptive prediction-error filtering⁷ offers a potentially valuable means of achieving adequate frequency resolution from short data windows.

The method consists of computing the data-adaptive prediction-error operator using Griffiths⁷ formulation of the Widrow⁸ algorithm. This is basically the same algorithm used for SP deconvolution studies reported in the previous two SATS. At specified group arrival times, the inverse of the prediction-error-operator spectrum is computed and contour-plotted. The advantage to using an adaptive filtering algorithm is that the data design the filter, thus allowing the filter to "track" variations in the data spectrum.

As examples of the method, group-velocity-dispersion curves were computed for two relatively close-in events selected from our SRO data catalog. These data are particularly well-suited to dispersion computations because of their broad-band high-dynamic-range characteristics. The pertinent event information is given in Table II-1. The first event is one of the

TABLE II-1							
PDE INFORMATION FOR THE TWO EVENTS USED IN THIS STUDY							
Station	Date (1976)	Origin Time	Latitude (°N)	Longitude	Depth	Region	m_b
ANMO	12 May	19:50:00.2	37.2	116.2°W	0	S. Nevada	4.9
MAIO	16 March	07:28:57.6	27.3	55.1°E	33	S. Iran	5.4

few NTS explosions which did not overdrive the Albuquerque SRO. Rotated LP seismograms are shown in Figs. II-6 and II-7, respectively. A close examination of Fig. II-7 reveals the fundamental and first higher Rayleigh-wave modes interfering on the LPZ component and the barest hint of a higher Love-wave mode preceding the fundamental on the LPT component.

In processing these and other similar data, we found that the filter learning constant suggested by Griffiths⁷ ($\alpha = 0.75$) was optimum; it gave the best balance between slow adaptation on the one hand and noisy performance on the other. Best results were obtained by using a suite of filter lengths between 8 and 20 sec long where the data were sampled at 1 Hz. As a general rule, short filter lengths produced narrower contours but were less sensitive to longer periods than the long filters.

The results are presented in Figs. II-8 through II-10, which are group-velocity-dispersion curves plotted to overlie the spectral-contour plots. Doubtful values are indicated by dashed lines. No attempt was made to remove either the SRO instrument or source-group delays. Since maximum values of this combined effect are less than 10 sec for the band indicated in the plots, the group-delay error cannot be more than 0.01 km/sec. Both events were approximately 1000 km away from the respective SROs. Another possible analysis delay is due to the filter learning response time. However, the examples run by Griffiths using the same learning constant⁷ show that this is a negligible effect.

The results in Figs. II-8 through II-10 suggest that the two propagation paths, the Colorado Plateau in the first case and Iranian Platform in the second, exhibit relatively low group velocities. Figure II-8 includes a comparison with the group-velocity dispersion from Model 72T (see Ref. 9) appropriate to the Basin and Range geologic province. This comparison indicates that the Colorado Plateau structure is significantly different than that for Model 72T. Other investigators,¹⁰ using WWSSN LP recordings of the Rio Blanco explosion, have found that the Colorado Plateau has a relatively thick crust (~40 to 45 km) for the Western U.S. underlain by the usual low-velocity upper mantle. The group-velocity-dispersion curve in Fig. II-8 is quite similar to one presented by Keller *et al.*¹⁰ for the northern Colorado Plateau. It therefore lends additional support for their conclusions.

Figures II-9 and II-10 are Rayleigh- and Love-wave group-velocity-dispersion curves for the Iranian Platform. In this case, it was possible to measure a Rayleigh-wave higher mode and see, at least, the indication of a Love-wave higher mode. The high-resolution method was used to advantage because the higher modes were intermingled with the fundamental modes. Both fundamental modes exhibit extraordinarily low group velocities which can be compared with the dispersion from the Gutenberg continent model also included in the figures. Such group velocities would indicate an anomalously thick crust, possibly 50 to 60 km. This interpretation

is consistent with the tectonic explanation that Iran is being compressed by the northward movement of the Arabian lithospheric plate.

D. W. McCowan

D. A RAYLEIGH-WAVE STRUCTURE FOR NOVAYA ZEMLYA

The sequence of large (presumed) explosions detonated in Novaya Zemlya¹¹ generated unusually good Rayleigh-wave seismograms. A pair of these events, one from the northern and the other from the southern test areas on Novaya Zemlya, recorded at ALPA were analyzed using the single-station, two-event method due to Alexander.¹² This analysis produced a phase-velocity-dispersion curve appropriate to the source region. The pertinent information for the two events is given in Table II-2.

TABLE II-2 PDE INFORMATION FOR THE TWO NOVAYA ZEMLYA EVENTS USED IN THIS STUDY					
Event	Date	Origin Time	m_b	Latitude [†] (°N)	Longitude (°E)
Northern	28 August 1972	05:59:57	6.3	73.3	55.1
Southern	2 November 1974	04:59:56	6.7	70.8	54.1
† These epicenters imply an event separation of 285 km.					

The method consists of crosscorrelating the set of seismograms from one event with those from the other. Since these were array observations, the resulting set of crosscorrelations from corresponding array elements was then averaged. If the following assumptions are valid:

- (1) The source region can be characterized by an average plane layered structure;
- (2) The Rayleigh waves from both events traverse a common path from the nearer (northern) event to the receiver;
- (3) Interference due to multipathing can be neglected;
- (4) The source phase for the two events is either identical or, at least, known;

then the phase of the resulting cross spectrum will exhibit the phase-velocity dispersion in the source region, i.e.,

$$\exp\left[-i \frac{\omega D}{C(\omega)}\right]$$

Here, D is the separation between the two events.

Assumption (2) above is fortuitously met by this combination of events and station. The two events are almost perfectly lined up on a great-circle path which traverses the Arctic Ocean and passes through ALPA. Because this path consists largely of an ocean basin, multipathing effects can be expected to be small. However, as will be seen in the results, there were minima

TABLE II-3 LAYER PARAMETERS FOR MODEL NZ1			
Thickness	P-Wave Velocity	S-Wave Velocity	Density
2.0	4.95	2.26	2.65
3.0	5.55	2.73	2.70
5.0	6.00	3.03	2.75
5.0	6.00	3.05	2.75
5.0	6.20	3.35	2.80
10.0	6.78	3.97	2.85
10.0	6.78	3.97	2.85
10.0	6.78	3.89	2.85
10.0	7.99	4.33	3.25
15.0	8.10	4.29	3.25
20.0	8.10	4.27	3.25
20.0	8.20	4.39	3.28
40.0	8.20	4.52	3.30
60.0	8.20	4.59	3.31
100.0	8.20	4.60	3.32
0	8.40	4.67	3.37

TABLE II-4 DATA AND COMPUTED VALUES FROM MODEL NZ1			
Period	Observed C(T)	Computed C(T)	Computed U(T)
51.08	3.83	3.85	3.45
42.70	3.75	3.77	3.35
36.49	3.69	3.69	3.24
31.93	3.63	3.62	3.15
28.38	3.56	3.56	3.07
25.54	3.50	3.49	2.99
23.22	3.45	3.44	2.92
21.28	3.39	3.38	2.84
18.24	3.28	3.28	2.70
15.96	3.18	3.18	2.57
14.19	3.09	3.09	2.48

in the cross-power spectrum which may have been caused by multipathing. Since there is practically no available information in the open literature on the crustal structure of Novaya Zemlya, it is impossible to know a priori whether or not assumption (1) is met. Instead, the spirit of this experiment is to postulate it as being true, and see whether or not the results are reasonable. We have also assumed that, both events being presumed explosions, they will have identical source phases. However, the possibility exists that either event could have triggered tectonic stress release which would add an earthquake-like source phase to the spectra.

The results are shown in Fig. II-11. The data points are plotted as small dots with a smooth curve drawn through them in the lower graph. The upper graph is a plot of the relative power in the averaged cross spectrum. As can be seen, there is a pronounced minimum near the 22-sec period; this corresponds to a dip in the measured phase velocities. Two other areas of erratic phase velocity are at the 17- and 30-sec periods, respectively. The former of these corresponds to another minimum in the relative power of the latter to a hump-like side lobe above the main peak. We did not consider any of these phase-velocity fluctuations to be significant.

The X's in the lower graph are computed phase velocities from the model given in Table II-3. The data, as well as the computed phase and group velocities, are given in Table II-4 where one can see that the rms error of the fit to the phase-velocity data is approximately 0.01 km/sec. This model was obtained by using the stochastic inverse method applied to surface-wave-dispersion data.¹³

The model is characterized by a 50-km-thick crust and a slight shear-wave low-velocity zone in the lower mantle. The latter is probably an artifact of the inversion process, since lower bounds on the standard deviations of the model parameters exceed this dip. The 50-km-thick crust is the result of several attempts at data inversion. It minimizes extreme oscillations in adjacent layer parameters. This model is not offered as a unique solution, as it is well known that surface-dispersion data, band-limited and for only the fundamental mode, cannot determine a unique structure. Furthermore, differential model parameter changes within the averaging kernels produced by the stochastic inversion method agree equally well with the data within its observational errors. We only offer this as a plausible model that fits our limited data.

The 50-km-thick crust of Model NZ1 is consistent with the explanation that Novaya Zemlya is a northern extension of the Ural mountains. Kosminskaya et al.¹⁴ present results for Russian crustal structures determined by "Deep Seismic Sounding" (DSS). In particular, their Fig. 11 is a contour map of Moho depth for the whole Soviet Union. The Ural mountain belt, which generally lies along the 60°E longitude meridian, is pictured as having a 45-km-thick crust. Unfortunately, none of their profiles are appropriate to Novaya Zemlya; however, the P-wave velocity structure of our model is similar to that for their Ukrainian Shield profile.

D. W. McCowan
P. Glover†
S. S. Alexander†

† Pennsylvania State University, University Park, PA.

E. PURE PATH DISPERSION OF OVERTONES OF SURFACE WAVES

Most of the inferences with respect to the differences between the continental and oceanic mantle have been made through interpretation of "pure path" dispersion of mantle waves.¹⁵⁻¹⁷ As the resolving power of these data becomes poor for depths greater than 300 km, the details of the models below this level are rather arbitrary and it has been shown that they are unnecessary to explain the observations. One of the ways to increase the overall resolution of the upper-mantle structure would be to obtain reliable measurements of dispersion of overtones to periods as short as 20 sec.

Figure II-12 is meant to illustrate this point. Models 1066A and 1066B of Gilbert and Dziewonski¹⁸ give an equally good fit to the normal-mode data, even though their upper-mantle structures differ significantly in detail; model B has abrupt discontinuities, while model A is smooth. Group velocities for the fundamental mode are practically identical for periods greater than 100 sec; for shorter periods, the discrepancies are caused by differences in the details of crustal structures. Yet the dispersion curves for the fourth and sixth overtones are significantly (5 to 7 percent) different in the range of phase velocities that correspond to the turning point between 300 and 700 km depth. It is clear that if precise group velocity data were available, much more could be said about the actual structure of the upper mantle. At the same time, Fig. II-12 illustrates the fact that such measurements could not be made using individual recordings, as there are multiple intersections of group velocity curves where dispersion could not be resolved by the frequency-time analysis.

Initial progress in the development of techniques of mode separation has been made by Forsyth¹⁹ and Nolet^{20,21} who have used the "stacking" approach in order to achieve mode separation. The procedure outlined here is different in several aspects from those applied previously.

- (1) Having a regional network of seismographs (for example, WWSSN stations in Western Europe) and a given location of the source and its source mechanism, we compute synthetic seismograms for the first orbit (R1) for each overtone whose dispersion is to be measured; this should be done for each of the stations in the array; the main elements of the theory have been described by Gilbert.²² The synthetic spectrum of the n^{th} overtone is

$${}_n\tilde{w}(\underline{r}, r_0, \omega) = \frac{a}{{}_n u(\omega)} \exp[-{}_n\alpha(\omega) \cdot \Delta / {}_n u(\omega)] \cdot \sum_{i=1}^6 {}_n\tilde{A}_i(\underline{r}, r_0, \omega) \cdot f_i(\omega)$$

where \underline{r} is the position of the receiver in the epicentral coordinate system, r_0 is the radius of the source, a is the Earth's radius, ${}_n\alpha(\omega)$ is the attenuation factor ($\alpha = \omega/2Q$), Δ is the epicentral distance, ${}_n u(\omega)$ is the group velocity, ${}_n\tilde{A}_i(\underline{r}, r_0, \omega)$ are analogous to those in Gilbert and Dziewonski's¹⁸ expressions (2.1.30) for spheroidal modes and (2.1.31) for toroidal modes, with the functions $X_\ell^m(\Theta)$ replaced by those in Eq. (21) of Gilbert;²² $f_i(\omega)$ are the spectra of the six independent components of the moment rate tensor.

- (2) Compute the stack of crosscorrelograms between the actual recordings (s_j , where j is the index of a station within the array) and the synthetic seismogram for a given overtone (${}_n w_j$). The spectrum of such a stack is

$${}_n r(\omega) = \sum_j s_j(\omega) \overline{{}_n w_j(\omega)}$$

where the bar denotes the complex conjugate. This process can be repeated for any number of events from roughly the same source region.

- (3) Measure differential group- and phase-velocity dispersion using the "residual dispersion method" of Dziewonski *et al.*²³

Figures II-13(a-p) show results of a synthetic experiment in which an attempt was made to isolate the energy associated with individual overtones using an earthquake in Japan (49.05°N, 153.6°E, depth 135 km) and 15 WWSSN stations: AQU, ATU, COP, ESK, HLW, IST, JER, KEV, KON, MAL, NUR, PTO, STU, TOL, and UPP. The observed seismograms were simulated by superposition of fundamental Rayleigh and Love modes and their first seven overtones. The period range of the analysis extended from 20 to 500 sec. The retrieved signal for the fundamental Rayleigh mode is nearly perfect; in all remaining cases, we note various degrees of interference with other modes. By proper windowing and truncation, it should be possible to recover most of the information for ${}_1 S_\ell$; ${}_3 S_\ell / {}_2 S_\ell$ seems to be mostly disturbed by a high-frequency energy (the third overtone is continuous with the second after intersection with the core-mantle boundary Stoneley branch). The same is true of ${}_5 S_\ell / {}_4 S_\ell$; ${}_6 S_\ell / {}_5 S_\ell$ is quite good, but ${}_7 S_\ell / {}_6 S_\ell$ and ${}_8 S_\ell / {}_7 S_\ell$ might not yield reliable results. Of the toroidal modes, probably ${}_1 T_\ell$ has the best signal-to-noise ratio, but several others should also prove useful.

We would like to point out that these results are for a single source. If several sources with slightly different locations were used, the phase-equalization procedure would always lead to reinforcement of the signal of interest, while other modes having different phase-arrival times would tend to cancel.

The method can be applied to investigate purely continental paths under the Eurasia and, for example, oceanic paths under the Pacific using an array of stations in western United States and Canada. Also, stations in the eastern United States and Canada could be used to study dispersion from suitably located events on the Mid-Atlantic Ridge, and European stations would have a purely oceanic path for the events in the Caribbean.

If these studies are successful, and there is every indication that they should be, it would be very desirable to apply a relocatable network of broadband digital instruments for the specific purpose of investigating the multimode surface-wave dispersion along selected paths.

T. A. Chou†
A. M. Dziewonski

† Department of Geological Sciences, Harvard University, Cambridge, MA 02138.

REFERENCES

1. A. M. Dziewonski, S. Bloch, and M. Landisman, "A Technique for the Analysis of Transient Seismic Signals," *Bull. Seismol. Soc. Am.* 59, 427-444 (1969).
2. T. Furuzawa, "Group Velocities of Surface Waves from Near Earthquakes Around Japan," *J. Phys. Earth* 24, 131-147 (1976).
3. A. R. Leeds, "Lithospheric Thickness in the Western Pacific," *Phys. Earth Planet. Int.* 11, 61-64 (1975).
4. M. Yoshida, and Y. Satô, "Dispersion of Surface Waves Across the Pacific Ocean," *J. Phys. Earth* 24, 157-175 (1976).
5. A. M. Dziewonski and A. L. Hales, "Numerical Analysis of Dispersed Seismic Waves," in *Methods of Computational Physics*, Vol. 11 (Academic Press, New York, 1972).
6. J. P. Burg, "Maximum Entropy Spectral Analysis," paper presented at the 37th Annual Meeting of the Society of Exploration Geophysicists, Oklahoma City, OK, 1967.
7. L. J. Griffiths, "Rapid Measurement of Digital Instantaneous Frequency," *IEEE Trans. Acoust., Speech, and Signal Processing* 23, 207-222 (1975).
8. B. Widrow, "Adaptive Filters I: Fundamentals," Report SEL-66-126, Stanford Electronics Labs, Stanford, CA (1966).
9. Seismic Discrimination SATS, Lincoln Laboratory, M.I.T. (30 June 1976), pp. 40-42, DDC AD-A032754/4.
10. G. R. Keller, R. B. Smith, L. W. Braile, R. Heaney, and D. H. Shurbet, "Upper Crustal Structure of the Eastern Basin and Range, Northern Colorado Plateau, and Middle Rocky Mountains from Rayleigh-Wave Dispersion," *Bull. Seismol. Soc. Am.* 66, 869-876 (1976).
11. Seismic Discrimination SATS, Lincoln Laboratory, M.I.T. (30 June 1975), pp. 38-39, DDC AD-A014793/4.
12. S. S. Alexander, The Pennsylvania State University, University Park, PA (unpublished Research Note, 1969).
13. W. L. Rodi, P. Glover, T. M. C. Li, and S. S. Alexander, "A Fast, Accurate Method for Computing Group Velocity Partial Derivatives for Rayleigh and Love Modes," *Bull. Seismol. Soc. Am.* 65, 1105-1114 (1975).
14. I. P. Kosminskaya, N. A. Belyaevsky, and I. S. Volvovsky, "Explosion Seismology in the USSR," in *The Earth's Crust and Upper Mantle* (Geophysical Monograph 13, AGU, Washington, DC, 1969).
15. M. N. Toksoz and D. L. Anderson, "Phase Velocities of Long Period Surface Waves and Structure of the Upper Mantle; I. Great Circle Love and Rayleigh Wave Data," *J. Geophys. Res.* 71, 1649-1658 (1966).
16. H. Kanamori, "Velocity and Q of Mantle Waves," *Phys. Earth Planet. Int.* 2, 259-275 (1970).
17. A. M. Dziewonski, "Upper Mantle Models from Pure Path Dispersion Data," *J. Geophys. Res.* 76, 2587-2601 (1971).

18. F. Gilbert and A. M. Dziewonski, "An Application of Normal Mode Theory to the Retrieval of Structural Parameters and Source Mechanisms from Seismic Spectra," *Philos. Trans. R. Soc. Lond.* A278, 187-269 (1975).
19. D. W. Forsyth, "Contamination-free Love Wave Phase Velocities," *Trans. A.G.U. (abstract)* 54, 366 (1973).
20. G. Nolet, "Higher Rayleigh Modes in Western Europe," *Geophys. Res. Lett.* 2, 60-62 (1975).
21. ———, "Higher Modes and the Determination of Upper Mantle Structure," PhD. Thesis, University of Utrecht, The Netherlands (1976), 90 pages.
22. F. Gilbert, "The Representation of Seismic Displacements in Terms of Travelling Waves," *Geophys. J. R. Astron. Soc.* 44, 275-280 (1976).
23. A. M. Dziewonski, J. Mills, and S. Bloch, "Residual Dispersion Measurement — a New Method of Surface Wave Analysis," *Bull. Seismol. Soc. Am.* 62, 129-139 (1972).

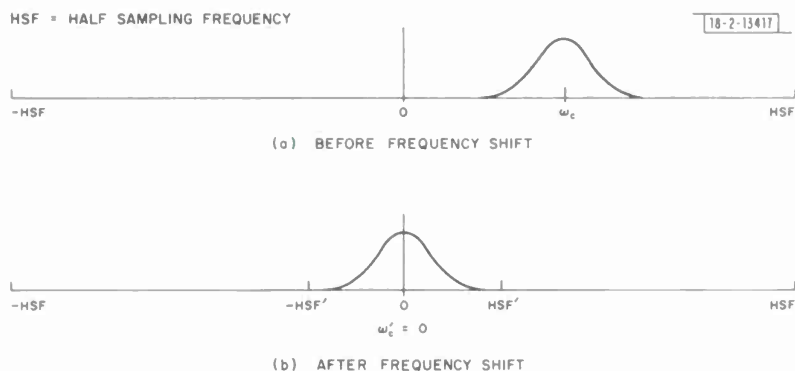


Fig. II-1. Frequency shift by $-\omega_c$ to achieve bandwidth reduction.

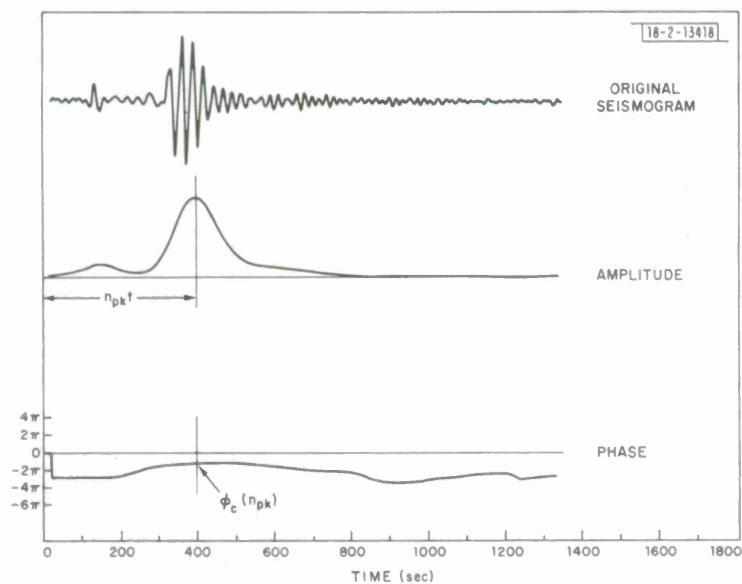


Fig. II-2. Amplitude and phase characteristics of filtered and frequency-shifted waveform resulting from analysis of oceanic surface-wave data for center frequency = 0.04 Hz ($T = 25$ sec).

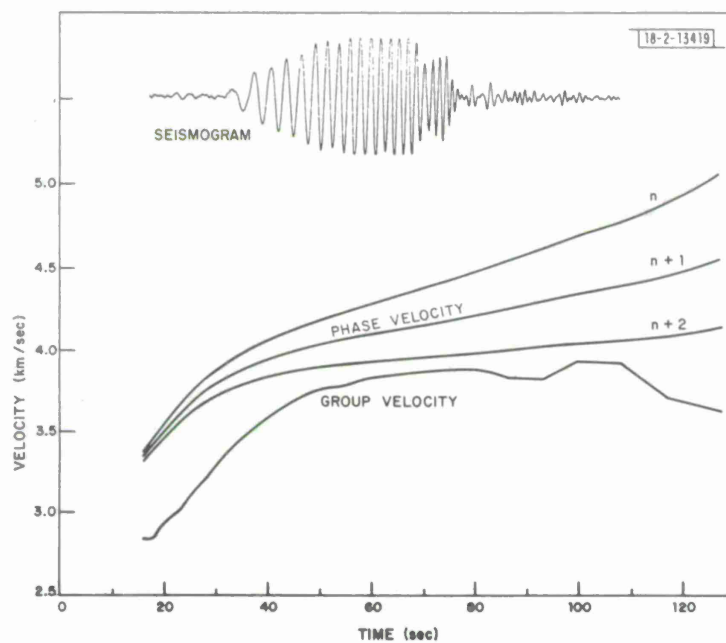


Fig. II-3. Group and phase velocities for well-dispersed continental seismic data determined using modified Dziewonski method. (Correction for source phase not included.)

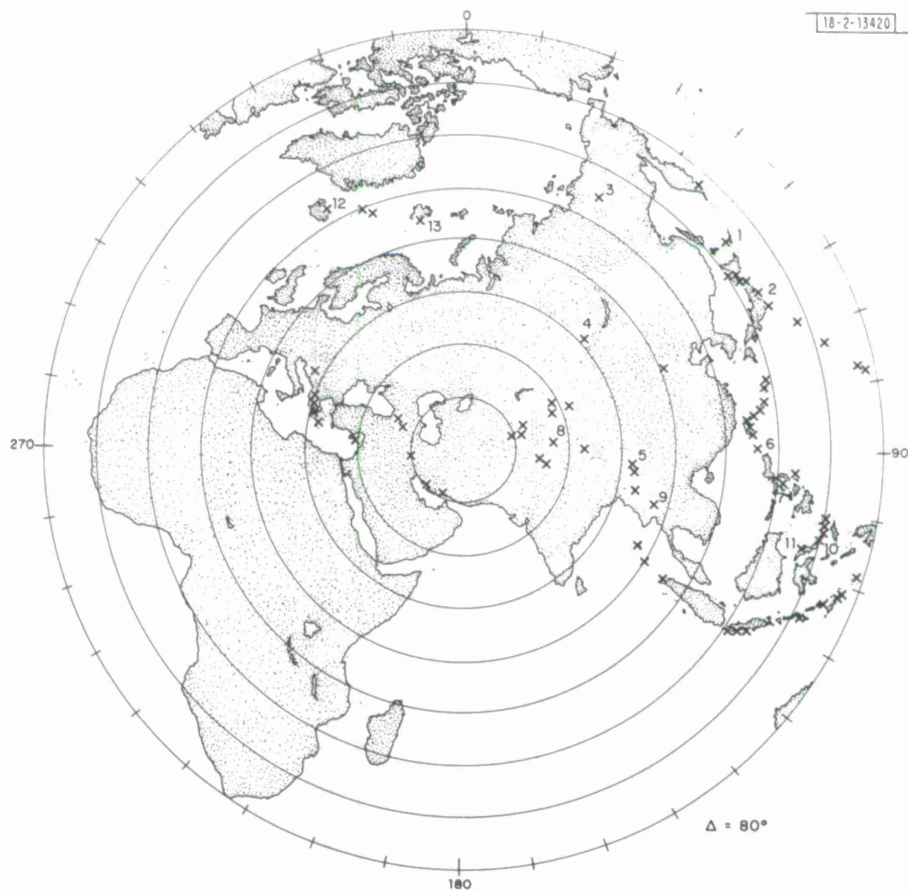


Fig. II-4. Polar plot centered at Mashad showing events recorded at Mashad SRO to which group velocity has been determined. Numbers refer to events from which group velocity is shown in Fig. II-5.

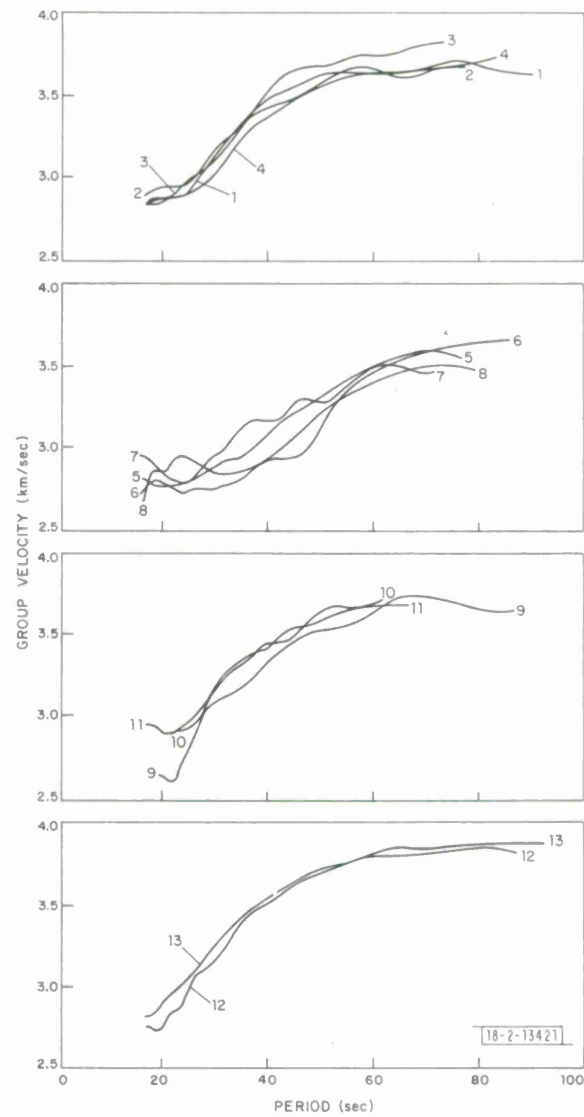


Fig. II-5. Group-velocity dispersion measured at Mashad for paths from events numbered in Fig. II-4.

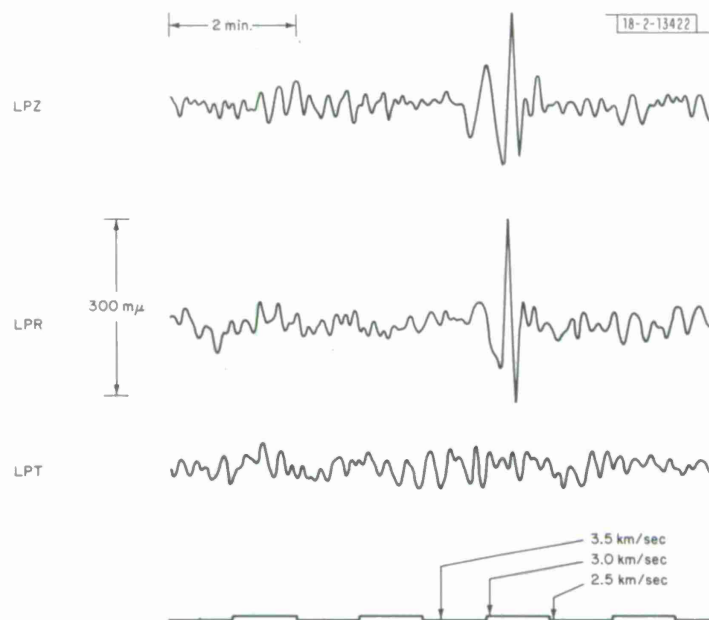


Fig. II-6. Rotated LP seismograms for 12 May 1976 NTS explosion recorded at Albuquerque SRO.

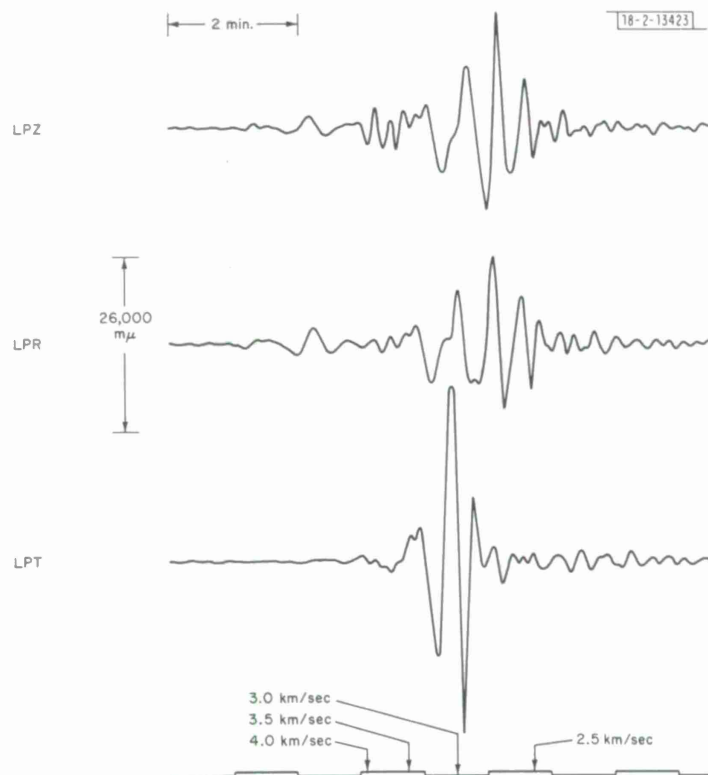


Fig. II-7. Rotated LP seismograms for 16 March 1976 Southern Iran earthquake recorded at Mashad SRO.

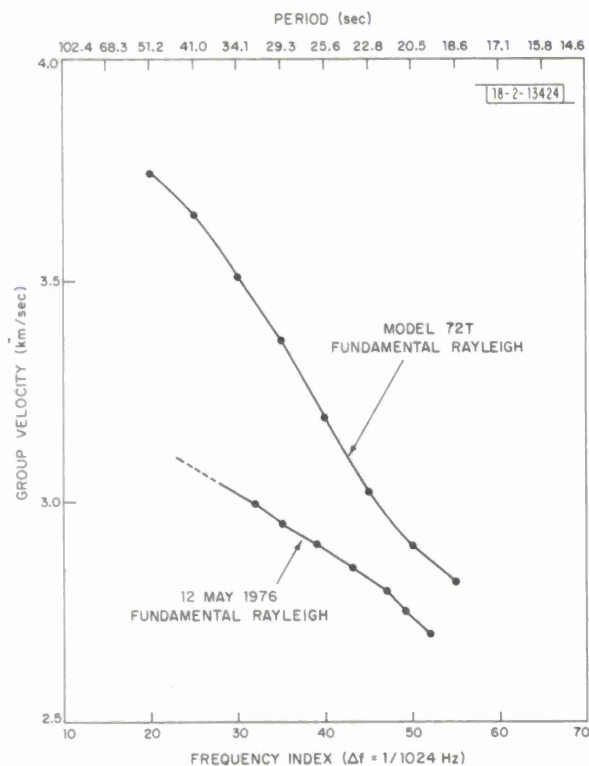
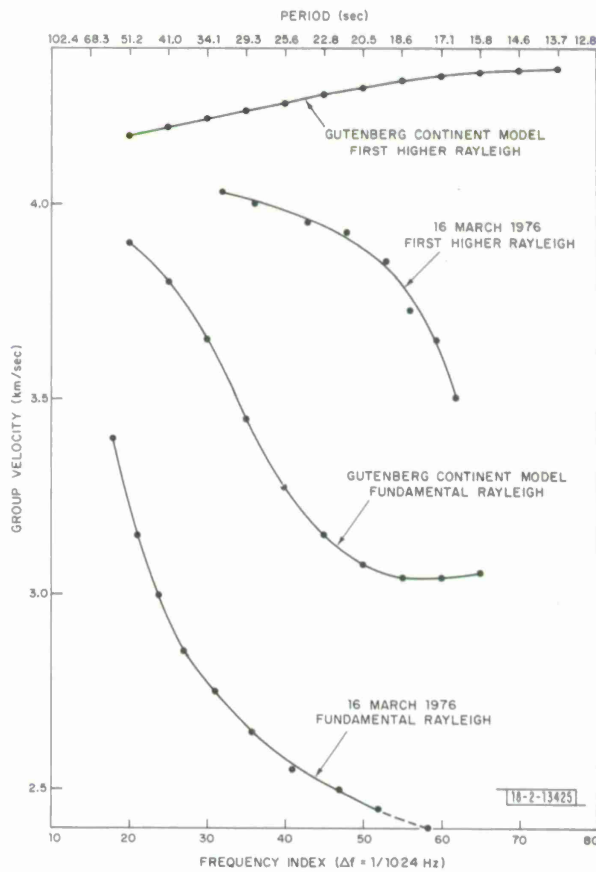


Fig. II-8. Rayleigh-wave group-velocity dispersion for 12 May 1976 NTS explosion. Also included for comparison is dispersion for Model 72T appropriate to Basin and Range structure.

Fig. II-9. Rayleigh-wave group-velocity dispersion for 16 March 1976 Southern Iran earthquake. Also included for comparison is dispersion for Gutenberg continent model.



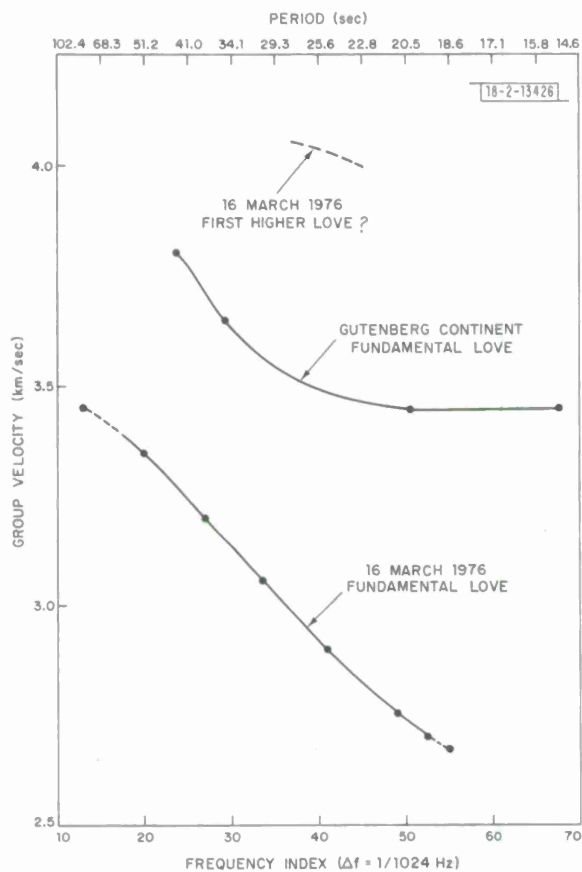


Fig. II-10. Love-wave group-velocity dispersion for 16 March 1976 Southern Iran earthquake.

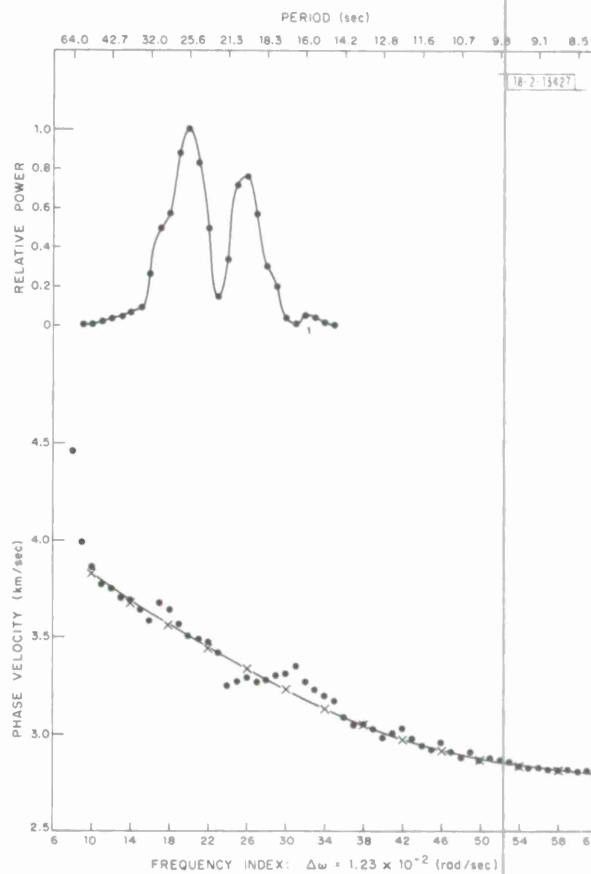
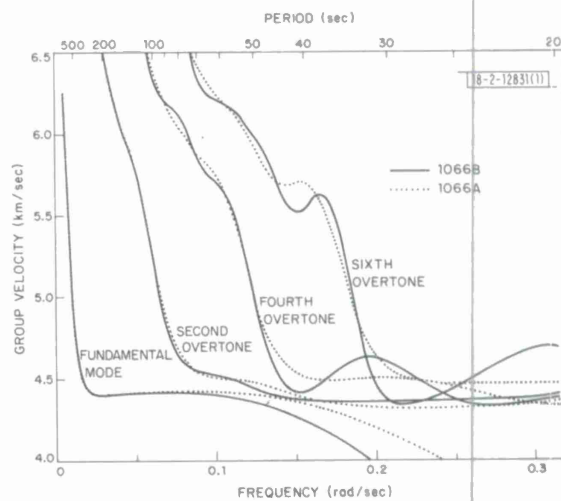


Fig. II-11. Phase-velocity-dispersion results for Novaya Zemlya. Lower graph shows observed data (dots), smoothed interpretation (line), and results computed from Model NZ1 (X's). Upper graph is a relative power in cross spectrum.

Fig. II-12. Comparison of group-velocity-dispersion curves for several overtones of Love waves computed for earth models 1066A and 1066B (Ref. 18).



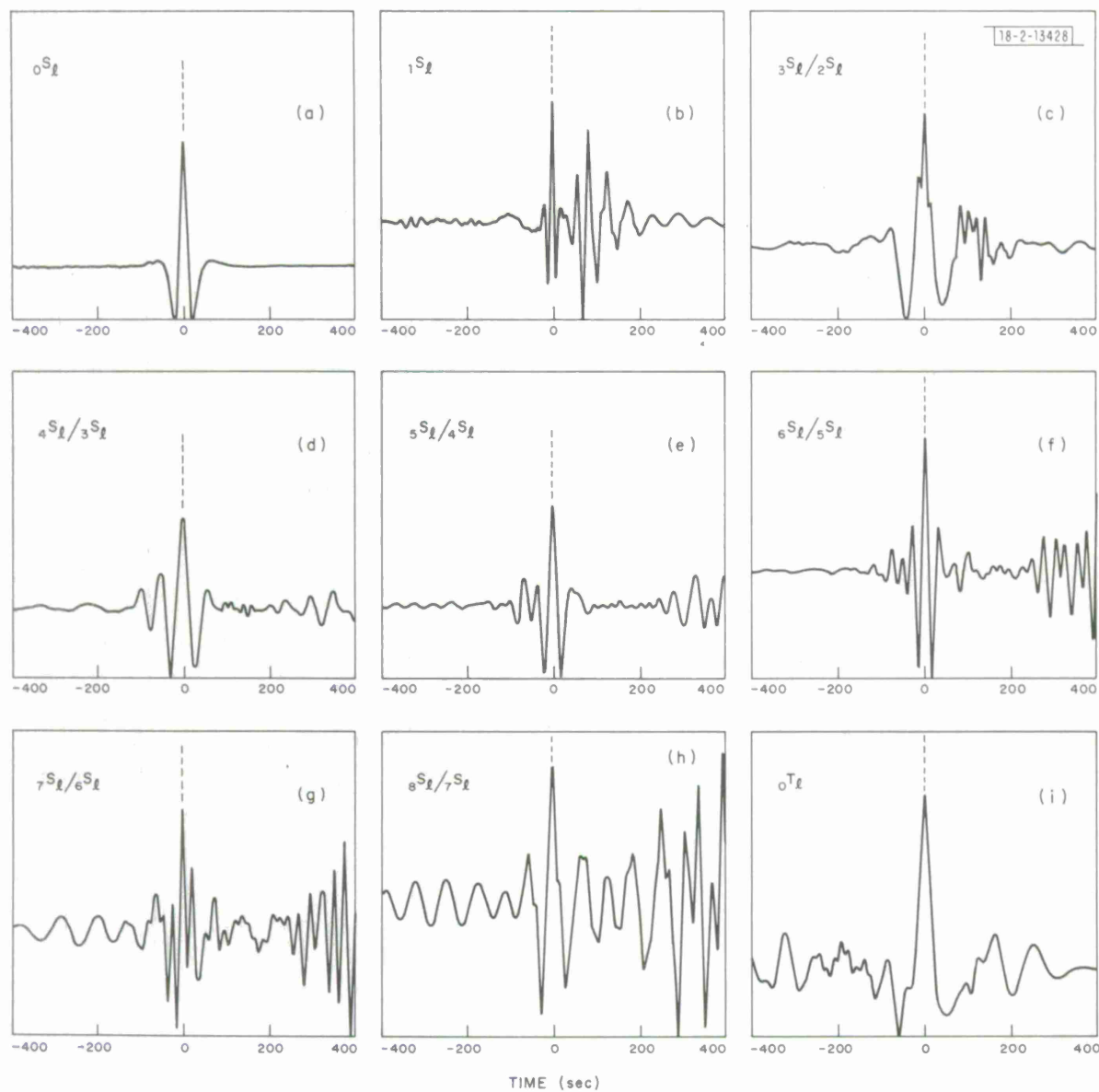


Fig. II-13(a-p). Synthetic examples of an attempt at extraction of residual dispersion for 16 overtones of surface waves by processing synthetic 3-component records from 15 European WWSSN stations.

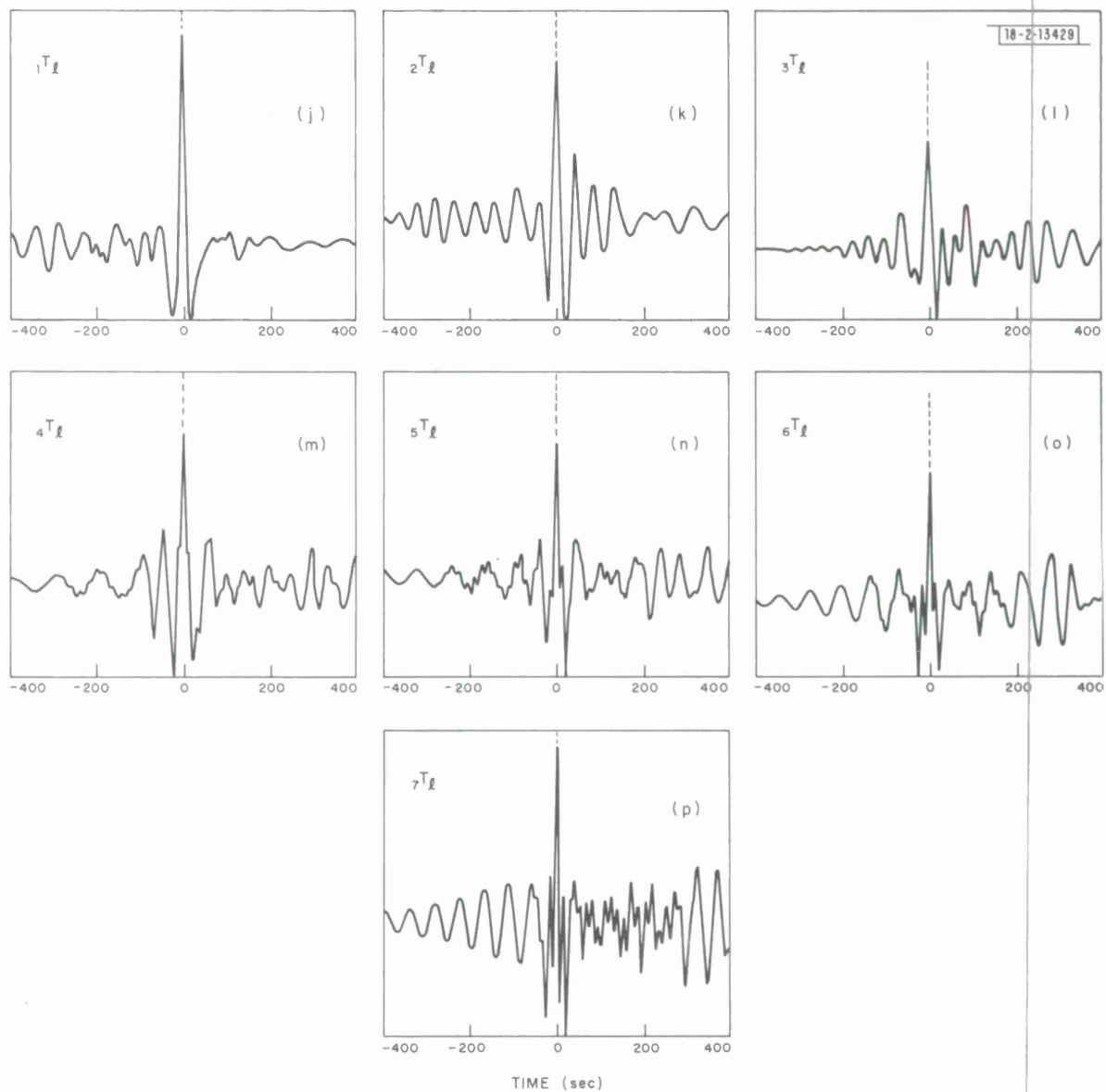
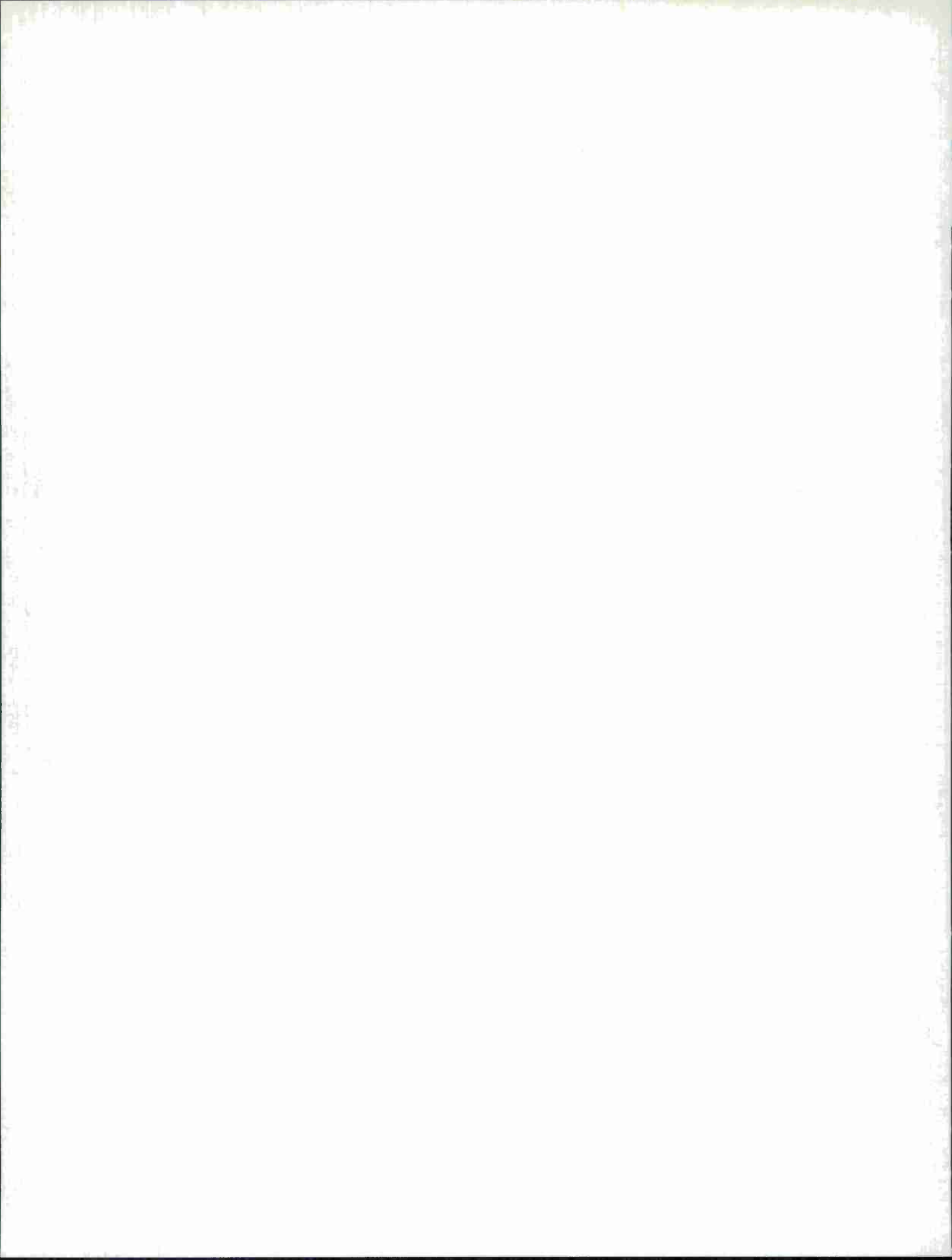


Fig. II-13(a-p). Continued.



III. MAGNITUDE, YIELD, AND ENERGY

A. AZIMUTHAL P-WAVE AMPLITUDE VARIATIONS FROM LARGE EXPLOSIONS

In recent years, increasing use has been made of body phase amplitudes to constrain source and structure models. These constraints often are applied with the barest understanding of amplitude variations from the effects of anelasticity and scattering. These effects are difficult to measure independently; at best, both effects are lumped together by assigning an effective Q or t^* to the particular ray path.

Teleseismic signals in the band pass of SP instruments vary by a factor of 4 globally due to the effects of station bias (North¹). In some regions, these biases change dramatically over distances that are short on a teleseismic scale, e.g., the station BKS at Berkeley, California and TFO in Arizona which have an arc separation of about 6° and have biases of +0.18 and -0.33, respectively, in units of $\log(A/T)$. The equivalent amplitude differences are about a factor of 3 for signals of about 1-sec period. Presumably similar differences would occur over shorter distances if stations were more densely distributed.

North¹ showed that m_b biases and the regional tectonic setting are correlated, but that there is little azimuthal variation in these biases for a given region or for a given station. Yet azimuthal variation related to near-source effects is well-known from studies of SP signals from explosions² and from earthquakes, particularly those in island arc regions.³

We have begun a study of the amplitude variation of P waves as a function of azimuth with LP amplitudes from two explosions: Cannikin in Amchitka Island [Fig. III-1(a)], and one in Novaya Zemlya [Fig. III-1(b)]. The LP amplitudes are particularly useful for this study because the signal is simple, e.g., see Frasier, Sec. H below. As a result, the chance of reading errors is minimized and the formal modeling of these waveforms is encouraged. The object of this work is to separate the gross effects of scattering, including focusing and defocusing, from those of anelasticity and thus to measure the real t^* for the earth. Explosions are preferred to earthquakes for this work because, ideally, explosions radiate seismic energy uniformly, although some deviation from uniformity may result from the release of tectonic strain.

Figure III-1(a) shows that P waves from Cannikin arrive at European and extreme eastern North American stations with amplitudes diminished by a factor of 2 to 3 from the average amplitude recorded elsewhere (about 7μ normalized to an arc distance of 60°). This azimuthal variation can be explained by defocusing of signals that pass through the seismic zone inclined from the Aleutian Arc. Three-dimensional ray tracing by Jacob⁴ has shown that body phases recorded at European stations from the Amchitka explosion, Longshot, will travel through the slab and show negative travel-time residuals. We intend to quantify this amplitude effect in the future.

The smaller-magnitude Novaya Zemlya explosion shows no broad amplitude variation comparable with the Cannikin signals; however, amplitudes recorded in the Middle East over an azimuth window of about 20° are larger than a mean amplitude for this event by about a factor of 2. In the middle of this window are two stations, AAE and NAI, near the East African rift that recorded low amplitudes. The azimuth window corresponding to stations in the Western United States as far east as Texas is also characterized by low amplitudes. These observations are consistent with North's¹ study in that stations near the rift and those in the Western United States show m_b biases equivalent to amplitude diminutions of 60 and 40 percent, respectively.

T. J. Fitch
C. W. Frasier

B. SEISMIC SCALING INFORMATION FROM SRO DATA

Seismic Scaling Laws are of great importance to discrimination since determination of the correct law would allow one to predict M_s - m_b , M_s -Moment, and even m_b -Moment relations for earthquakes and explosions. Unfortunately, as has been pointed out,⁶ measurements of magnitude and moment are often insufficiently precise, primarily because of our lack of knowledge about source mechanism (as opposed to size) and propagation effects, to enable the various laws proposed to be tested. A powerful way of testing these laws is to compare spectral ratios of events of different sizes, but from the same source region, with model predictions. The SRO stations, with their large dynamic range and high digital-data quality, are particularly well-suited to the calculation of spectral ratios, and we describe here the collection and preliminary analysis of a unique data set for this purpose.

On 21 January 1976, a large earthquake occurred in the southern Kurile Islands. During the following 20 days, some 120 aftershocks of this event were located by the USGS. Both surface and body waves from most of these events were well-recorded at Mashad SRO: the two other SROs installed at the time were either out of operation (Albuquerque) or of poor data quality (Guam). All the aftershocks reported have been relocated using a master-event technique, with the main shock as the master: use of this method considerably reduces the aftershock area (Fig. III-2). A remarkable feature of this sequence is the number of depth phases reported: for over 60 percent of the events, three or more (pP-P) times constrain the depth to 45 to 55 km.

We thus have a set of events covering a large range of magnitude, located within a very small area, and well-recorded at Mashad SRO. The chief remaining uncertainty is that of the source mechanism: most of the events were too small for first motion to be observable on WWSSN seismograms. Those which are identifiable show only compression, probably indicating faulting of thrust type, which is consistent with the tectonics of this area. Perhaps the most convincing evidence of a uniform fault plane orientation for these events is the remarkably similar nature of all the short-period P waveforms recorded at Mashad.

Figure III-3 shows vertical-component Rayleigh-wave trains from five of the Kurile events, as recorded at Mashad SRO. Records (a) and (e) are contaminated by surface waves from smaller events in the same source region. This figure dramatically illustrates the dynamic range of the SRO recording system: peak-to-peak Airy phase amplitudes corrected for instrument response, range from 720 μ (a) to 0.36 μ (e), corresponding to $M_s = 7.6$ and 4.2, respectively. We plan eventually to utilize sophisticated filtering techniques, such as polarization filtering (see Sec. IV-D of this report) and time variable filtering based on the easily measurable group-velocity-dispersion characteristics of the path to improve signal-to-noise ratios and eliminate contaminating wave trains from sources in the same region or elsewhere.

Figure III-4 shows amplitude spectra of events (a) through (d) of Fig. III-3. The spectra are calculated from exactly the same time window in each case; thus, the only difference between them should be caused by seismic scaling effects. The effects of the source mechanism, propagation path, and instrument should be identical. Events (a) through (d) are of $M_s = 7.6$, 6.6, 5.6, and 4.6, respectively. The ω^2 law of Aki⁶ predicts that these M_s values correspond to $M_0 = 4 \times 10^{27}$, 3.5×10^{25} , 2×10^{24} , and 1.8×10^{23} dyn-cm and corner periods $t_c = 105$, 30, 10, and 2 sec, respectively. Thus, within the period range over which we have calculated the spectra, we would expect to see significant changes in spectral shape over the magnitude range considered.

Figure III-5 shows spectral ratios of events (a/b), (b/c), and (a/c) calculated at periods of 10, 20, 50 and 100 sec (crosses). The solid line shown is the spectral ratio predicted by the ω^2 model. At the shorter periods of 10 and 20 sec, the agreement between observation and theory is quite good, but both the ratios involving event (a) are considerably less than predicted at the longer periods.

These data do not therefore satisfy the ω^2 law: we intend to investigate other scaling laws (such as those involving ω^{-1} and ω^{-3} falloff above the corner frequency) and to improve the quality of the spectra obtained.

R. G. North
C. W. Frasier

C. A RAPID AND INEXPENSIVE PROCEDURE FOR MEASURING THE RESPONSE OF THE WWSSN SP INSTRUMENT

As installed, the WWSSN SP recording system provides for a "weight lift" calibration pulse. Unfortunately, at the operating drum speed, the pulse cannot be resolved in time. In fact, it is difficult to see at all. Consequently, the preferred calibration procedure recommended by the manufacturer (Geotech) is to drive the calibration coil with AC currents and measure the amplitude and phase delay of the resulting output relative to the input current. To do this properly requires electronic equipment. Alternatively, the seismometer can be removed and mounted on a shake table where its amplitude and phase responses can be measured relative to the deflection of the table. While this latter procedure eliminates all seismic noise from the response measurement, it too requires specialized equipment. By far, the simplest procedure is to speed up the drum to resolve the calibration pulse. Then it can be Fourier analyzed in much the same manner as are the LP calibration pulses. We present here a relatively simple means of doing this with a geared-down electric motor.

The motor and pulley arrangement is shown in Fig. III-6. The Bodine motor has a 10-rpm reduction drive which generates 72 in.-oz of torque. In our experiment, the high torque was a useful feature because of friction in the recording drum drive system. To this motor was added a 2-in.-diameter pulley with an O ring to improve traction. The resulting recording rate was therefore approximately 1 in./sec.

We are indebted to the Weston Seismic Observatory (particularly Mr. R. O. Ahner) for allowing us to try out our procedure on their SPZ recorder during a record-changing session. In all, we recorded 11 calibration pulses with roughly an even mix of both polarities, of which 10 were usable. These were then hand-digitized on our Bendix digitizer at approximately 28-Hz sampling rate. The 10 sets of digital data were then phaseless low-pass filtered and resampled at 20 Hz. Each trace was aligned by eye and summed to produce the pulse shown in Fig. III-7. The measured overshoot ratio is approximately 12 to 1.

The seismometer used in the WWSSN SP system is a variable reluctance Benioff instrument. As such, the well-known Hagiwara⁷ formulation of the system response is inappropriate because the inductance of the seismometer has been neglected. The correct form of the equations has been derived by Chakrabarty and Choudhury⁸ and, when applied to the WWSSN SP system, predicts noticeably different amplitude and phase responses than zero-inductance approximations. In particular, the phase varies over $5\pi/2$ rad from DC to infinite frequency as opposed to 2π rad in zero-inductance systems.⁹ The installed overshoot ratio for the WWSSN SP system is supposed to be 17 to 1.

Amplitude and phase spectra computed from the calibration pulse in Fig. III-7 are shown in Figs. III-8 and III-9, respectively. The amplitude response is usable, with some smoothing, from DC to 5 Hz but the phase response is well-determined only between DC and 3 Hz. The discrepancy in usable bandwidths is explainable in terms of the fiducial phase delay of the pulse. Since the sampling frequency is 20 Hz, the phase error due to a starting-time error of $1/40$ sec (half the sampling interval) at 3 Hz is approximately 0.5 rad. The amplitude response is independent of this effect. The DC phase-angle asymptote of $-3\pi/2$ rad predicted by the theory is supported by the results in Fig. III-9. Unfortunately, due to the limited bandwidth of the experiment, it is not possible to verify a high-frequency asymptote of $+\pi$ rad. Judging from the measured overshoot ratio, this particular system appears to be underdamped relative to the specification. Whether or not the actual system parameters can be obtained through analysis of these measurements, as Mitchell and Landisman¹⁰ have done for WWSSN LP systems, remains to be seen. We have merely demonstrated that it is feasible to run the recording drum faster and record accurate calibration pulses.

D. W. McCowan
L. E. Sargent

D. ESTIMATION OF STATION DETECTION CHARACTERISTICS FROM BULLETIN DATA

In the previous SATS,¹¹ a study was described in which a maximum-likelihood method was used to determine the station detection parameters for a set of 72 stations, using data from the Bulletin of the International Seismological Center (ISC) for the years 1964 through 1973.

The present investigation is a continuation of the earlier one, and is aimed at refining the methods that can be used to extract detection parameters from these kind of data. Particular emphasis has been placed on documenting temporal changes in the detection threshold of some existing stations, on examining log A/T thresholds as compared with magnitude thresholds, on obtaining further information about the seismicity parameter β , and on the inclusion of saturation thresholds.

First, a pass was made through the 10 years of ISC data, and counts of log A/T values were extracted for each of the years for the 72 stations listed by North (see p. 2 in Ref. 11). Comparison of yearly plots of frequency against log A/T revealed substantial variations of detection characteristics with time. In a few cases, this was attributable to changes in station magnification. However, in most instances the variations had no obvious explanation, and were presumed to be due to variable operator performance. Only 12 of the 72 stations were consistent enough that all 10 years of data could be used in the determination of detection parameters, and about 20 of the stations showed such erratic behavior that they were not usable. In the remaining cases, portions of the catalog were used during which the stations were relatively consistent. The lengths of these portions generally lie in the range 4 to 6 years.

Frequency against log A/T plots are shown for three good stations in Figs. III-10(a), (b), and (c). A typical feature of all these plots is an extremely linear segment which is interpreted as being due to background seismicity. These straight segments were extended in both directions, and used to estimate the 50-percent detection threshold G_D and its associated spread γ_D , and the 50-percent saturation threshold G_S and its spread γ_S . These parameters, together with the station biases estimated by North,¹¹ are listed in Table III-1 for a particular subset of 30 stations.

TABLE III-1
DETECTION AND SATURATION PARAMETERS FOR A SET OF 30 STATIONS
(Biases from North¹¹)

Station	Bias	G_D	γ_D	G_S	γ_S
ALQ	-0.20	1.02	0.30	2.7	0.3
BMO	-0.29	0.28	0.30	3.1	0.3
BNS	+0.20	1.61	0.30	3.4	0.2
BOZ	-0.06	0.98	0.33	2.3	0.2
CAN	-0.02	1.57	0.40	3.2	0.2
CLL	+0.20	1.30	0.25	3.1	0.3
COL	+0.01	1.00	0.30	3.0	0.3
CPO	-0.07	0.87	0.25	3.4	0.4
EDM	+0.37	1.63	0.20	3.0	0.2
EKA	0.00	1.12	0.40	2.5	0.3
EUR	-0.24	0.67	0.40	2.3	0.4
GIL	-0.04	0.97	0.45	2.9	0.2
HYB	+0.19	1.62	0.35	3.3	0.3
KHC	+0.10	1.20	0.25	2.9	0.2
KON	+0.07	1.36	0.30	2.7	0.2
LON	-0.30	1.13	0.30	2.9	0.2
LPS	+0.04	1.20	0.25	2.9	0.4
MUN	+0.15	1.61	0.30	3.1	0.2
NDI	+0.33	1.77	0.40	3.0	0.2
NEW	+0.05	1.23	0.35	2.6	0.2
NOR	-0.14	1.02	0.28	2.9	0.4
PMR	-0.08	1.03	0.33	3.4	0.2
PNT	+0.13	1.40	0.30	2.8	0.2
POO	+0.17	1.54	0.25	2.8	0.2
PRU	+0.04	1.25	0.20	3.1	0.2
SJG	+0.24	1.46	0.35	3.1	0.2
TFO	-0.32	0.26	0.50	3.0	0.3
TUC	-0.14	1.21	0.30	2.5	0.2
UBO	-0.11	0.45	0.50	3.1	0.3
WMO	-0.17	0.41	0.23	2.7	0.5

The slopes of the straight portions of these plots showed some significant variations. Approximately half the stations studied contained slopes that were extremely close to 1.00. These included all stations in the U.S., Alaska, and Canada, together with most stations in India and Australia. On the other hand, with occasional isolated exceptions, stations in Africa had slopes in the range 1.10 to 1.20, while stations in Scandinavia, Europe, and Greenland (19 stations) had slopes in the range 1.20 to 1.30. An example of one of these is shown in Fig. III-10(c). These very interesting observations are being investigated further. The stations listed in Table III-1 all were consistent, with a seismicity slope of 1.00.

One possible explanation of these slope variations is that they are due to the inclusion of all events detected by the station, regardless of distance and depth. This might result in unusual emphasis of certain portions of the local spatial distribution of seismicity. To test this, another pass was made through the ISC catalog, this time retaining only events in the distance range 30° to 90° , and recording the station m_b value (i.e., including distance-depth corrections). The frequency-station m_b plots for the same three stations in Figs. III-10(a-c) are shown in Figs. III-11(a), (b) and (c). Although there is a slight increase in the scatter of the data points, the general agreement of these plots with the $\log A/T$ plots in Fig. III-10 is excellent. The slopes of the linear portions agree within the scatter of the data, and detection and saturation thresholds are consistent. There is a suggestion that the detection curves for station m_b do not fall off as fast, at low magnitudes, as those for $\log A/T$. This is unexplained at present.

Preliminary conclusions from this experiment are that Bulletin data can be used directly in the determination of station operating characteristics and station detection and saturation parameters. No explanation has yet been found for the strong variation in the seismicity parameter observed in different areas. In view of the shapes of many of the frequency-station magnitude plots, the maximum-likelihood method described earlier¹¹ may lead to unreliable results.

M. A. Chinnery
J. C. Johnston

E. COMPUTER SIMULATION OF NETWORK PERFORMANCE

The 30 stations which are listed along with their detection and saturation parameters in Table III-1 can be viewed as a model of a global network. The catalog simulation program described in the previous SATS¹¹ has been adapted to include saturation parameters, and it has been used to generate several artificial earthquake catalogs using these parameters. A value of 3.8 has been added to all thresholds to simulate a typical distance-depth correction: this allows the catalogs to simulate magnitude determination.

Events input to the program, based on a pseudorandom number generator subroutine, are constrained to have a probability distribution of the form $\log N = a + bm$, with the parameter $b = 1.00$. The actual distribution of these events for a catalog with 15,000 detected events is shown in Fig. III-12. Detections at each station are generated according to the detection probability curve at the station, and at least 3 station detections are required before a network detection is declared. The distribution of network-detected events is also shown in Fig. III-12 as a function of the true (input) magnitudes. The 50-percent detection threshold for the network is 4.35, and its 50-percent saturation threshold is about 7.07.

One interesting aspect of Fig. III-12 is the sharpness of the falloffs in detections at both low and high magnitudes. The effective γ for both detection and saturation is less than 0.2,

i.e., smaller than any of the γ 's for the individual stations. This is interpreted as being a result of the requirement that 3 station detections are necessary before an event is declared as a network detection. This unexpected result is being investigated further.

The artificial catalog may also be used to compare true event magnitudes with network magnitudes estimated in the usual way, by simply averaging the station magnitudes from those stations detecting the events, without regard to station bias. Figure III-13 shows incremental plots of frequency against true magnitude and network average magnitude. Notice the wide difference in these plots at low magnitudes.

The problem of bias in network average magnitudes is illustrated more clearly by Fig. III-14 which plots average values of magnitudes as a function of true magnitude. The upper magnitude limit behaves as expected; since stations receiving larger-than-average station magnitudes from an event saturate, the network average is biased smaller than the true magnitude. At low magnitudes, the network average magnitude is expected to be larger than the true magnitude. However, the opposite is observed, and this is attributed to the negative biases of the stations with the lowest detection thresholds (namely the VELA arrays BMO, TFO, UBO, and WMO, all in the Western U.S.).

The latter observation is likely to apply to both the ISC catalog and the USGS catalog of global earthquakes, at least for events within the teleseismic range (30° to 90°) from the Western U.S., which includes much of the Pacific earthquake belt. These same stations have the lowest detection threshold of all stations reporting to these catalogs. We therefore infer that the apparent detection threshold of these global networks may be several tenths of a magnitude unit too low. Further applications of computer simulations to the study of global network performance are continuing.

M. A. Chinnery

F. AN APPLICATION OF THE ENERGY-MOMENT TENSOR RELATION TO ESTIMATION OF SEISMIC ENERGY RADIATED BY LINE SOURCES

In a previous SATS,¹¹ we computed total radiated seismic energies for point-source models of the 1960 Chilean and 1964 Alaskan earthquakes. The expressions derived for the cases of three different source time functions are:

$$E = \frac{1}{2} \sum_n \frac{|M_n S_n(\vec{r}_s)|^2}{F_n \omega_n^2} \quad (\text{step}) \quad (\text{III-1a})$$

$$E = \frac{1}{2} \sum_n \frac{|M_o S_n(\vec{r}_s)|^2}{F_n \omega_n^2} \left[\frac{\sin(\omega_n T/2)}{\omega_n T/2} \right]^2 \quad (\text{ramp}) \quad (\text{III-1b})$$

$$E = \frac{1}{2} \sum_n \frac{|M_o S_n(\vec{r}_s)|^2}{F_n \omega_n^2} \left[\frac{\pi^2 \cos(\omega_n T/2)}{\pi^2 - \omega_n^2 T^2} \right]^2 \quad (\text{half sine wave}) \quad (\text{III-1c})$$

Here we show how to extend these results to a source model consisting of a finite propagating line source.

Dziewonski and Romanowicz (Sec. IV-E of this report) derived expressions for excitation of normal modes by a line source that may be approximated by a fragment of a great circle, of

angular extent Φ , connecting the beginning and the end points of the fault. They employed a specific rotation of the spherical coordinate system, first suggested in a different context by Backus.¹² Upon rotation, the fault represents a fraction of the equator where the origin point has a colatitude $\pi/2$, longitude 0, and the end point is at $\pi/2\Phi$. Assuming that the source mechanism does not change during the process of rupture, the expression for the spectral amplitude of a particular normal mode k is

$$\hat{u}_k(r, \omega) = \frac{\hat{C}_k(\omega)}{F_k \omega_k} \sum_{m=-\ell}^{+\ell} \bar{S}_k^m(r) \hat{\psi}_k^m(\omega) \quad (\text{III-2})$$

where $\hat{C}_k(\omega)$ is the resonance curve and

$$\hat{\psi}_k^m(\omega) = M_O(\omega) \bar{S}_k^m(r_O, \pi/2) \cdot \frac{\sin \chi_m}{\chi_m} e^{-i\chi_m} \quad (\text{III-3a})$$

If the moment release along the source line changes as $(\pi/2\Phi) \sin(\pi\varphi/\Phi)$, then the excitation function is

$$\hat{\psi}_k^m(\omega) = M_O(\omega) \bar{S}_k^m(r_O, \pi/2) \cdot \frac{\pi^2 \cos \chi_m}{\pi^2 - 4\chi_m^2} e^{-i\chi_m} \quad (\text{III-3b})$$

$\bar{M}_O(\omega)$ is the spectrum of the moment rate tensor of the equivalent point source. Most frequently it is represented by a constant $\bar{M}_O(\omega) = \bar{M}_O$ (cf. Kanamori¹³), but it could be modeled to include the effect of the finite fault width, which would lead to an asymptotic ω^{-2} decrease in amplitudes at high frequencies (Aki¹⁴).

$\bar{S}_k^m(r_O, \pi/2)$ is the strain tensor at coordinates $(r_O, \pi/2, 0)$, where r_O is the constant source radius (depth). The expressions for $\bar{S}_k^m = \bar{S}_k^m(r_O, \pi/2)$ can be found in Gilbert and Dziewonski¹⁵ [Eq.(2.1.19) for the spheroidal modes, and Eq.(2.1.20) for the toroidal modes].

Note that, for $\varphi = 0$,

$$Y_\ell^m(\theta, \varphi) = X_\ell^m(\theta) = (-1)^m \left[\frac{2\ell+1}{4\pi} \frac{(\ell-m)!}{(\ell+m)!} \right]^{1/2} P_\ell^m(\theta) \quad ; \quad (\text{III-4})$$

computations of X_ℓ^m for $\theta = \pi/2$ are particularly efficient.

The term

$$\frac{\sin \chi_m}{\chi_m} e^{-i\chi_m} \quad (\text{III-5})$$

where

$$\chi_m = \frac{1}{2} \Phi \left(\frac{\omega k r_O}{v} + m \right) \quad (\text{III-6})$$

is analogous to the directivity term of Ben-Menahem¹⁶ [Eq.(2-19)]. Dziewonski and Romanowicz discuss this analogy in some detail in Sec. IV-E of this report.

Thus, the expression for the kinetic energy of the k^{th} mode excited by a propagating fault is

$$E_k = \frac{1}{2} \sum_{m=-\ell}^{+\ell} |M_O(\omega) \bar{S}_k^m(r_O, \pi/2)|^2 \sin^2 \chi_m / \chi_m^2 \quad (\text{III-7a})$$

and for a modulated line source:

$$E_k = \frac{1}{2} \sum_{m=-l}^l |M_o(\omega); \bar{S}_k^m(r_o, \pi/2)|^2 \left(\frac{\pi^2 \cos \chi_m}{\pi^2 - 4\chi_m^2} \right)^2 \quad (III-7b)$$

It is obvious that when the fault length approaches zero, the expression above becomes identical to Eq. (III-1a); also, when $\Phi \rightarrow 0$, $\Phi r_o/v = T$, this expression is identical to Eq. (III-1b). Similarly, application of Eq. (III-7b) will lead to Eq. (III-1c) under these conditions. Note that

$$\frac{1}{2\pi} \int_{-\infty}^{+\infty} |\hat{C}_k(\omega)| d\omega = 1 \quad ; \quad (III-8)$$

thus, the kinetic energy of a mode is independent of attenuation.

The results for a modulated line source are presented in Table III-2 and in Figs. III-15 to III-17. Our choice of the model has been dictated by its asymptote ω^{-2} amplitude behavior at high frequencies, cf. Eq. (III-3b), in agreement with Aki.¹⁴ These are all for the 1960 Chilean earthquake using Plafker and Savage's¹⁷ fault-plane solution with the line source at 79.4-km depth. Table III-2 lists the cumulative energy in the toroidal modes for a variety of fault-length and rupture-velocity combinations. Thus, one can see here the effects of three experiments: (1) changing the fault length with a constant rupture velocity (3.5 km/sec); (2) changing the rupture velocity with a constant fault length (800 km); and (3) changing the fault length and rupture velocity but keeping the ratio constant (180 sec). The most rapid variation in the energy values given in Table III-2 occurs when the rupture velocity is comparatively high: 3.5 to 4.0 km/sec.

Figures III-15 to III-17 show typical toroidal-energy spectral distributions from the three above-mentioned experiments. In particular, Fig. III-15 results from a low rupture velocity (2.0 km/sec). There the spectral dropoff rate is similar to the half-sine-wave point source, but the scallops in the power envelope are not as prominent. Figure III-16 shows the results from a high rupture velocity (4.0 km/sec). These are similar to those for a step-function point source. This is explained by the fact that a moving source radiates energy most efficiently in its direction of travel, and is spectrally enhanced at high frequencies by the Doppler effect. Seen from the front, where the radiated energy is concentrated, it would appear as a step-function point source. Finally, Fig. III-17 shows the results from intermediate values of fault length and rupture velocity. Here, the energy distribution is smooth with a peak near the 160-sec period. The distribution also drops off cleanly above this peak.

Results for the line-source model with finite rupture velocity do not substantially alter our previous conclusions. In particular, the cumulative toroidal energy which we computed for the 1960 Chilean earthquake using the fault-length and rupture-velocity values estimated by Kanamori and Cipar¹⁸ (800 and 3.5 km/sec) is 9.1×10^{23} ergs. This corresponds to a half-sine-wave point-source duration of 140 sec, which is very close to that value obtained when the source duration was adjusted to give the reported M_s value. We can therefore conclude that, for the 1960 Chilean earthquake, both point- and line-source models give energies in good agreement with the Gutenberg-Richter relation.

The principal difference between the point- and line-source results is in the shape of the power spectrum envelope. Going to a more realistic finite source with a propagating rupture gives a smoother power spectrum. However, increasing the rupture velocity to 4.0 km/sec from 3.5 km/sec produces an unacceptable envelope shape which, in our frequency band, resembles

TABLE III-2 TOTAL TOROIDAL ENERGY FOR THE 1960 CHILEAN EARTHQUAKE [†] AS A FUNCTION OF FAULT LENGTH AND RUPTURE VELOCITY			
Toroidal Energy (erg)	Fault Length (km)	Rupture Velocity (km/sec)	Ratio (sec)
8.96×10^{24}	200.0	3.5	57.1
3.98×10^{24}	400.0	3.5	114.3
1.85×10^{24}	600.0	3.5	171.4
9.10×10^{23}	800.0	3.5	228.6
4.84×10^{23}	1000.0	3.5	285.7
1.09×10^{23}	800.0	2.0	400.0
1.09×10^{23}	800.0	2.5	320.0
3.07×10^{23}	800.0	3.0	266.7
9.10×10^{23}	800.0	3.5	228.6
2.51×10^{24}	800.0	4.0	200.0
3.01×10^{23}	7.2	0.04	180.0
2.70×10^{23}	36.0	0.2	180.0
2.74×10^{23}	72.0	0.4	180.0
4.48×10^{23}	360.0	2.0	180.0
2.96×10^{24}	720.0	4.0	180.0
[†] Source at 79.4-km depth, Plafker and Savage's ¹⁷ fault-plane parameters.			

that due to a step-function point source. Since the shear velocity of the 1066A model at 80-km depth is approximately 4.5 km/sec, we conclude that, for this event, the radiated energy is quite sensitive to rupture propagation velocity approaching the source region shear velocity.

D. W. McCowan
A. M. Dziewonski

G. RAYLEIGH-WAVE EXPLOSIVE MOMENTS AND SEISMIC ENERGIES FOR SIX U.S. EXPLOSIONS

Rayleigh-wave point-source theory¹⁹ provides a means of calculating the radiated Rayleigh-wave seismic energy if the moment tensor and time history of a source are known. In the case of a step function of explosive moment, the vertical component Rayleigh-wave spectrum will be:

$$A(r,z,\omega) = - \frac{Mk\Delta k}{2\pi\omega} w(\omega,k,z) \sqrt{\frac{1}{\pi kr}} [-ku(\omega,k,d) + \frac{dw(\omega,k,d)}{dz}] \quad (III-9)$$

In this expression, A is the zero-to-peak amplitude, M is the scalar explosive moment, k is horizontal wavenumber, ω is angular frequency, d is the source depth, and u and w are the Rayleigh-wave eigenfunctions normalized as described previously.¹⁹ In the interests of simplicity, the amplitude effects of attenuation and dispersion have been neglected. Figures III-18 to III-20 show this function plotted for the case of a 10^{23} dyn-cm explosive moment source at a distance of 100 km. Figures III-18 and III-19 show the effects of a change in source depth, while Fig. III-19 shows the results of Fig. III-18 seen through an LRSM (Long Range Seismic Measurements) LP recording system.

Values read from these graphs or similar versions computed for the required source depths can be used to estimate the explosive moment of an underground explosion from amplitude and period observations. The formula is:

$$M = \frac{A(\text{obs}) \sqrt{D}}{A(\text{graph}) 10} \times 10^{23} \text{ dyn-cm} \quad (III-10)$$

where D is the source distance in kilometers. Combining Eq. (III-10) with the Prague formula for M_s , and using the value in Fig. III-18 at 20-sec period, implies the following surface-wave magnitude-moment relation:

$$M_s = \log(M \times 10^{-22}) + 1.16 \log \Delta + 0.80 \quad (III-11)$$

where Δ is the epicentral distance in degrees, and M is again the explosive moment.

The arguments used previously²⁰ to derive an energy-moment tensor relation appropriate to free oscillation seismology can be easily generalized to Rayleigh waves. The resulting expression is

$$E = \frac{1}{2} \sum_{m=-2}^{+2} \int_0^\infty k dk \sum_j \frac{|M:S_m^{R+}(\omega_j,k,d)|^2}{2\pi\omega_j^2 I_R(\omega_j,k)} \quad (III-12)$$

which is valid for a step-source time function. Here, M is the moment tensor of the source, S_m^{R+} is the set of Rayleigh-wave strains, I_R is the normalization integral, and j is the mode index. The Rayleigh-wave strains can either be calculated by using a surface-wave-dispersion program or, for a homogeneous halfspace, be expressed analytically. In the latter case,²¹ the

TABLE III-3
PUBLISHED INFORMATION ON NTS EXPLOSION AND COMPUTED RESULTS

Shot ⁽¹⁾	Date ⁽¹⁾	Location ⁽¹⁾	Depth ⁽¹⁾ (km)	Geology ⁽¹⁾	Yield ⁽¹⁾ (kT)	Explosive Moment (dyn-cm) $\times 10^{23}$	Step-Function ⁽²⁾ Energy (kT)	Scale ⁽³⁾ Length (km)	Rise ⁽⁴⁾ Time (sec)
Half Beak	6/30/66	Pahute Mesa	0.88	Rhyolite	300	49 ± 32	400.0	4.6	1.4
Greeley	12/20/66	Pahute Mesa	1.23	Tuff	825	165 ± 190	1800.0	8.0	2.4
Scotch	5/23/67	Pahute Mesa	1.00	Tuff	150	33 ± 29	160.0	4.4	1.3
Knickerbocker	5/26/67	Pahute Mesa	0.63	Rhyolite	71	20 ± 16	200.0	4.7	1.4
Gasbuggy	12/10/67	Dulce, NM	1.29	Shale	29	3.6 ± 2.2	0.73	0.77	0.23
Rulison	9/10/69	Rulison, CO	2.57	Sandstone	40	3.3 ± 1.7	0.08	—	—

(1) Taken from Ref. 23.

(2) 1 kT = 4×10^{19} ergs.

(3) = cT.

(4) Assuming c = 3.3 km/sec.

resulting energy density consists of three terms, of the form:

$$\omega^2 e^{-A\omega d} \quad (III-13)$$

Each one of these decays at both ω extremes. The energy for a homogeneous Poisson halfspace can be integrated to give an exact answer for the radiated energy:

$$E = \frac{(0.196)M^2}{\mu d^3} \quad (III-14)$$

However, previous free-oscillation results^{22,24,25} show that a step function in applied moment produces an infinite radiated energy. Equation (III-14) shows that, for fundamental-mode Rayleigh waves, this only happens at zero source depth. For nonzero source depths, the exponential in Eq. (III-13) makes the energy finite. In other words, very-high-frequency Rayleigh waves propagate between the free surface and the source and are therefore poorly excited. Instead of relying on this source-depth effect to limit the high-frequency energy spectrum, it is prudent to include the possibility of a ramp-source time function. The corresponding expressions to Eqs. (III-12) and (III-14) are:

$$E = \frac{1}{2} \sum_{m=-2}^{+2} \int_0^\infty k dk \sum_j \frac{|M: S_m^{R+}(\omega_j, k, d)|^2}{2\pi\omega_j^2 I_R(\omega_j, k)} \left[\frac{\sin(\omega_j T/2)}{\omega_j T/2} \right]^2 \quad (III-15)$$

and

$$E = \frac{(0.196)M^2}{\mu d^3} \left[\frac{2.2909}{4.8698 + 1.6950x^2} - \frac{3.0475}{1.9103 + 1.2408x^2} + \frac{1.0343}{0.4867 + 0.7866x^2} \right] \quad (III-16)$$

$x = cT/d$

where T is the ramp time. The bracketed quantity, denoted by $\Sigma(x)$, is plotted in Fig. III-21.

As can be seen, increasing the ramp time serves to substantially decrease the radiated energy.

The results of estimating explosive moments and computing radiated energies from Eqs. (III-9) and (III-16), respectively, are given in Table III-3. These are for a selection of six U.S. explosions described as part of the LRSM program.²⁵⁻³⁰ In applying Eq. (III-9), a structure appropriate to the NTS was used.³¹ The explosive moments and their standard deviations were computed from all the nonquestionable Rayleigh-wave data reported for these six explosions. No attempts were made to remove anomalously high or low values (which were clearly evident), nor were any attempts made to reduce the impact on the average of very distant stations. A value of $\mu = 4 \times 10^{11}$ dyn/cm², deemed characteristic of sedimentary crustal rocks, was used in all the analyses.

The energies in Table III-3 are on the order of, or slightly higher than, the announced yields for NTS explosions. The two gas stimulation explosions, Gasbuggy and Rulison, produce energy estimates much lower than the announced yields. These, of course, are all for the step-function source. In an ad hoc attempt to deduce the correct source ramp time, scale lengths ($=cT$) were chosen which reduced the calculated step-function energy to 1 percent of the announced yield. This was thought to be a representative number based on previous work.³² The resulting ramp times are all near 1.5 sec for the NTS events, except that for the Greeley explosion. Unfortunately, its explosive moment is the most poorly determined example in the group. Again, the

TABLE III-4

PARAMETERS FOR pP AND SLAPDOWN PHASES DETERMINED BY (a) BAKUN AND JOHNSON³⁴
 AND (b) KING ET AL.³⁵ CORNER FREQUENCIES WERE CALCULATED FROM KING'S DATA.
 m_b AND M_s ARE NEIS MAGNITUDES.

	Amplitude Ratio		Time Delay (sec)		Corner Frequency (Hz)	Yield (kT)	m_b	M_s
	pP/P	Slapdown/P	pP/P	Slapdown/P				
	-0.3	+0.3	0.5	0.9	1.62	85	6.1	3.9
Longshot (b)	-0.7	+0.7	0.8	1.4	-	-	-	-
	-0.5	+0.4	0.8	1.4	1.21	~1000	6.5	4.9
Milrow	-0.6	+0.8	1.2	1.9	-	-	-	-
	-0.4	+0.4	1.1	1.9	0.971	5000	6.8	5.7
Cannikin	-0.6	+0.8	1.2	1.9	-	-	-	-
	-0.4	+0.4	1.1	1.9	0.971	5000	6.8	5.7

gas stimulation explosions stand out as having substantially lower ramp times. In fact, the computed step-function energy for Rulison is already below 1 percent of the announced yield.

An obvious conclusion of this work is that the source time function for explosions remains virtually unknown. Observed Rayleigh-wave spectra corrected for the recording system response³⁰ generally show that the energy peaks above 1/10 Hz. Since this is in the rejection band of the anti-microseism filter, there isn't much chance of recovering the source time function from presently available data. What is needed is a representative sample of broadband Rayleigh-wave seismograms recorded on reasonably near-in stations. One good possibility here is to modify the Albuquerque SRO by reducing the gain and removing the anti-microseism filter. It could then be used to observe NTS explosions which, by chance, propagate to Albuquerque across a relatively simple and homogeneous structure: the Colorado Plateau. These recordings could then be analyzed along the lines of Dziewonski and Gilbert's³³ work on deep South American earthquakes. The result of such endeavors should be an accurate determination of the explosive moment time histories for NTS explosions, which may also lead to more accurate estimates of the radiated seismic energies.

D. W. McCowan

H. YIELD VERIFICATION USING LONG-PERIOD P WAVES FROM EXPLOSIONS

At WWSSN stations, intermediate- to large-yield nuclear explosions produce LP P waves which are extremely simple in shape. Although these waves are not usually seen for yields much less than 100 kT, their simple shape and generally smaller amplitude scatter at large yield, compared with SP records, allow an alternate way to examine explosion source functions and seismic scaling with yield.

Figures III-22(a), (b), and (c) show plots of LP and SP amplitudes in microns for three large explosions in different test areas. These amplitudes were measured peak-to-peak on available WWSSN records, and corrected only for instrument gain at 1 sec for SP stations and at 15 sec for LP stations. Except for the Novaya Zemlya data, in Fig. III-22(a), the LP amplitudes are mostly greater than the SP amplitudes, with a slope LP vs SP less than 1. For both the Novaya Zemlya and Cannikin tests, the LP amplitudes have an order-of-magnitude less scatter than the SP amplitudes.

It is interesting that the LP amplitudes for Cannikin are, on the average, about half-a-magnitude larger than the Novaya Zemlya LP amplitudes, although the m_b values assigned by the NEIS were the same. This observation and the larger Cannikin yield suggest that the Cannikin m_b is underestimated.

In order to explain the pattern of SP and LP amplitudes, we investigated the effect of explosion source functions and earth attenuation on synthetic SP and LP records. Because our knowledge of site parameters for Novaya Zemlya explosions is limited, we chose the three U.S. Amchitka tests - Longshot, Milrow, and Cannikin - which have a wide range of known yields and depths.

Table III-4 contains source parameters for pP/P and slapdown/P phases obtained by Bakun and Johnson³⁴ and by King *et al.*³⁵ from SP spectral analysis.

Although the delay times for pP and slapdown phases relative to P agree between the two studies, the relative amplitudes do not. In particular, pP and slapdown phases have about equal and opposite amplitudes significantly less than 1.

Synthetic LP WWSSN records for Cannikin were calculated to compare with actual waveforms. Included in the records are Bakun and Johnson's parameters for the relative P, pP, and slapdown amplitudes, an explosion source function given by Blake³⁶ with a corner frequency of 0.971 obtained from King's results, a causal attenuation operator, and the WWSSN LP response.

Figure III-23(a) shows the synthetic waveforms for the P phase alone, and the effects of adding pP and slapdown phases. Figure III-24 displays several LP recordings of Cannikin, and they are surprisingly impulsive. Of particular interest are the equal positive and negative swings in the first motion, and the lack of strong later phases in the first few seconds. This seems to imply that the pP/P amplitude ratio must be closer to one, and the slapdown amplitude nearer to zero than suggested by Bakun and Johnson's study. The slapdown phase shown in the synthetic record is not visible at all on most of the LP explosion records.

In Fig. III-23(b), synthetic LP records for Cannikin are displayed assuming a pP/P amplitude ratio of -1.0 and retaining the slapdown/P amplitude ratio of 0.8. The synthetic records which contain only P and pP phases adequately explain the shape and pulse width of the observed data. In Fig. III-23(c), synthetic SP records are shown for Cannikin using the same source parameters. These calculations use the formulation for the WWSSN SP response obtained by Burdick and Mellman,³⁷ which includes the effect of transducer inductance at high frequencies.

Synthetic SP and LP records were computed for Cannikin, Milrow, and Longshot for a variation of attenuation parameter $t^* = (\text{travel time})/(\text{average } Q)$. The far-field displacement spectrum for each explosion was normalized to equal the yield at 0 frequency, and given the corner frequency listed in Table III-4. Instrument responses were normalized to 1.0 at 1 and 15 sec for SP and LP records, respectively. P amplitudes, peak-to-trough, were measured to obtain relative amplitudes of LP and SP phases.

These synthetic amplitudes are displayed in Fig. III-25. The trend of SP vs LP amplitudes is very similar for the three explosions in spite of variations in source corner frequency. This trend is controlled primarily by attenuation variations which affect the SP amplitudes more severely than the LP amplitudes. Thus, attenuation alone may explain much of the trend of the real LP and SP data in Figs. III-22(a-c). In particular, the Novaya Zemlya data show a cross-over region where LP amplitudes become less than SP amplitudes. From the synthetic cases this would be expected along paths with $t^* \lesssim 0.5$, a reasonable value for high Q teleseismic paths.

Another feature of the synthetic data is that attenuation differences may cause SP amplitudes to overlap from explosion-to-explosion, whereas the LP amplitudes remain separated. This would decrease the reliability of SP magnitudes based on uneven station coverage.

Taking amplitude ratios of the synthetic data for pairs of shots, we obtain the curves shown in Fig. III-26(a) as a function of t^* . As attenuation increases, both LP and SP amplitude ratios converge to the ratio of yields used in the calculations.

Figure III-26(b) shows amplitude ratios calculated from real data of various periods. On LP records we measured 32 Cannikin LP amplitudes, and 8 Milrow amplitudes. Of these measurements, Cannikin and Milrow were measured at 7 common stations including COL which also recorded Longshot. Amplitude ratios at common stations are:

Milrow/Cannikin	0.26 ± 0.07
Longshot/Milrow	0.089
Longshot/Cannikin	0.023

These ratios are plotted in Fig. III-26(b) as crosses. In spite of the small number of measurements, these ratios agree well with the yield ratios and with ratios expected from NEIS M_s differences which are measured at periods from 10 to 20 sec. Amplitude measurements predicted from NEIS m_b differences clearly do not agree with the other data and must be considered unreliable. Specifically, m_b for both Milrow and Cannikin are probably underestimated. This is suggested by SP measurements at seven common LRSM stations by von Seggern and Blandford.³⁸ They computed the amplitude ratios displayed as solid points in Fig. III-26(b). These ratios are much closer to the yield ratios than are the ratios based on NEIS m_b .

This preliminary analysis of LP data from explosions is promising. We intend to examine data from all test areas and concentrate on the yield range of 100 to 1000 kT.

C. W. Frasier
T. J. Fitch

I. ANOMALOUS m_b VS YIELD FOR LONGSHOT, MILROW, AND CANNIKIN

Using LP and SP data, we are investigating the difficulties of estimating consistent yields for large explosions. In Sec. H above, we indicated that relative LP amplitudes for body waves from Longshot, Milrow, and Cannikin could be used to estimate the relative yields of the three explosions. These amplitudes were not divided by their apparent period, nor were they corrected for instrument response.

Figure III-27 shows log amplitude as a function of yield for Milrow and Cannikin data, normalized by the Longshot data. Different types of actual and theoretical amplitudes are shown, both LP and SP. Using the scaled, theoretical ω^{-2} source spectra of the previous section, we calculated amplitudes of Milrow and Cannikin relative to Longshot at 0.05, 1.0, and 2.0 Hz frequencies. In the broadband from 0.05 to 1.0 Hz, the theoretical ratios vary insignificantly and agree quite well in Fig. III-27 with amplitude variations expected from differences in NEIS M_s , measured from 15 to 20 sec, and LP body wave measurements at periods as small as 2 to 3 sec. Therefore, a consistent trend of amplitude proportional to yield 1.0 fits the data from periods $\gtrsim 2$ to 20 sec.

At shorter periods $\lesssim 1$ sec the amplitudes are proportional to a smaller power of yield. For example, at 2 Hz the theoretical amplitudes vary as yield ~ 0.75 because the corner frequencies assumed in the source functions for Milrow and Cannikin are both < 2.0 Hz. Von Seggern and Blandford³⁸ measured the amplitudes of the first quarter-cycle of the SP records at seven LRSM stations. They obtained the following ratios:

Milrow/Longshot	6.68 ± 0.86
Cannikin/Longshot	15.76 ± 2.32

Logarithms of these ratios are shown in Fig. III-27 as black circles, and follow the trend of the theoretical curve at 2 Hz. Although the first motion amplitudes contain frequencies higher than 1 Hz, it is uncertain whether the spectra peak nearer to 2 and 1 Hz. If not, the data of von Seggern and Blandford may indicate a faster falloff than ω^{-2} in the source spectra beyond the corner frequencies.

Expected log amplitudes based on NEIS and ISC m_b , assuming similar periods for each P wave, show a trend well below von Seggern and Blandford's results and must be considered suspect. Cannikin and Milrow m_b values are most certainly underestimated, due to a variety of problems in network detection, station bias, and inconsistent period measurements. These are

discussed in great detail by Basham and Horner.³⁹ They used the Canadian seismic network to estimate LP and SP magnitudes which do not involve dividing by pulse period. By including station biases for high-quality stations on the Canadian shield, Basham and Horner calculated SP magnitudes which give the log amplitude ratios shown in Fig. III-27 by black triangles. These values agree well with von Seggern and Blandford's amplitude ratios and verify the poor quality of NEIS m_b values.

Basham and Horner used an explosion source model by Haskell⁴⁰ to predict the LP and SP body phase amplitudes and the relative M_s values for the three Aleutian explosions. As in our study, they were able to match M_s variations based on the 0-Hz spectral level, which scales as yield 1.0. They could not, however, predict either the LP or SP amplitudes using the Haskell source model. Their discrepancy for SP amplitudes is similar to that shown in Fig. III-27, between the theoretical curve for 1.0 Hz and the black triangles and circles. At long periods, the scaled Haskell source functions predict a Cannikin/Longshot P-wave ratio about 0.4 magnitude units larger than the prediction in Fig. III-27.

One difficulty with the Haskell explosion model is that it predicts a far-field spectrum which decays as ω^{-4} above the corner frequency. This causes large explosions to have less high-frequency energy than small explosions. Most evidence,³⁸ however, suggests that ω^{-2} source models fit the explosion data better and are physically more plausible than Haskell's model.

It appears then that m_b as currently determined by the NEIS and ISC is particularly questionable for large explosions, and that more consistent yield determinations can be made by the combined use of M_s and LP P waves. It must be emphasized that if absolute rather than relative yields are to be obtained, a path-dependent magnitude M_s , as proposed by Marshall and Basham,⁴¹ must be used - particularly for explosions in different tectonic regions.

C. W. Frasier

REFERENCES

1. R. G. North, "Station Biases in Body-Wave Magnitude," *Bull. Seismol. Soc. Am.* (in press).
2. A. Douglas, P. D. Marshall, P. G. Gibbs, J. B. Young, and C. Blamey, "P Signal Complexity Re-examined," *Geophys. J. R. Astron. Soc.* 33, 195 (1973).
3. M. Barazangi and B. Isacks, "Lateral Variations of Seismic-Wave Attenuation in the Upper Mantle above the Inclined Earthquake Zone of the Tonga Island Arc: Deep Anomaly in the Upper Mantle," *J. Geophys. Res.* 76, 8493 (1971).
4. K. H. Jacob, "Global Tectonic Implications of Anomalous Seismic P Travel Times from the Nuclear Explosion Longshot," *J. Geophys. Res.* 77, 2556 (1972).
5. L. R. Johnson, "Array Measurements of P Velocities in the Lower Mantle," *Bull. Seismol. Soc. Am.* 59, 973 (1969).
6. K. Aki, "Scaling Law of Earthquake Source Time-Function," *Geophys. J. R. Astron. Soc.* 31, 3 (1972).
7. T. Hagiwara, "A Note on the Theory of the Electromagnetic Seismograph," *Bull. Earthquake Res. Inst.* 36, 139-164 (1958).
8. S. K. Chakrabarty and S. N. R. Choudhury, "Response Characteristics of Electromagnetic Seismographs," *Bull. Seismol. Soc. Am.* 54, 1445-1458 (1964).
9. L. Burdick and G. Mellman, "The Response of the WWSSN Short Period Seismometer," Division of Geological and Planetary Sciences Contribution No. 2628, CALTECH, Pasadena, CA (1976).
10. J. Mitchell and M. Landisman, "Electromagnetic Seismograph Constants by Least-Squares Inversion," *Bull. Seismol. Soc. Am.* 59, 1335-1348 (1969).
11. Seismic Discrimination SATS, Lincoln Laboratory, M.I.T. (30 June 1976), DDC AD-A032754/4.
12. G. E. Backus, "Geographical Interpretation of Measurements of Average Phase Velocities of Surface Waves over Great Circular and Great Semi-circular Paths," *Bull. Seismol. Soc. Am.* 54, 571-610 (1964).
13. H. Kanamori, "The Alaskan Earthquake of 1974: Radiation of Long Period Surface Waves and Source Mechanism," *J. Geophys. Res.* 75, 5029-5040 (1970).
14. K. Aki, "Generation and Propagation of G Waves from the Niigata Earthquake of June 16, 1964, 2, Estimation of Earthquake Moment, Released Energy, and Stress-Strain Drop from the G Wave Spectrum," *Bull. Earthquake Res. Inst. Tokyo Univ.* 44, 73 (1966).
15. F. Gilbert and A. M. Dziewonski, "An Application of Normal Mode Theory to the Retrieval of Structural Parameters and Source Mechanisms from Seismic Spectra," *Philos. Trans. R. Soc. Lond.* 278, 187-269 (1975).
16. A. Ben-Menahem, "Radiation of Seismic Surface Waves from Finite Moving Sources," *Bull. Seismol. Soc. Am.* 51, 401-435 (1961).
17. G. Plafker and J. C. Savage, "Mechanism of the Chilean Earthquakes of May 21 and May 22, 1960," *Geol. Soc. Am. Bull.* 81, 1001-1030 (1970).
18. H. Kanamori and J. J. Cipar, "Focal Process of the Great Chilean Earthquake of May 22, 1960," *Phys. Earth Planet. Int.* 9, 128-136 (1974).
19. D. W. McCowan, "Moment Tensor Representation of Surface Wave Sources," *Geophys. J. R. Astron. Soc.* 44, 595-599 (1976).
20. Seismic Discrimination SATS, Lincoln Laboratory, M.I.T. (31 December 1975), pp. 58-61, DDC AD-A025777/4.

21. G. Nadeau, Introduction to Elasticity (Holt, Rinehart & Winston, New York, 1964).
22. See Sec. F on p. 47 in this SATS.
23. D. L. Springer and R. L. Kinnaman, "Seismic Source Summary for U.S. Underground Nuclear Explosions, 1961-1970," *Bull. Seismol. Soc. Am.* 61, 1073-1098 (1971).
24. Seismic Discrimination SATS, Lincoln Laboratory, M.I.T. (30 June 1976), pp. 81-82, DDC AD-A032754/4.
25. D. M. Clark, "Long Range Seismic Measurements - Half Beak," Seismic Data Laboratory Report No. 171, Alexandria, VA (1966).
26. _____, "Long Range Seismic Measurements - Greeley," Seismic Data Laboratory Report No. 180, Alexandria, VA (1967).
27. _____, "Long Range Seismic Measurements - Scotch," Seismic Data Laboratory Report No. 200, Alexandria, VA (1967).
28. D. M. Clark, E. W. Moore, and D. H. von Seggern, "Long Range Seismic Measurements - Knickerbocker," Seismic Data Laboratory Report No. 208, Alexandria, VA (1968).
29. S. F. Thorpe, L. C. Lande, D. J. Glasscock, and F. P. Van Leer, "Long Range Seismic Measurements - Gasbuggy," Geotech Technical Report No. 68-7, Garland, TX (1968).
30. D. G. Lambert and R. O. Ahner, "Seismic Analysis of the Rulison Explosion," Seismic Data Laboratory Report No. 255, Alexandria, VA (1972).
31. Seismic Discrimination SATS, Lincoln Laboratory, M.I.T. (30 June 1976), pp. 40-42, DDC AD-A032754/4.
32. H. C. Rodean, "Nuclear-Explosion Seismology," U.S. Atomic Energy Commission Technical Report No. TID-25572 (1971).
33. A. M. Dziewonski and F. Gilbert, "Temporal Variation of the Seismic Moment and the Evidence of Precursive Compression for Two Deep Earthquakes," *Nature* 247, 185-188 (1974).
34. W. H. Bakun and L. R. Johnson, "The Deconvolution of Teleseismic P Waves from Explosions MILROW and CANNIKIN," *Geophys. J. R. Astron. Soc.* 34, 321-342 (1973).
35. C. Y. King, A. M. Abo-Zena, and J. N. Murdock, "Teleseismic Source Parameters of the Longshot, Milrow, and Cannikin Nuclear Explosions," *J. Geophys. Res.* 79, 712-718 (1974).
36. F. G. Blake, "Spherical Wave Propagation in Solid Media," *J. Acoust. Soc. Am.* 24, 211-215 (1952).
37. L. Burdick and G. Mellman, "The Response of the WWSSN Short Period Seismometer," unpublished contribution No. 2628, Seismological Laboratory, California Institute of Technology, Pasadena, CA.
38. D. von Seggern and R. Blandford, "Source Time Functions and Spectra for Underground Nuclear Explosions," *Geophys. J. R. Astron. Soc.* 31, 83-97 (1972).
39. P. W. Basham and R. B. Horner, "Seismic Magnitudes of Underground Nuclear Explosions," *Bull. Seismol. Soc. Am.* 63, 105-131 (1973).
40. N. A. Haskell, "Analytic Approximation for the Elastic Radiation from a Contained Underground Explosion," *J. Geophys. Res.* 72, 2583-2587 (1967).
41. P. D. Marshall and P. W. Basham, "Discrimination between Earthquakes and Underground Explosions Employing an Improved M_s Scale," *Geophys. J. R. Astron. Soc.* 28, 431-458 (1972).

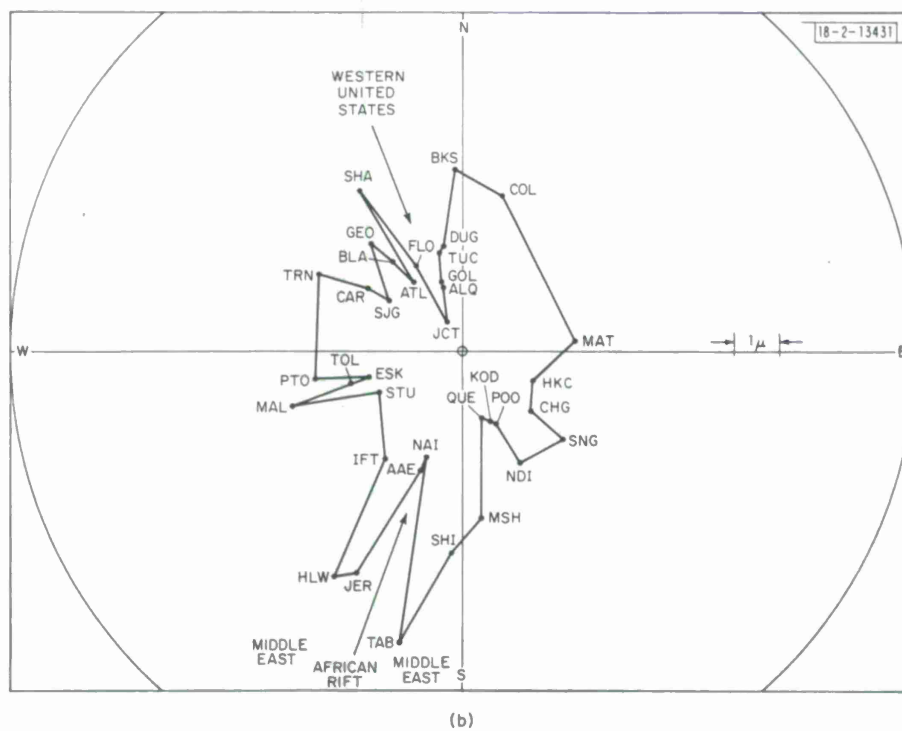
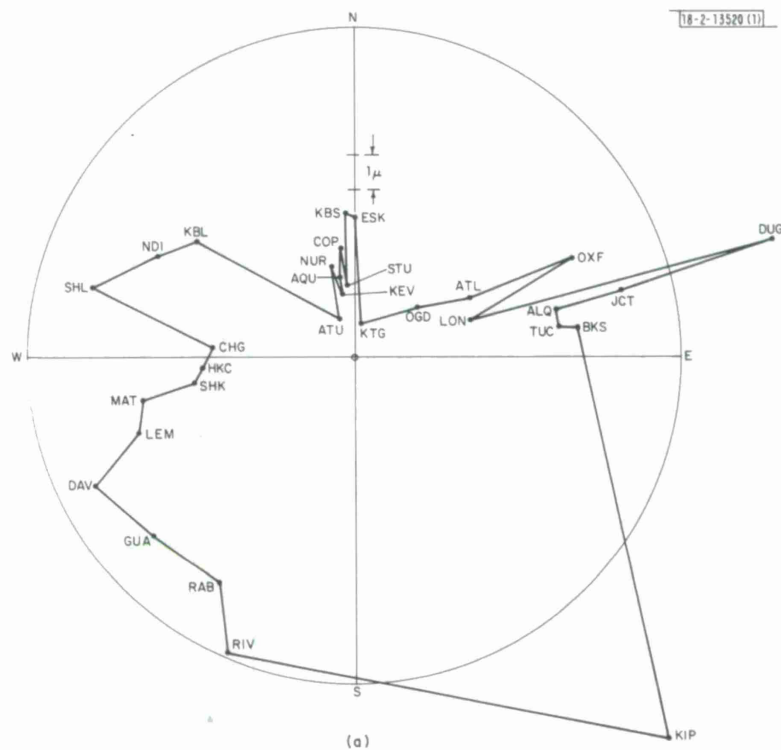


Fig. III-1. Amplitudes vs azimuth. All signals were recorded by LP instruments of WWSSN in distance range 30° to 90° and reduced peak-to-peak amplitudes in microns normalized to an arc distance of 60° . Corrections for spherical spreading were computed from earth model CIT20 (Ref. 5). Events used are (a) Cannikin explosion, and (b) Novaya Zemlya event (14 October 1970).

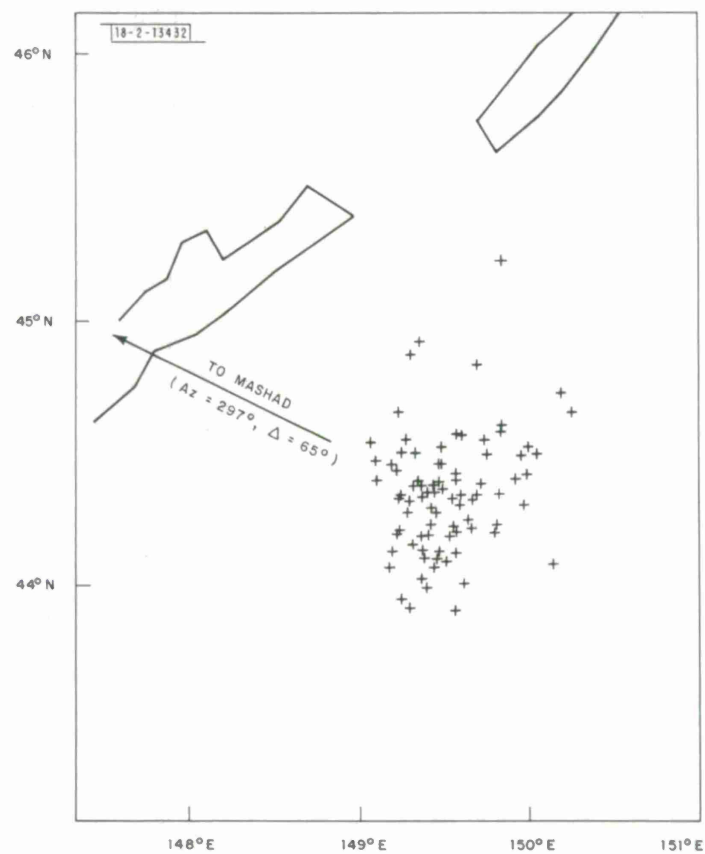


Fig. III-2. Relocated epicenters of Kurile aftershock sequence of 21 January - 10 February 1976.

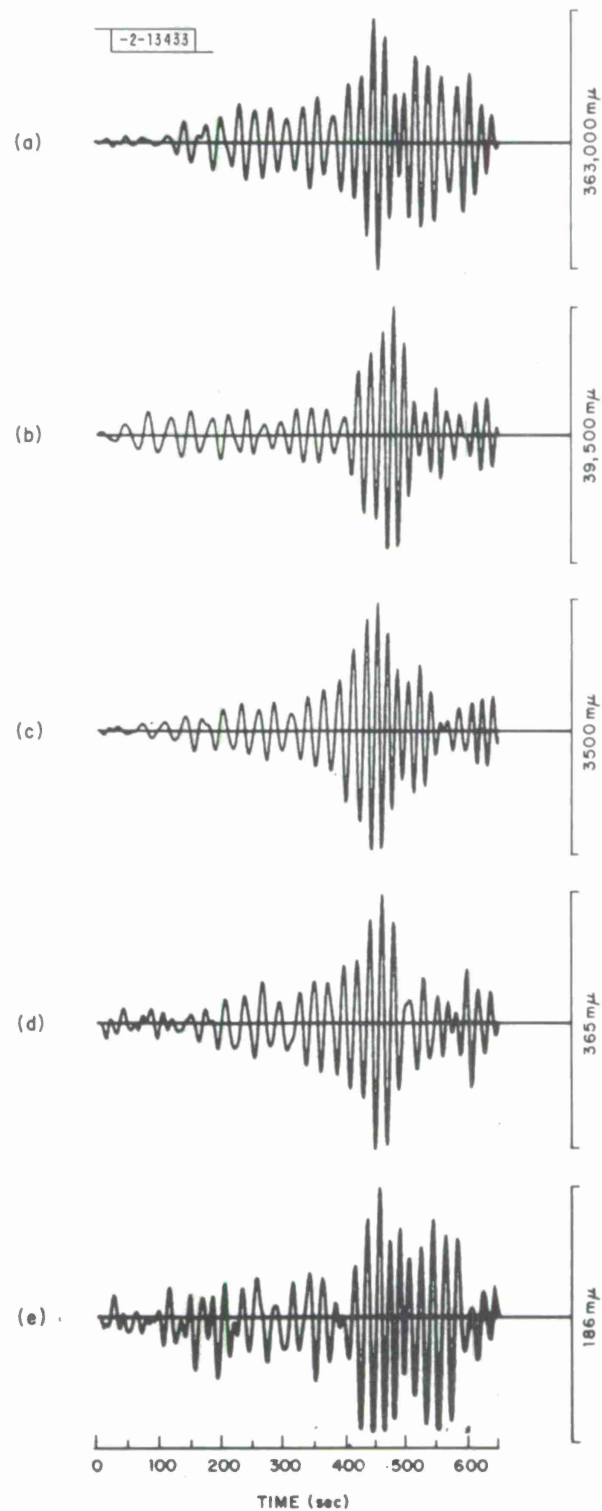


Fig. III-3. LP vertical Rayleigh-wave trains recorded at Mashad SRO from Kurile sequence, covering $3\frac{1}{2}$ orders of magnitude. All seismograms start at 2070 sec after origin time, and are of 640-sec duration.

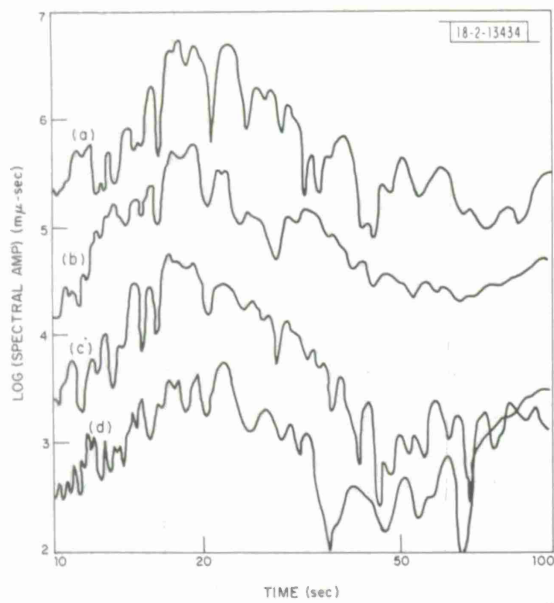


Fig. III-4. Spectra of seismograms (a) through (d) from Fig. III-3.

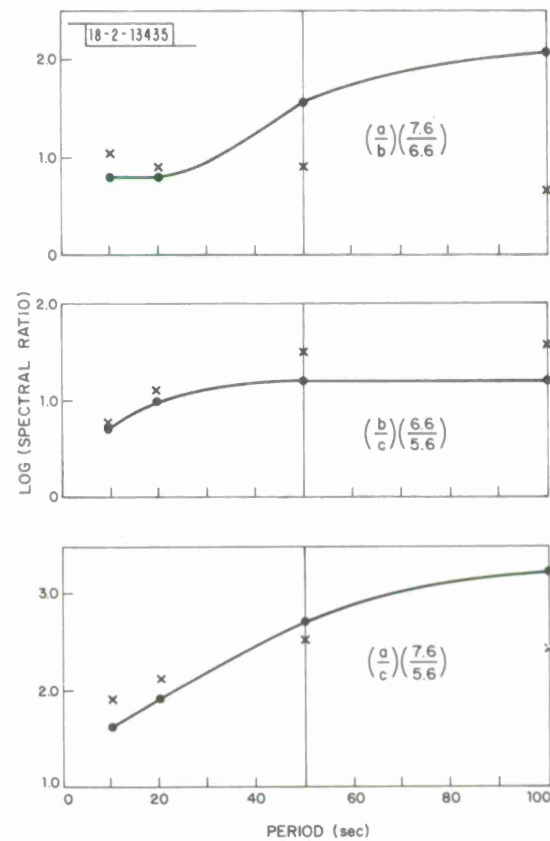


Fig. III-5. Spectral ratios of events (a/b), (b/c), and (a/c), calculated at $t = 10, 20, 50,$ and 100 sec (crosses), together with ratios predicted by ω^2 law.

Fig. III-6. Bodine motor drive and pulley arrangement.

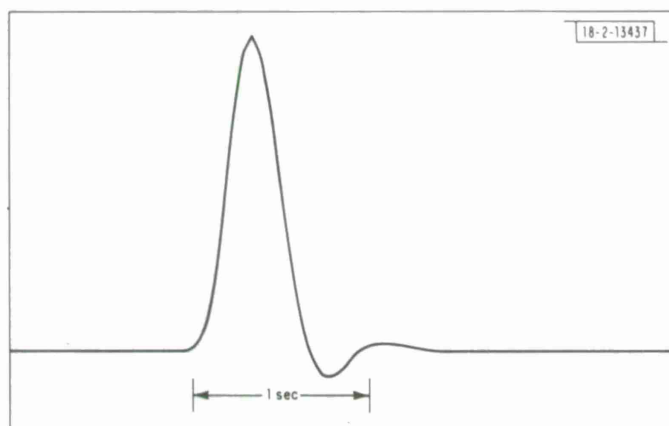
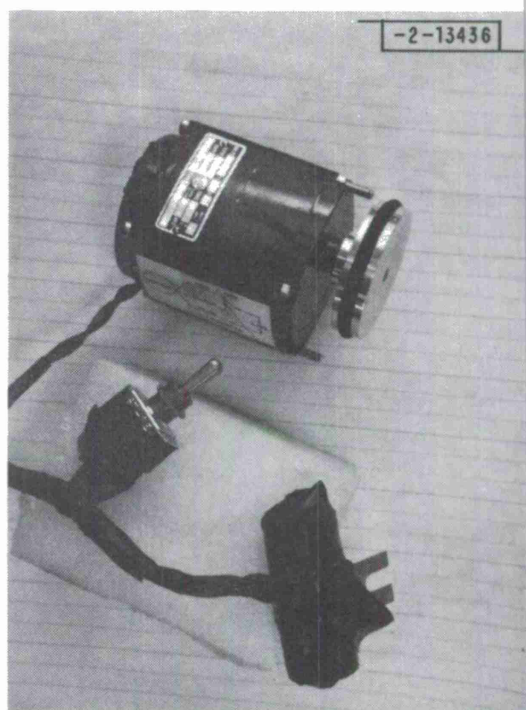


Fig. III-7. Final averaged WWSSN SP calibration pulse recorded at Weston Seismic Observatory.

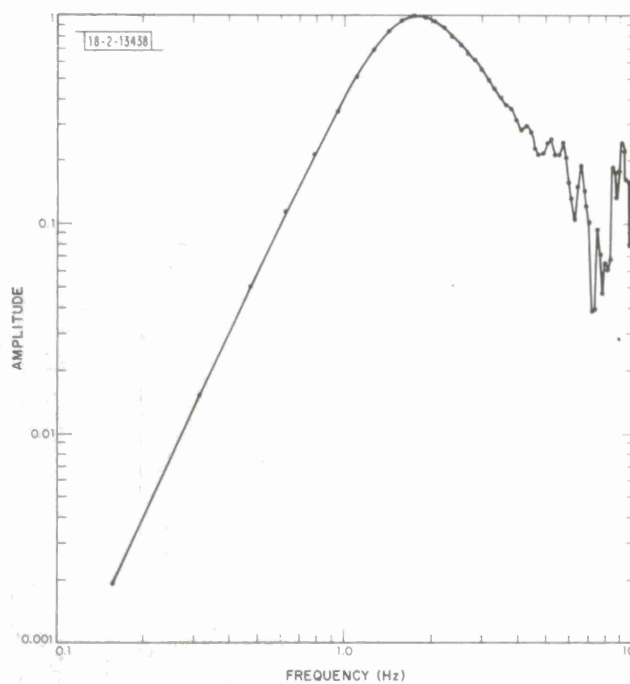


Fig. III-8. System amplitude response computed from pulse in Fig. III-7.

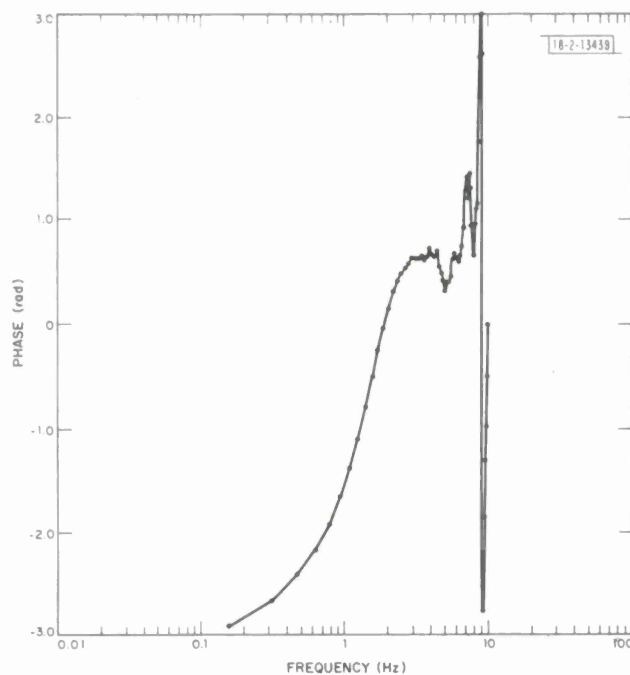


Fig. III-9. System phase response computed from pulse in Fig. III-7.

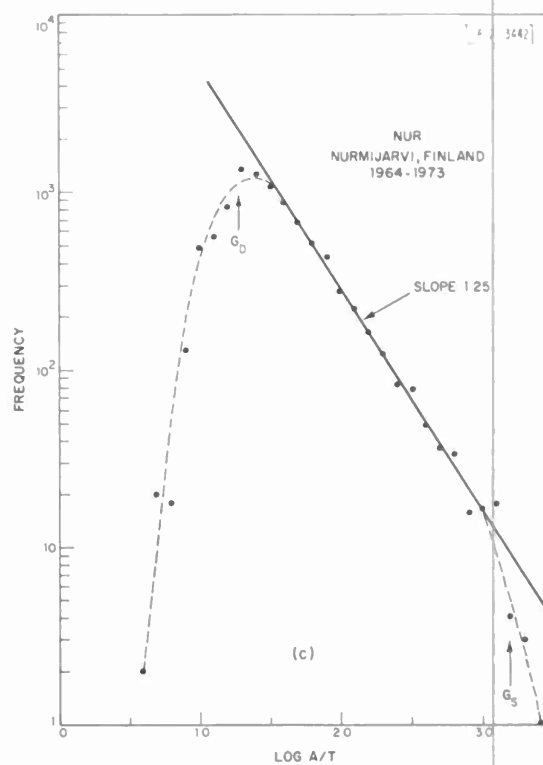
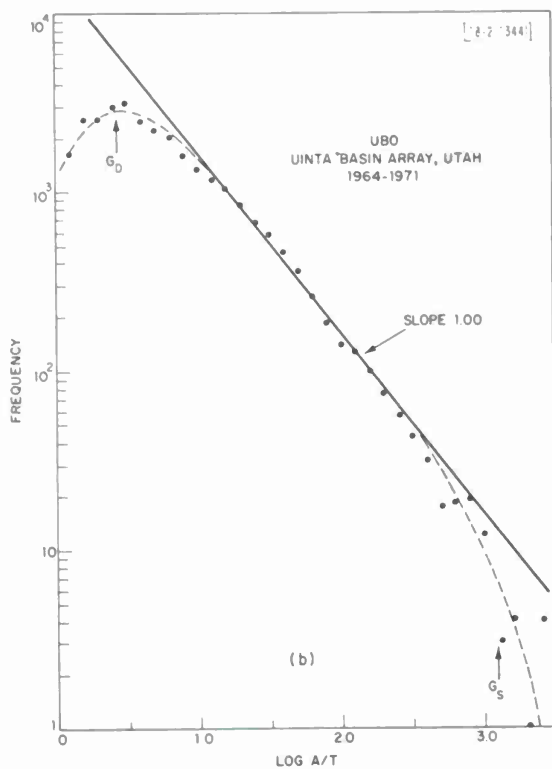
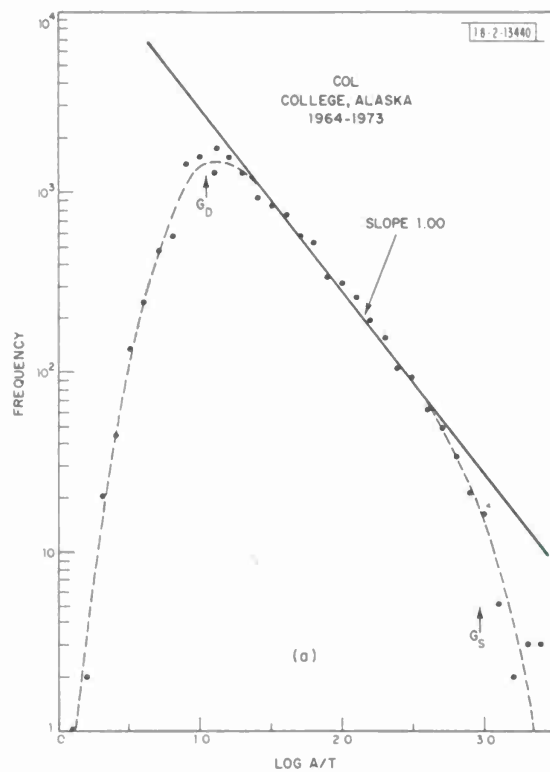


Fig. III-10(a-c). Observed variation of frequency with $\log A/T$ for three stations, using ISC Bulletin data. Solid line is an inferred seismicity relation, and dashed lines are interpretations of station detection capability. G_D is 50-percent detection threshold; G_S is 50-percent saturation threshold.

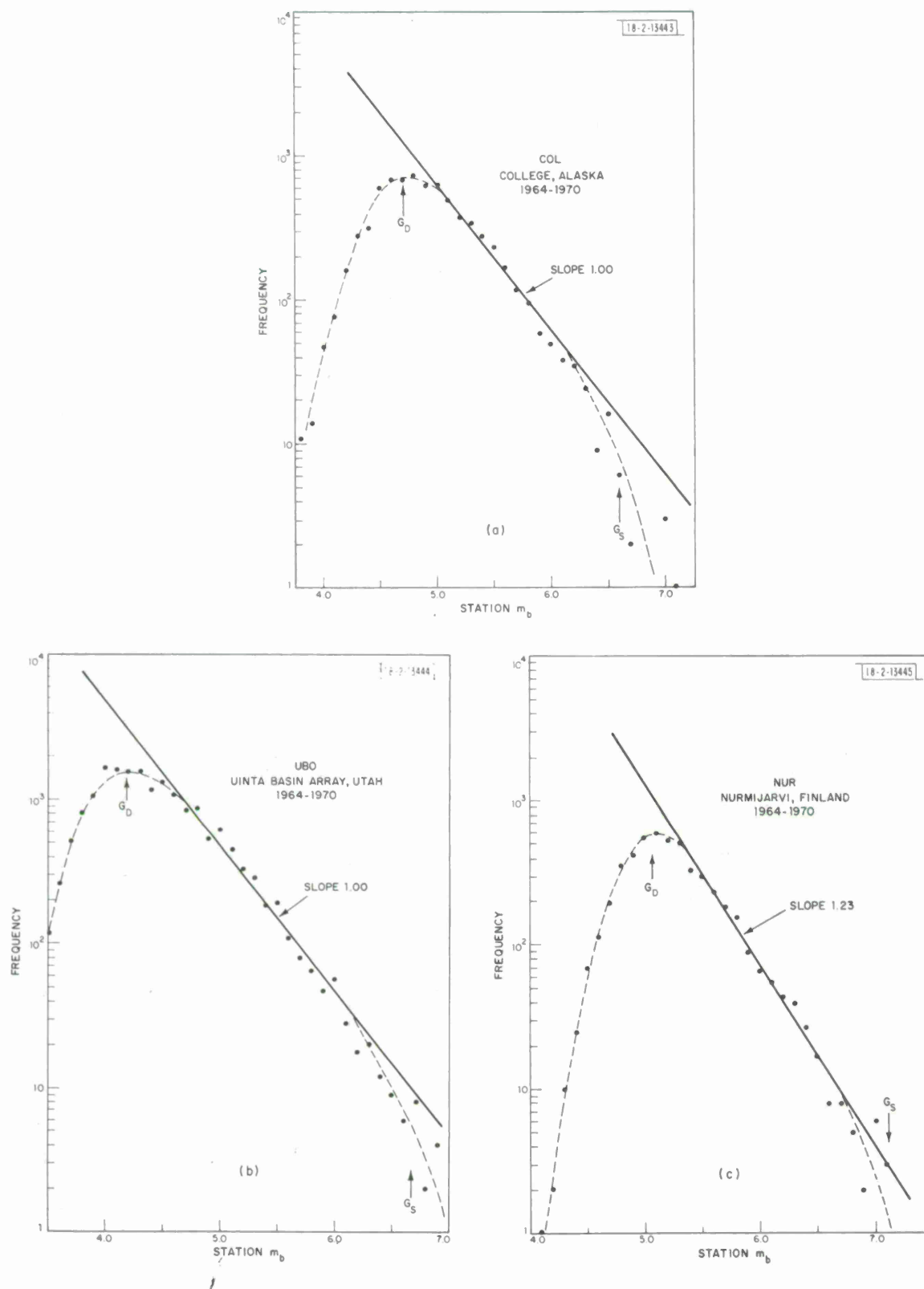


Fig. III-11(a-c). Observed variation of frequency with station magnitude m_b , for events in distance range 30° to 90° , using ISC Bulletin data. For other symbols, see Fig. III-10.

Fig.III-12. Comparison of magnitude distribution of events input into simulated network program, with magnitude distribution of events detected. G_S and G_D are 50-percent detection and saturation thresholds of network.

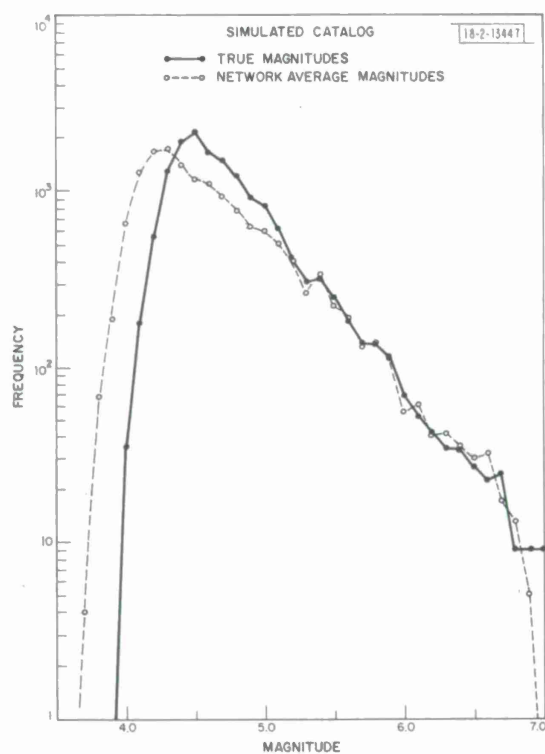
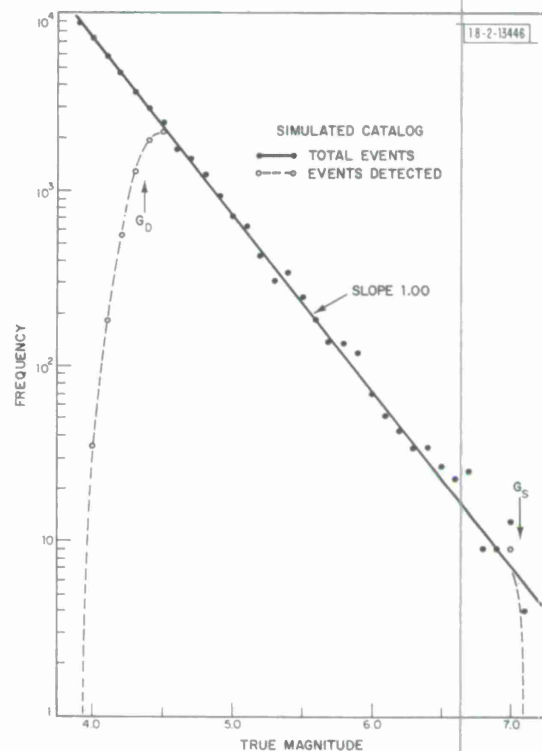


Fig.III-13. Comparison of true magnitudes of events detected by simulation program with network magnitudes, computed as average station magnitude for those stations detecting each event.

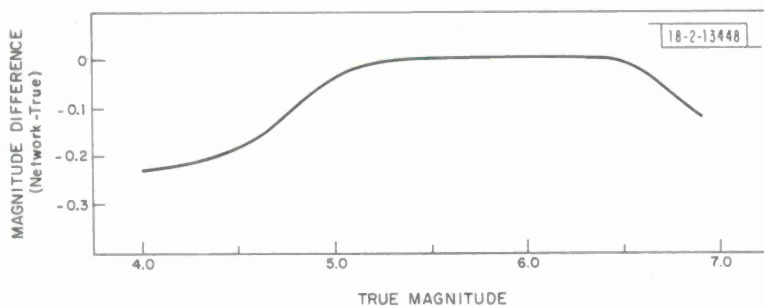


Fig. III-14. Average values of difference between network average magnitude and true magnitude, plotted as a function of true magnitude.

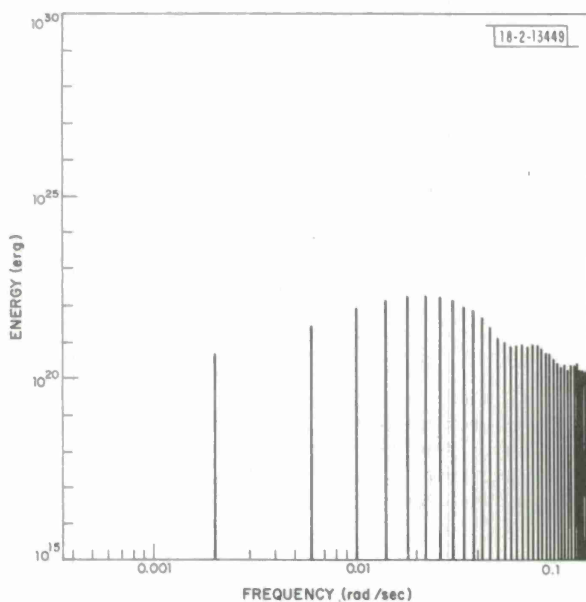


Fig. III-15. Spectral distribution of radiated energy for 1960 Chilean earthquake for an 800-km fault with 2.0-km/sec rupture velocity. Line source at 79.4-km depth using Plafker and Savage's¹⁷ fault-plane solution.

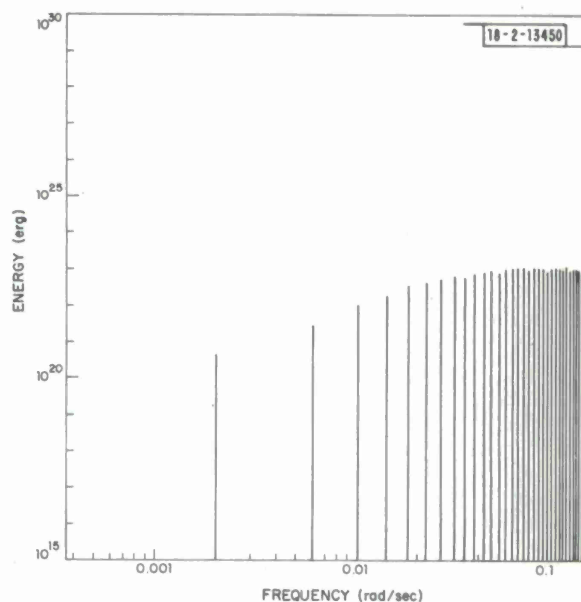


Fig. III-16. Spectral distribution of radiated energy for 1960 Chilean earthquake for a 720-km fault with 4.0-km/sec rupture velocity. Line source at 79.4-km depth using Plafker and Savage's¹⁷ fault-plane solution.

Fig. III-17. Spectral distribution of radiated energy for 1960 Chilean earthquake for an 800-km fault with 3.5-km/sec rupture velocity. Line source at 79.4-km depth using Plafker and Savage's¹⁷ fault-plane solution.

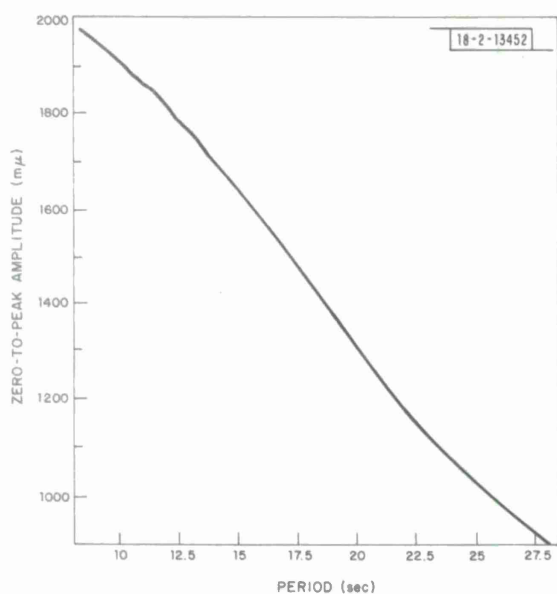
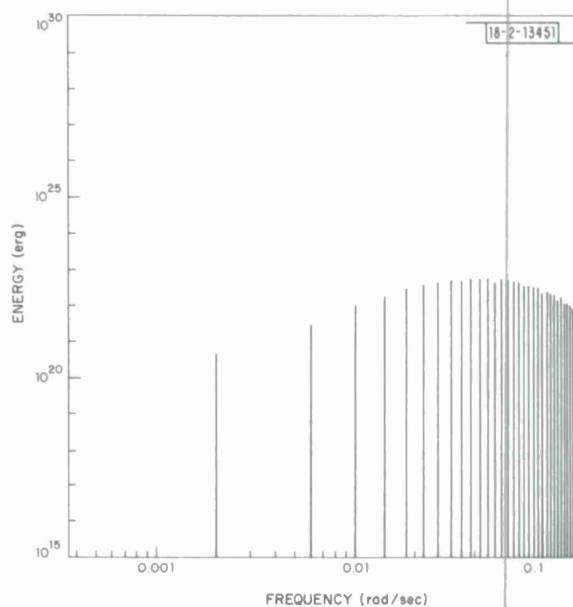


Fig. III-18. Amplitude vs period for a 10^{23} dyn-cm explosive moment source 1 km deep at 100-km distance. (Instrument response not included.)

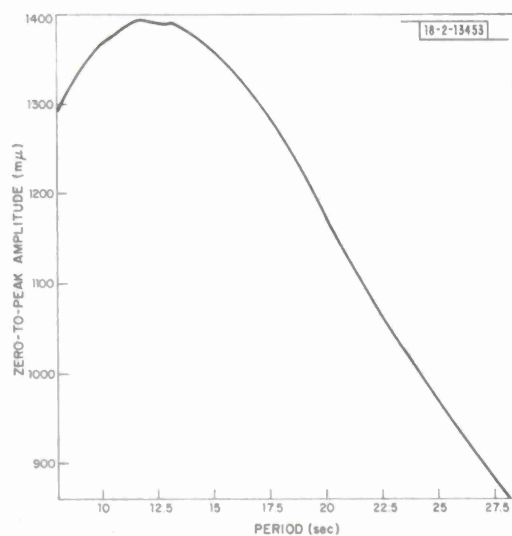


Fig. III-19. Amplitude vs period for a 10^{23} dyn-cm explosive moment source 3 km deep at 100-km distance. (Instrument response not included.)

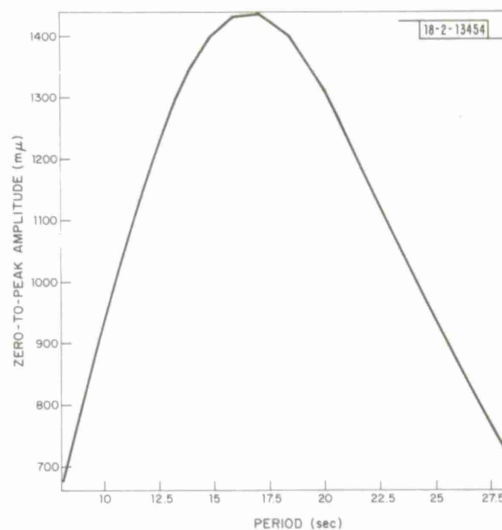


Fig. III-20. Amplitude vs period for a 10^{23} dyn-cm explosive moment source 1 km deep at 100-km distance as seen through LRSM LP recording system.

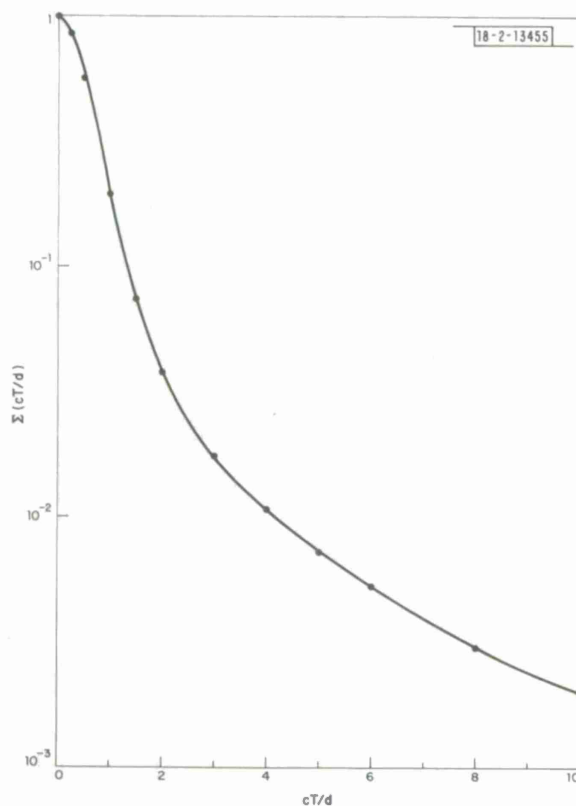


Fig. III-21. Σ factor for ramp-source time function in a homogeneous Poisson halfspace.

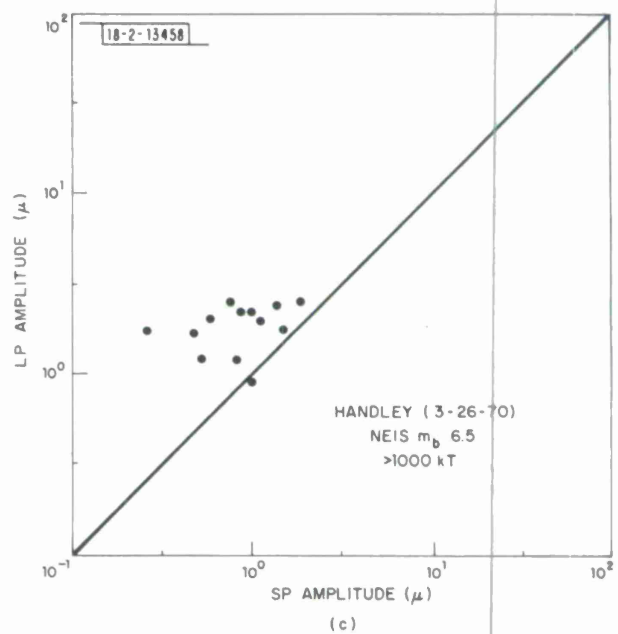
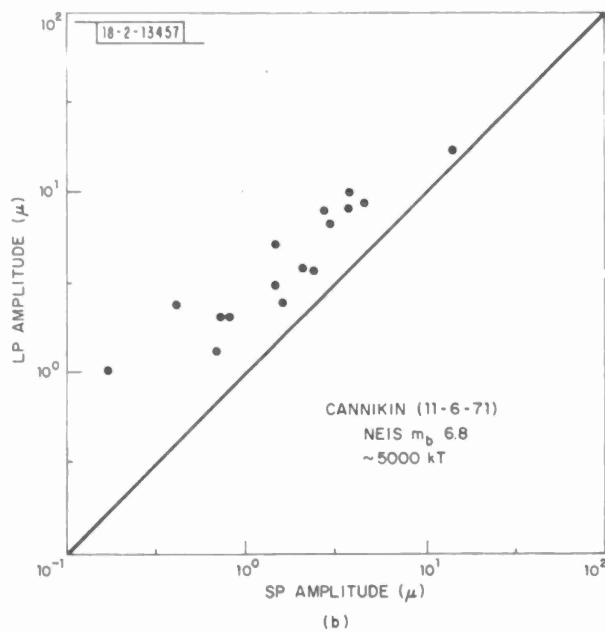
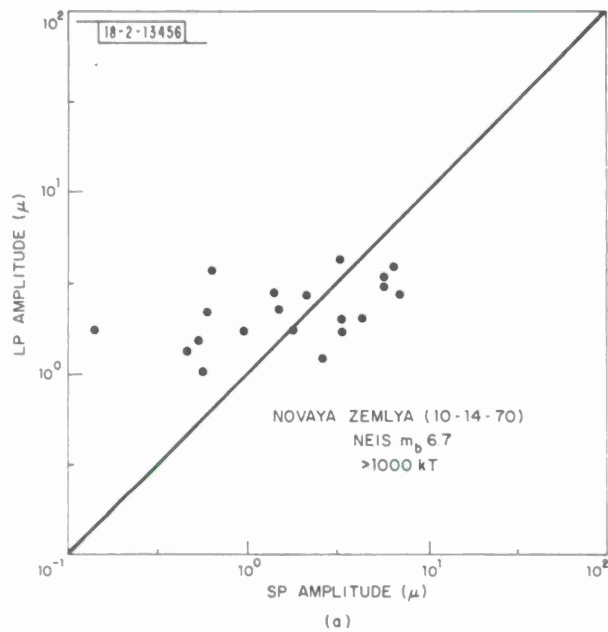


Fig. III-22. LP and SP P amplitudes measured at WWSSN stations for three large explosions at (a) Novaya Zemlya, (b) Amchitka Island, and (c) NTS.



Fig. III-23. Synthetic P waves from Cannikin. Includes explosion source spectrum, earth attenuation pP and slapdown phases, and WWSSN response. (a) LP synthetic record with amplitude ratios $pP/P = -0.6$, $slapdown/P = 0.8$, and $t^* = 0.5$. (b) LP synthetic records with $pP/P = -1.0$, $slapdown/P = 0.8$, and three attenuation parameters. (c) Same as (b), except recorded on SP seismograph.

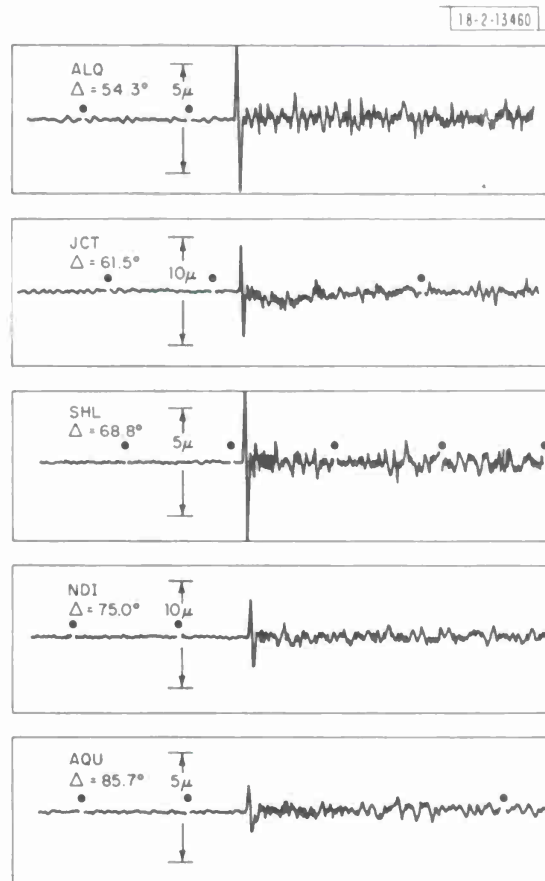


Fig. III-24. Examples of WWSSN LP recordings of P waves from Cannikin.

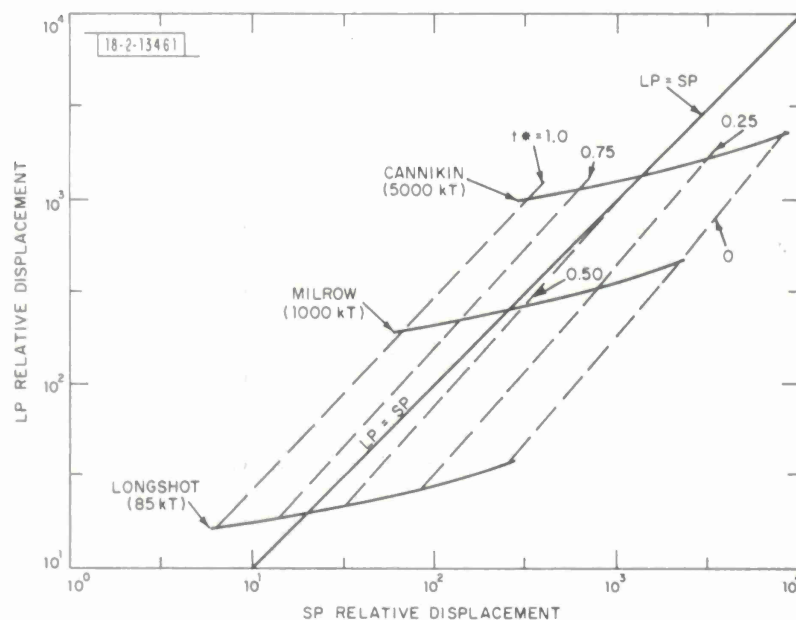


Fig. III-25. Relative LP and SP amplitudes predicted for Cannikin, Milrow, and Longshot. Source spectra have corner frequencies given in Table III-4, and have 0-Hz levels scaled by yield in kilotons. Dashed lines join amplitude points of equal attenuation parameter t^* .

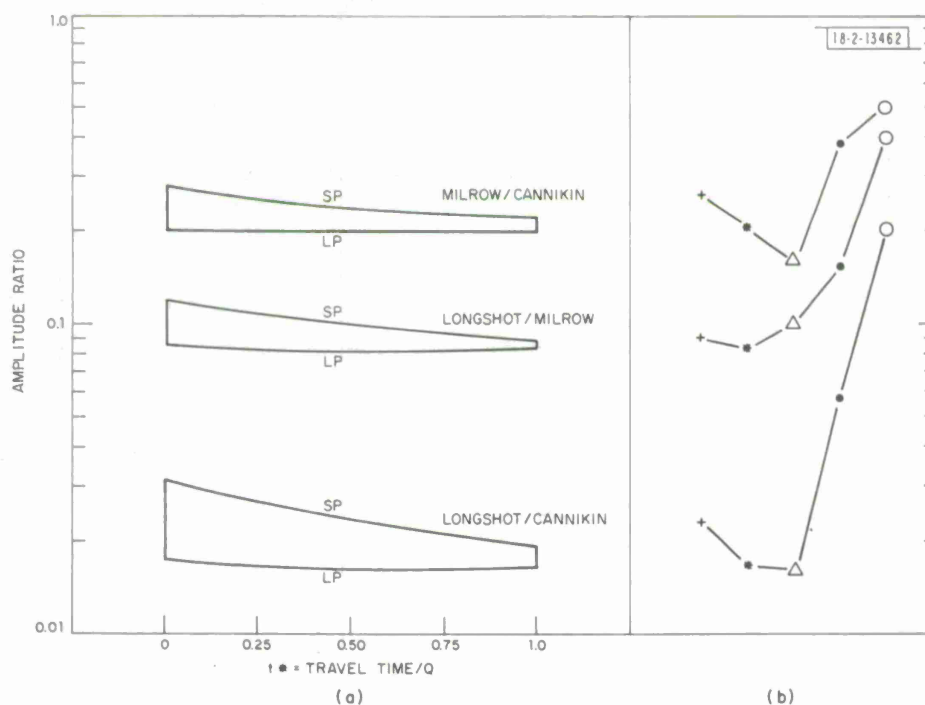


Fig. III-26. (a) Theoretical amplitude ratios for pairs of explosions calculated from Fig. III-25, as a function of t^* . (b) Measured LP amplitude ratios (+), SP ratios determined by von Seggern and Blandford³⁸ (●), yield ratios (*), amplitude ratios inferred from NEIS M_s (Δ) and m_b (\odot).

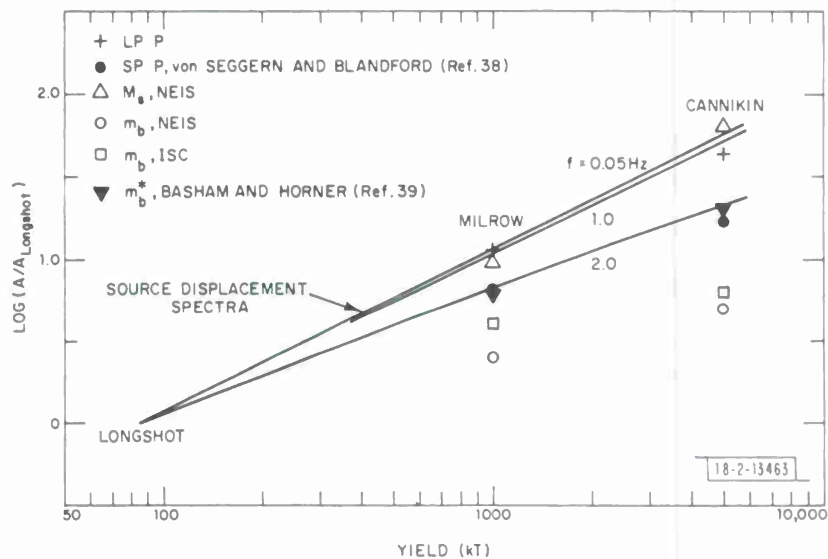


Fig. III-27. Log amplitude as a function of yield for Milrow and Cannikin seismic phases relative to Longshot. Amplitudes are based on several SP body-wave magnitudes, surface-wave magnitudes, and some LP and SP amplitude measurements. Curves show low amplitude variations at 0.05, 1.0, and 2.0 Hz predicted by an ω^2 explosion source model described in text.

IV. MISCELLANEOUS STUDIES

A. MULTIPLE-CHANNEL MAXIMUM-ENTROPY SPECTRA

Multivariate spectral analysis provides a method by which correlation information existing between several time series can be uncovered and evaluated. For seismic data, the shape and amplitude of the spectrum of each seismogram are themselves useful information, in particular when the form of the spectrum is predictable. In the bands where the various spectra are strongly correlated, multivariate spectral analysis can be applied to deduce the relative phase and group relationships. The success of such spectral analyses in this respect has been demonstrated by the use of the maximum-likelihood method in wavenumber analysis of array data.¹

Conventional methods for estimating cross spectral density are based on generalizations of the Blackman and Tukey² and the periodogram³ techniques to multidimensional data sequences. In the Blackman and Tukey approach, the matrical autocorrelation function is estimated directly from the data. This function is scaled by a taper to window out the larger lags that are inaccurate due to finite sample size. The resulting matrix sequence is Fourier transformed to produce the matrical spectral sequence. Similarly, in the periodogram approach, window functions are employed to smooth out the effect of finite sample size.

These approaches as applied to single-channel data have shortcomings that do not disappear in their multivariate extensions. Specifically, the effect of windowing is to smooth the power spectrum and so reduce the resolution. Recently, new spectral estimation techniques that do not make assumptions about the data outside the observation interval have been shown to be superior in terms of resolution on single-channel data.⁴⁻⁷ The basic method, introduced to geophysics by Burg,⁸ is based on maximizing the information entropy of a time series, and so is referred to as the Maximum Entropy Method (MEM). Equivalently, the technique can be thought of as fitting an autoregressive model to the time series,⁹ and is referred to as autoregressive spectral analysis in the engineering literature.

There are essentially two algorithms for computing the autoregressive coefficients. The first is by onestep forward prediction error. The second, developed by Burg,¹⁰ combines forward and backward prediction to insure positive definite autocorrelation functions. In this report, we investigate the extension of the single-channel Burg technique to multichannel data.

Various aspects of the Multivariate Burg Spectral Estimator were investigated. Specifically, the accuracy and resolution of estimated spectra, the determination of optimal autoregressive order, and the effect of additive white noise on the correctness of an autoregressive model were evaluated. Although theoretical study of the properties of an autoregressive spectral estimator has been attempted,¹¹ a complete and satisfactory theory has not been developed. The investigation undertaken here was empirical. Owing to the large variety of data encountered in geophysics, no statement based on empirical investigation can be conclusive. However, studies based on idealized data types can be very beneficial. Other than illuminating various characteristics of the Multivariate Burg Estimator under a well-controlled and adjustable experimental environment, these studies provide insights in understanding more complicated spectra.

In general, a spectrum can be decomposed into broadband and narrowband components. Although the boundary between these is not well-defined, the flat spectrum for a white process and the line spectrum for multiple sinusoids have been tested to examine the extreme forms. The algorithm for computing the Burg Maximum Entropy Spectra was taken from Nuttall.¹²

First, two-channel 100-point broadband series contaminated with 1-percent white noise and with a constant time shift between the channels were analyzed for cross-spectral amplitude coherence and phase. Model orders equal to the delay were used, and the time shift was kept small compared with the data length. It was observed that, in general, the maximum and minimum cross powers were within 3 dB of the true value. Values of the estimated coherence at all frequencies were well above 0.97, with maxima close to 0.99, which is the true coherence for a signal-to-noise ratio (SNR) of 100. Phase estimates were strikingly linear, varying by less than 3 percent of the true value over the entire spectrum.

As for accuracy, the superiority of this method over the windowing method is illustrated in Figs. IV-1 and IV-2 where coherence and phase estimated by Burg's method are compared with those computed by taking the Fourier transform of a windowed estimate of the crosscorrelation sequence. Two coherence and phase spectra are shown, one with a 6-sample Bartlett window, and the other with a 100-sample Bartlett window. Even the 100-sample Bartlett estimates cannot reach the same accuracy achieved by the Burg estimates.

The same procedure was also applied on data composed of two sinusoids with constant time shifts between channels and small amounts of white noise. The cross-spectral amplitudes showed the two spectral peaks to be well-resolved, although the peak values varied by up to 3 dB from the true power levels. They were, however, consistent when the area under each spectral peak was considered. Coherences at the frequencies of the sinusoids were practically equal to one. However, they were not as well-resolved as the cross amplitude. Phases at the frequencies were within 5 percent of the true value, an error that is within one sampling interval and so quite acceptable. As was previously done for broadband noise, the accuracy of the Burg method is compared with windowing methods in Figs. IV-3 and IV-4 for an input series of 10 cycles of a single sinusoid and a 0.6π shifted version in the second channel. The Burg estimate of order 4 is clearly more accurate in both cross amplitude and phase than the Bartlett estimators.

Our next effort involved model-order determination for multichannel data. The Final Prediction Error,¹³ the Information Theoretic,¹⁴ and the Autoregressive Transfer Function⁹ criteria were used with the following result: the order numbers predicted by each method generally agree. Exceptions do occur, and in these cases use of Parzen's number⁹ produces the best spectra. For processes where the number of points that channels are shifted is greater than the order of the individual channels, the order number generated is the shift number. The result is better cross spectra than individual spectra. More complex individual channels result in orders larger than the shifts.

As an example of the effect of order number, the coherence (Fig. IV-5) and phase (Fig. IV-6) for the two shifted white processes described earlier were computed by both the Burg and windowing methods as functions of order number. Each of the order-number criteria gave the shift (i.e., 10) as the order number. Burg's estimate rapidly converged to the true spectra at and beyond the autoregressive order of 10. Phase estimates from the other method are comparable to Burg's estimates only when autocorrelation lags of 20 and longer are used. Coherence estimates, nevertheless, seen incapable of achieving the same level of accuracy as Burg's estimates, even when 50 samples of the autocorrelation sequence were used.

Our final effort looked at the effect of SNR. Figure IV-7 shows coherence and phase estimates of a two-channel shifted white signal with five levels of independent white noise added to each channel. It is obvious from the figure that the accuracy of the estimates deteriorates as uncorrelated noise power increases. The coherence estimate seems particularly sensitive to

the presence of the noise. A comparison with estimates obtained from a 100-sample Bartlett estimator indicates that, even in the presence of noise, Burg's estimator can still provide more accurate coherence and phase estimates than the conventional estimator.

A. T.-U. Ng
T. E. Landers

B. A MULTIPLE EVENT AT SEMIPALATINSK

The practical application of seismic discrimination techniques depends to a large extent on both the natural and explosion seismic history of the region in which explosions might occur. Consequently, for a given site where events of both types have occurred and their data reduced to a set of discrimination parameters (e.g., M_s - m_b , complexity, 3rd moment, etc.), a new event can be, with a great degree of certainty above some magnitude threshold, classified. In the instance where a testing region is aseismic and new events are found to have the same parameters as previous events, then, through the somewhat more subtle implication that earthquakes would have sufficiently different discrimination parameters, they too could be classified. In any case, when the depth of an event can be established at greater than the maximum feasible testing depth then the event would necessarily be an earthquake, irrespective of the seismic history of the epicentral region. However, it is possible to mimic the depth phase by multiple explosions such that casual observations of teleseismic data would classify the events as a single earthquake.¹⁵ Event-location techniques, including master-event-location methods, would be very difficult to use to establish depth since time picks on later phases would have errors due to masking by the coda of the earlier events. Consequently, depth determination for unusually complex events in aseismic regions would depend on analyzing waveform data. On the other hand, no region of the globe can be truly aseismic, i.e., said not to be capable of having an earthquake. In fact, from a geologic point of view, the earth's crust is essentially faulted everywhere. The source structure and stress environment and path characteristics determine many of the teleseismic properties (e.g., Novaya Zemlya events are more complex than Semipalatinsk events, Semipalatinsk events are much higher frequency at NORSAR than in North America, and NTS events often release considerable shear strain energy) such that the prediction of earthquake parameters for current aseismic regions is very difficult. The result of these considerations is that, under the circumstance of an event taking place in a previously aseismic region, the possibility of multiple explosions can not be ruled out on the basis that its discrimination parameters do not match a previously determined set. In light of the above discussion we present data on one such puzzling event(s) that occurred 20 March 1976 at Semipalatinsk, USSR at 50°N 77.3°E at approximately 4:03:39 GMT at 0-km G depth.¹⁶

Figure IV-8 shows the SP vertical seismograms for the event at stations with the best focal sphere distribution that can be obtained in the data base available to us. The data from College (COL) were digitized from the WWSSN 70-mm-film chip, those from Yellowknife (YKC) and Guaribidanur (GBA) are single-channel raw data recorded on analog tape and then run through an A-D converter, and the NORSAR data are the single-channel 04C site digital recording. The event is clearly quite unusual. To our knowledge, no natural seismic event near this magnitude has occurred within several hundred kilometers of the epicenter. Yet, what appears to be P, pP at about 7 sec and 1 sP at about 10 sec indicates its hypocenter to be at a depth of about 30 km, and so it would be an earthquake. It is unusual, though perhaps possible, that in every quadrant of the lower focal sphere the depth phases are larger than the initial arrival. That such behavior

can be mimicked by a set of explosions is illustrated in Fig. IV-9. A fuller explanation of the figure is given by Landers in Ref. 15; however, it suffices here to say that the bottom trace is the sum of the 5 upper identical traces (except for a delay and positive scaling factor), the basic seismogram being a LASA recording of a Semipalatinsk explosion. Not only is there an appearance of depth phases (at an earthquake-only depth), but pP is inverted. Figure IV-10 shows the surface wave that would be recorded at a distance of 12° with the same scaling and delays as in Fig. IV-9. Characteristically, signal busting at the higher frequencies produces a sum that has the overall summed amplitudes at longer periods, but reduced amplitudes at shorter periods. The overall effect is a more spread-out surface-wave train and a larger M_s . Since the m_b would still be obtained from the first arrival, the $M_s - m_b$ for the multiple set would be pushed toward earthquake-like values. Figure IV-11 shows the LP data for the 20 March 1976 event(s) and a 4 July 1976 event with the same epicenter at the MAIO SRO. The 20 March event shows the same property as the summed surface wave in Fig. IV-10, while the more compact Rayleigh wave typical of a single explosion is exhibited by the 4 July event. The Love-to-Rayleigh-wave ratio in the 20 March event is about 3:2, whereas for the 4 July event it is about 1:2. Though more an indicator of tectonic conditions at the epicenter, the variation in this ratio indicates that if it was a set of explosions, an extremely large amount of SH motion was generated.

TABLE IV-1 STATION M_s VALUES FOR 20 MARCH 1976 EVENT			
Station	A (μ)	T (sec)	M_s
MAIO	0.88	19	4.17
KON	0.67	18	4.30
SHI	0.67	21	4.24
TAB	0.33	20	3.86
QUE	0.5	22	4.02
KBL	1.08	19	4.17
			Mean $M_s = 4.13$
			S.D. = 0.16

Table IV-1 shows data used to compute an M_s value for the 20 March 1976 event. The value was determined using the formula given in Marshall and Basham.¹⁷ In Fig. IV-12, the resulting $M_s - m_b$ value (point A) is superimposed on Marshall and Basham's data events in the same epicentral region. Assuming 4 multiple events (for reasons we will show when the cepstra for this event are discussed), each contributing equally to the surface waves, the $M_s - m_b$ typical of the individual events would be at point B. As noted in Fig. IV-8, the secondary arrivals were bigger than the primary. Assuming an average amplitude per arrival to be 1.5, the amplitude of the first arrival (the "average" $M_s - m_b$ per event) would fall at point C, squarely on the explosion trend line.

As mentioned above, 4 events were assumed to be contributing to the surface waves. Evidence for this minimum number comes from cepstral analysis of the first few seconds of the SP records. We note that this part of the seismogram in each of the records shown in Fig. IV-8 is more complicated than is usually observed for events from this region. Figure IV-13 shows the first 4 sec of the Yellowknife seismogram, and Fig. IV-14 shows the cepstrum computed by analyzing the log spectrum with maximum-entropy (ME) spectral analysis¹⁸ and by direct FFT of the log spectrum. The interpretation of this function is that 2 events, the second slightly larger than the first and delayed by 0.9 sec, are present and that depth phases for both are about 0.8 sec. Such a depth-phase time delay indicates that the events originate at less than a few kilometers hypocentral depth. Counting these two, and assuming that the later arrivals are each a separate event, makes at least four and leads to the interpretation that the individual events have explosion-like M_s - m_b signal characteristics, and depth.

In summary, the SP data indicate that more than 2 events occurred. LP data indicate that the events have more explosion-like M_s - m_b values than the nearest earthquakes. The possibility exists that a combination of explosions and high-stress drop earthquakes occurred or that a series of extremely high-stress drop very shallow earthquakes occurred, but these seem unlikely.

T. E. Landers
M. W. Shields

C. SPLITTING OF THE pP PHASE FROM SUBOCEANIC EVENTS

The intent of this project was to observe a splitting of the depth phase (pP) from suboceanic events. Splitting might be expected since energy from the pP wave incident on the ocean floor should be partially reflected and partially transmitted. The part entering the water column would be reflected at the surface, and would return to the ocean floor with a delay equal to the two-way travel time in the water column. This energy would again be partly reflected and partly transmitted at the ocean floor, the transmitted part giving rise to the presumed splitting of the pP phase.

Theoretically, energy would be trapped in the water column by the strongly reflecting interfaces at the ocean surface and floor. This situation would produce a periodic repetition of the pP phase. The period would be the two-way travel time in the water column, and the amplitudes of the "multiples" would be expected to decay geometrically. Removal of these reverberations is necessary for determining the position of deep reflectors under the ocean floor. Additionally, the characteristics of the reverberations provide information on the nature of the ocean floor.

In searching for an event which might be expected to exhibit reverberations, there are a number of criteria which the event should meet to facilitate observation of the water-column phases. First, the pP wave should emerge in a region under water. This is not exactly a facile observation, since the point of emergence may be a considerable distance from the epicenter for a very deep event. Second, the event should have an uncomplicated source mechanism (an explosion would be ideal), so that there would be little question whether observed features of the seismogram are due to the source or to reflecting structures in the medium of propagation. Third, it is desirable that the epicenter be located in a region where the depth of water is constant for hundreds of kilometers in all directions, so that the two-way travel time can be accurately computed even if the epicenter or point of pP emergence is uncertain. This condition can be relaxed for shallow focus events. Fourth, events with abnormally complicated pP phases (relative to simpler P phases) may be of interest. Finally, the event should be in deep water

to facilitate observation of the reverberant phases – the deeper the better, since the reverberations will be more widely separated.

The event which best met these conditions was a shallow event (49 km) in the Kurile Island arc (15 July 1973, 14:06:50.1, $43.1^{\circ}\text{N} \times 146.52^{\circ}\text{E}$, $m_b = 5.4$). A seismogram for this event from a single station at LASA is shown in Fig. IV-15. Following the pP phase, this seismogram has a complicated structure. This is probably due, in part, to arrival of the sP, PcP, pPcP, and sPcP phases. An interesting feature of this seismogram is the pP arrival itself. Note that the P wave has a very large positive-amplitude spike. Presumably, then, the pP wave should have a very large negative-amplitude spike. This pP appears to have two such spikes separated by about 1.9 sec. Obviously, some technique more sophisticated than visual inspection must be employed to determine if the first part of the pP arrival is actually two slightly separated arrivals.

Many techniques for the detection of multiples could be applied to this problem. Those discussed here by no means exhaust the possibilities. The two techniques tried as part of this project fall into the class of cepstral analysis methods. Both involve computation of the cepstrum of pertinent parts of the seismogram and search for peaks in the cepstrum. Since details of the theory and computation^{19,20} of the cepstrum are amply covered elsewhere, they are omitted here. However, it is worthwhile to recall a few properties of the cepstrum that are important to the present efforts at interpretation.

The computation of the cepstrum is not a trivial task, due to the fact that the logarithm of the spectrum is a multivalued function. Since computer arctangent routines will return only the principal value of the phase, the principal value must be "unwrapped" to produce an analytic function. A particularly effective algorithm for performing this unwrapping operation has been developed by Tribolet.²⁰

The important feature of the cepstrum, so far as multiple detection is concerned, is that the cepstrum of a signal with multiples exhibits peaks located at the delay times of the multiples. If a primary arrival is larger than the secondary, then the cepstrum will be a causal spike train. If, instead, the reverse is true then the cepstral spike train would be anti-causal. The situation is much more complicated if there are multiple arrivals with different arrival times. This will complicate the determination of arrival times, although the peaks at the individual arrival times should be the largest.

Computation of the cepstrum is equivalent to spectral analysis of the log spectrum of the signal. One way of performing spectral analysis, as mentioned above, would be to compute the Fourier transform of the log spectrum directly. Harmonics of the log spectrum should be well-resolved in the cepstrum, provided that the available bandwidth of the signal spectrum is large compared with the periods of the harmonics. Of course, the narrower the available spectral bandwidth, the worse the resolution will be.

In particular, for a multiple with small delay time n_0 , only a few periods of the fundamental $e^{-j\omega n_0}$ will be present in the log spectrum. The peak due to this fundamental may not be well-resolved in the cepstrum. To obtain a better estimate of the location (or existence) of such a peak, it may be necessary to use one of the high-resolution spectral-estimation techniques. The MEM has been used in this manner by Landers²¹ to determine the (necessarily short) delay times of the pP phases from underground nuclear explosions. The MEM essentially fits a rational (denominator only) model to the power spectrum of a signal. Since harmonics present in a

signal contribute poles to the z -transform of the signal, the MEM tends to resolve these harmonics well. It is known to provide good resolution when only a few cycles of a harmonic are present in the data. The MEM algorithm applied to the log spectrum of a signal generates a rational approximation to the squared magnitude of the cepstrum.

Even the best-quality digital seismic data are rather poor for the detection of closely spaced arrivals, because the data are very narrowband. For LASA SP data, the available bandwidth is approximately 2 Hz, even though sampling is at 20 Hz. A multiple arriving with a delay of 2 sec would produce a harmonic in the spectrum with only 4 cycles in the available spectrum. This is the reason that high-resolution spectral estimation must be employed to estimate the delay.

The processing of the Kurile Island event is summarized in Figs. IV-16 through IV-20. Cepstra computed directly using Fourier transforms are shown in Figs. IV-16 and IV-17. Some filtering of the log spectrum was performed to remove the low-time portion of the cepstrum. It is probably dominated by the source mechanism of the earthquake. Some of the high-time part of the cepstrum was removed also. Less was removed in the second example (Fig. IV-17) than in the first. In the computation of the cepstra, only the log magnitude of the spectrum was used. This accounts for the fact that the cepstra are even. The cepstra are also rather noisy, which may be due in part to the fact that the data were not modulated to close the gap around zero frequency.

Both cepstra are dominated by large negative spikes at 10.7 sec, which are undoubtedly due to the pP arrival. There are also negative spikes around 12.4 and 12.6 sec; these are consistent with the first water reverberation phase. In Fig. IV-17, the spike at 34 sec may be due to PcP.

Figures IV-18 through IV-20 show the steps in the computation of MEM cepstra. The log magnitude and phase of the spectrum are highpass filtered to remove source-mechanism effects. Then the log spectrum is windowed to retain the portion with significant energy and discard the remainder. Any linear trend is removed from the windowed portion before an MEM estimate of the cepstrum is computed. Rational approximations of orders 60 and 99 are presented in Figs. IV-18 and IV-19, respectively. In Fig. IV-20, the seismogram is windowed to isolate the pP arrival and its coda, and the cepstral estimate is computed for pP and its coda.

From the Herrin tables, this event should have a PcP arrival at 23 sec. sP should arrive around 5 sec after pP, pPcP should be 34 sec after P, and sPcP should be 38 sec after P. In Fig. IV-18, there is an arrival at 12.5 sec; this may be an amalgam of pP, sP, and the water phase. The spike at 23 sec is probably PcP. The spike at 5 sec corresponds to pP-sP.

Figure IV-19 has small peaks at 34 and 38 sec; these could be due to pPcP and sPcP. The spike at 12 sec is probably pP. The large spike at 5 sec is again consistent with pP-sP.

Figure IV-20 has a pulse at -2 sec; this could be the water phase. The peak at 4 sec is probably sP-pP, in which case the arrival at 8 sec would be the second harmonic. Its amplitude is correct for this. The peaks at larger times are in the PcP regions.

The case for the water reverberation phase seems to be inconclusive, although some of the other arrivals may contribute peaks to the cepstra. If it is present, then it most probably is delayed by about 2 sec with respect to pP as is suggested by the raw seismogram. The epicenter for this event is located under 1000 to 2000 m of water, and a two-way travel time of 2 sec translates into a depth of 1500 m. That delay is, at least, consistent.

Since the P and pP waves are well-separated in this event, it would be worthwhile to try to design a Wiener spiking filter using the P wave and then to apply it to the pP wave and coda. One further experiment that might be tried would be to subtract the cepstrum of the P wave from

the cepstrum of the pP wave and coda. In theory, that should eliminate the source-function effects and leave just the reflector information in the pP cepstrum. Certainly, more examples and a wider variety of techniques should be used to establish the existence or nonexistence of water phases.

D. B. Harris†
T. E. Landers

D. POLARIZATION FILTERING OF LONG-PERIOD SRO DATA

As part of an evaluation of SRO data, we are investigating a wide dynamic range of body and surface waves recorded at Mashad (MAIO) from an aftershock sequence in the Kuriles. These data are described with examples in Sec. III of this SATS.

One promising type of analysis is polarization filtering which has previously been applied to SP data.^{22,23} In the SRO network it is important to take advantage of the 3-component, LP data at each station to enhance body- and surface-wave arrivals. Polarization filtering is particularly useful for this because it allows one to calculate azimuth and ellipticity of detected surface-wave trains, and the azimuth and dip angle of enhanced body phases. Thus, polarization filtering of 3-component data at a single station can reveal some of the seismic parameters usually obtained by array analysis.

Polarization filtering in the time domain is based on the geometry of the least-squares particle-motion ellipsoid shown in Fig. IV-21, calculated from a window of 3-component data. The direction and squared length of each axis are given by an eigenvector and the corresponding eigenvalue of the 3×3 covariance matrix $R = \{r_{ij}\}$ where

$$r_{ij} = \frac{1}{n-1} \left\{ \sum_{t=1}^n x_i(t) x_j(t) - \frac{1}{n} \left[\sum_{t=1}^n x_i(t) \right] \left[\sum_{t=1}^n x_j(t) \right] \right\} \quad (IV-1)$$

In this equation, n is the number of points in the window; and $x_1(t)$, $x_2(t)$, and $x_3(t)$ are, respectively, the seismogram components Z, R, and T shown in Fig. IV-21. As the window slides in time through the data, the direction and magnitude of the largest axis ℓ_1 , called the principal component of the data, constantly change. If $\ell_1 \gg \ell_2$ at a given time, then the data are strongly polarized along the ℓ_1 direction. Examples of linearly polarized phases are P, S, and Love waves.

A standard method^{22,23} of enhancing strongly polarized data is to multiply the data components at the center of the window by a gain factor

$$g = (1 - \ell_1/\ell_2) \quad , \quad 0 \leq g \leq 1 \quad (IV-2)$$

and then project the principal-component vector onto these scaled data components. This method clearly enhances strong body waves, but in many cases it also enhances noise and surface waves which have ellipticities significantly larger or smaller than 1, and which are uncorrelated on 2 or more components.

Figure IV-22 shows an example of LP, 3-component data for an earthquake in the Kurile Island sequence recorded at MAIO. The earthquake had m_b 5.4, origin time 8:07:10 on 22 January 1976, with a distance $\Delta = 66^\circ$ from MAIO. The first three traces are the unfiltered Z, R, and T components, and the next three traces are bandpass-filtered data components (11.11 to 33.33 sec) using a phase-free operator.

† Department of Electrical Engineering, M.I.T.

The 3-component data were filtered to pass linearly polarized phases using a sliding window 30 sec wide. The results are shown in traces 8, 9, and 10. Trace 7 shows the filter gain g given by Eq. (IV-2) as a function of time. As the window moves by the P, S, and SS phases the gain approaches 1.0 and the principal component is passed and projected onto the Z, R, and T axes. Later in time one can see the enhancement of Love waves on the T component and a reduction of the Rayleigh-wave amplitude by the polarization filtering. The Rayleigh waves are attenuated because ℓ_1 and ℓ_2 are nearly equal so that gain g is close to zero. However the SS wave train which contains body phase and leaky-mode surface waves²⁴ is passed because the R component is much larger than the Z component, causing g to be close to 1.

An interesting problem is that of enhancing elliptically polarized surface waves while rejecting body-wave motion. This is not possible using only the particle-motion ellipsoid. One new modification of the time-domain polarization scheme appears to be useful for this problem. This is to reduce the components to Z and R only, Hilbert transform the R components, and use the correlation coefficient between components as a gain factor. For P and Rayleigh waves, we expect particle-motion diagrams similar to those displayed in Fig. IV-23(a-b). The P wave is linearly polarized, but the Rayleigh wave is elliptically polarized with an ellipticity which strongly depends on its propagation mode and the crustal structure of the travel path. Therefore, no simple relation between ℓ_1 and ℓ_2 exists which is useful for enhancing surface waves. However, for flat-layered isotropic crustal models, the R and Z components are 90° out of phase for all frequencies.²⁵ If the R component is Hilbert transformed, it should be in phase with the Z component over the whole dispersed wave, and the resulting particle motion will then be linearly polarized with $\ell_1 \gg \ell_2$. Conversely, body phases which were in phase should be 90° out of phase and appear to be elliptically polarized.

This is illustrated in Fig. IV-24 using the Z and R components of Fig. IV-22. Trace 4 is the R component of trace 2 after Hilbert transformation. Traces 3 and 4 show P and S phases which are 90° out of phase, surface-wave components in SS which are 180° out of phase, and Rayleigh phases which are in phase.

Traces 6 and 7 in Fig. IV-24 show the results of polarization filtering traces 3 and 4 using the ellipticity gain g in Eq. (IV-2) to pass surface waves. The R component in trace 7 has been inverse Hilbert transformed to restore the original phase in trace 2. Traces 8 and 9 show the results of subtracting the passed surface waves in traces 6 and 7 from the original data. Although the Rayleigh waves are removed, the results for body phases are not convincing. In particular, the P phase in the Z component of trace 6 is not attenuated much, and on traces 8 and 9 the P wave has only about one-half the amplitude of the unfiltered data.

A further refinement in the polarization scheme is to replace the gain factor in Eq. (IV-2) by the correlation coefficient

$$g = |r_{12}| / \sqrt{r_{11}r_{22}} \quad (\text{IV-3})$$

where the covariance r_{ij} is given by Eq. (IV-1). This has the effect of attenuating components which may be strong but uncorrelated, such as certain types of noise or components which are 90° out of phase. Using this gain-factor polarization filtering of traces 3 and 4 to pass surface waves yields traces 11 and 12, and traces 13 and 14 show the original data with surface waves subtracted. Traces 11 and 12 show almost complete attenuation of the P phase, because of the 90° phase shift between R and Z components in traces 3 and 4. Also, the long wave train associated with the SS arrival clearly separates into surface-wave and body-phase arrivals on the two pairs of polarized components.

This combination of using the principal component of the particular motion ellipse and a gain factor given by the correlation coefficient between components appears to produce better separation of body- and surface-wave phases than is possible using only the least-squares ellipse parameters.

This technique will be applied to the problems of separating interfering phases of the Kurile sequence and lowering the detection threshold of body and surface waves.

C.W. Frasier
R.G. North

E. AN EXACT SOLUTION TO THE PROBLEM OF EXCITATION OF NORMAL MODES BY A PROPAGATING FAULT

Consideration of both spatial and temporal dimensions of a seismic source as well as the direction of rupture propagation becomes a significant factor in excitation of normal modes and surface waves when the wavelengths or frequencies of the waves become greater than about 1/10 of either the source length or the source duration.

Ben-Menahem²⁶ presented a solution to the problem of excitation of surface waves by propagating sources, valid when the distance to the receiver is large in comparison with both the wavelength and the source dimension. This assumption clearly will not be satisfied in many cases of interest in seismology. Kanamori and Anderson²⁷ circumvented this difficulty by dividing the 800-km-long fault of the 1960 Chilean earthquake into 16 segments, each represented by a point source activated with a proper time delay. Although such a procedure leads to satisfactory results within the range of wavelengths considered in their study, it is very time consuming if applied to a great many modes and stations. Clearly, an analytical solution is desirable. Even if such a solution should prove to be not economical in practice, it would allow testing the precision and limits of applicability of various approximations.

Here, we shall present an exact solution to the problem of excitation of normal modes by a fault propagating with a constant velocity along a fraction of a great circle.

Gilbert and Dziewonski,²⁸ following the theoretical development of Gilbert,²⁹ gave the equations for excitation of normal modes by an arbitrary seismic source. The displacement vector \underline{u} for a k^{th} normal mode observed at location \underline{r} is, in the time domain:

$$\underline{u}_k(\underline{r}, t) = \sum_{m=-\ell}^{\ell} \underline{s}_k^m(\underline{r}) \Psi_k^m(t) * C_k(t) \quad (\text{IV-4})$$

or in the frequency domain:

$$\hat{\underline{u}}_k(\underline{r}, \omega) = \hat{C}_k(\omega) \sum_{m=-\ell}^{\ell} \underline{s}_k^m(\underline{r}) \hat{\Psi}_k^m(\omega) \quad (\text{IV-5})$$

where ℓ is the angular order number of the mode. The advantage of this representation is that the receiver term $\underline{s}(\underline{r})$ and the source term are clearly separated; the source term remains the same if, for example, the strain tensor at \underline{r} instead of the displacement vector were to be evaluated.

The source function is:

$$\Psi_k^m(t) = \int_{V_0} dv \underline{M}(\underline{r}_0, t) : \bar{\underline{E}}_k^m(\underline{r}_0) \quad (\text{IV-6})$$

where $E_k^m(\underline{r}_0) = 1/2(\nabla s_k^m + s_k^m \nabla)$; the bar denotes a complex conjugate and $\underline{\underline{M}}(\underline{r}_0, t)$ is the moment density rate tensor.

Gilbert and Dziewonski concentrated their attention on point sources (in space):

$$\underline{\underline{M}}(\underline{r}_0, t) = \underline{\underline{M}}(t) \cdot \delta(\underline{r} - \underline{r}_0)$$

and Eq. (IV-6) simplified to

$$\Psi_k^m(t) = \underline{\underline{M}}(t) : \bar{E}_k^m(\underline{r}_0) \quad .$$

For large earthquakes with fault lengths of the order of several hundred kilometers, it is important to account for the finite dimensions of the source as well as the finite time and direction of rupture propagation. The fault length is clearly the dominant dimension for such an earthquake, and it is reasonable to approximate the volume integral Eq. (IV-6) by a line integral evaluated along the fault of a length L :

$$\Psi_k^m(t) = \frac{1}{L} \int_0^L \underline{\underline{M}}(\xi, t) : \bar{E}_k^m(\xi) d\xi \quad . \quad (IV-7)$$

We shall further assume that the equivalent source radius (depth) remains constant (r_0), and that the source line can be described by the arc of a great circle with the end points having colatitudes and longitudes (θ_0, λ_0) and (θ_1, λ_1) , respectively. For a spherically symmetric, nonrotating earth the choice of a coordinate system is arbitrary, and we may choose the one that will make evaluation of Eq. (IV-7) the most convenient. Following Backus,³⁰ we rotate the coordinate system such that θ_0 and λ_0 correspond to a colatitude of 90° and longitude of 0° in the new coordinate system, which we shall call "equatorial," and (θ_1, λ_1) are $(90^\circ, \Phi)$, where $\Phi = L/r_0$. Note that the moment rate tensor must also be represented in this new coordinate system. Thus, the line source represents now a fraction of the equator. Therefore,

$$\Psi_k^m(t) = \frac{1}{\Phi} \int_0^\Phi \underline{\underline{M}}(\varphi, t) : \bar{E}_k^m(r_0, \frac{\pi}{2}, \varphi) d\varphi \quad .$$

For a uniform slip motion with a constant propagation velocity v :

$$\underline{\underline{M}}(\varphi, t) = \underline{\underline{M}}\left(0, t - \frac{\varphi r_0}{v}\right) = \underline{\underline{M}}_0\left(t - \frac{\varphi r_0}{v}\right) \quad ;$$

also:

$$\bar{E}_k^m(r_0, \frac{\pi}{2}, \varphi) = \bar{E}_k^m(r_0, \frac{\pi}{2}) \cdot e^{-im\varphi} \quad . \quad (IV-8)$$

Thus,

$$\Psi_k^m(t) = \frac{1}{\Phi} \int_0^\Phi \underline{\underline{M}}_0\left(t - \frac{\varphi r_0}{v}\right) : \bar{E}_k^m(r_0, \frac{\pi}{2}) e^{-im\varphi} d\varphi$$

and in the frequency domain:

$$\begin{aligned} \hat{\Psi}_k^m(\omega) &= \frac{1}{\Phi} \int_0^\Phi \underline{\underline{M}}_0(\omega) : \bar{E}_k^m(r_0, \frac{\pi}{2}) \exp\{-i\varphi[(\omega r_0/v) + m]\} d\varphi \\ &= \underline{\underline{M}}_0(\omega) : \bar{E}_k^m(r_0, \frac{\pi}{2}) \frac{\sin \chi_m}{\chi_m} e^{-i\chi_m} \end{aligned} \quad (IV-9)$$

where

$$\chi_m = \frac{1}{2} \Phi \left(\frac{\omega r_0}{v} + m \right) \quad . \quad (\text{IV-10})$$

Function $\hat{\Psi}_k^m(\omega)$ of Eq. (IV-9) may now be substituted into Eq. (IV-5) and yield the desired solution to the problem.

The "directivity" term dependent on χ_m is similar in its form to that given by Ben-Menahem²⁶ for the excitation of surface waves by propagating sources. Following some elementary transformations, χ_m can be written as:

$$\chi_m = \frac{\omega L}{2C_{r_0}} \left(\frac{C_{r_0}}{v} + \frac{m}{\ell + 1/2} \right)$$

where $C_{r_0} = \omega r_0 / (\ell + 1/2)$ is the phase velocity at a radius r_0 . For shallow sources, $C_{r_0} \approx C$, the phase velocity at the surface of the earth.

Ben-Menahem's directivity term is

$$X_R = \frac{\omega L}{2C} \left(\frac{C}{v} - \cos \nu \right)$$

where ν is the angle measured at the origin of the rupture between the direction of rupture propagation and direction of the receiver.

The equivalence between $\cos \nu$ and $-m/(\ell + 1/2)$ can be established on the basis of the asymptotic properties of spherical harmonics. Dahlen³¹ has shown that for a high angular order number ℓ , a spherical harmonic $Y_\ell^m(\Theta, \varphi)$ can be associated with a directed great-circle path with a pole at (Θ, Λ) , where $\cos \Theta = m/(\ell + 1/2)$. There is a 180° difference between the angle Θ defined by Dahlen and that in our coordinate system.

For evaluation of amplitudes of singlets in the geographical coordinate system, we must perform the back-transformation to the original source coordinates. Backus³⁰ gives recurrence formulas that provide a very efficient means of computation of the elements of the rotation matrix. If one desires to obtain amplitudes of the degenerate multiplets, the equatorial coordinate system is the most efficient for such computations.

A. M. Dziewonski
B. A. Romanowicz

F. DISSIPATION OF SHEAR AND COMPRESSIONAL ENERGY IN THE MANTLE FROM NORMAL-MODE DATA

Observations of the attenuation of modes of free oscillation provide the best measure of the average anelastic properties of the earth. In an earlier SATS,³² we described a technique for stacking spectra from many stations which enabled us to measure Q for over 200 modes. We also presented a result from inversion of these data — a two-layer Q_μ model of the mantle with $Q_\mu = 120$ in the upper mantle and $Q_\mu = 240$ below 670 km depth. We remarked that this model, which must represent a lower bound for Q_μ , does indeed indicate a much lower value of Q_μ in the lower mantle than any others in the literature. For example, models "MM8" (Ref. 33) and "LMS" (Ref. 34) have $Q_\mu = 750$ in the lower mantle.

Here, we use new data to study the variation of Q in the mantle. By inversion experiments using Q observations for radial modes, LP spheroidal modes, and high- Q overtones, we

conclude that the value of Q_μ in the lower mantle is ~ 400 . We also find that a value of $\bar{Q}_{ScS} = 200$ is consistent with Q models which satisfy free oscillation data [published measurements of \bar{Q}_{ScS} range from 600 (Ref. 35) to 162 (Ref. 36)]. In what follows, we present only the major conclusions; the details will be published elsewhere.

Q measurements for 35 modes were obtained using individual LaCoste gravimeter recordings of three major earthquakes (1964 Alaska, 1970 Colombia, 1975 Solomon Islands). We used the simple method of observing the time rate of decay of a spectral peak corresponding to each different mode.³⁷

Figures IV-25 and IV-26 show the application of this method to the modes ${}_0S_0$ and ${}_0S_2$ using recordings of the 1964 Alaskan earthquake. The data consist of two time series, recorded at the rate of one sample per minute on two LaCoste gravimeters located at UCLA (designated as #4 and #7).³⁸ The series are over 18 days long and thus provide an excellent opportunity for observing high- Q , LP modes.

The mode ${}_0S_0$ is remarkable for its very high Q . Previous estimates of this value have ranged from 900 to $>25,000$. We believe that the proper value of Q is actually less than 7000. As shown in Fig. IV-25, for gravimeter #4 we obtain the value 5096 (4675 to 5600), and for gravimeter #7 we obtain 5663 (5203 to 6212).

The value of Q for ${}_0S_2$ is about 550. The singlets ${}_0S_2^{+1}$ and ${}_0S_2^{-1}$ can be resolved and their Q measured separately. The $m = 0$ singlet was not observable because of the geographic location of this station. In Fig. IV-26, the open circles are values of P_0 , the maximum power in the peak ${}_0S_2$ ($T = 3287.76$ sec). Overlapping time segments of 6-day lengths were used. The upper line shows the least-squares fit for all 9 points shown, and gives $Q = 581$ (509 to 678 within ± 1 S.D. of Q^{-1}). If only the first 7 points are used, the result is $Q = 499$ (447 to 565), and the first 4 points alone give $Q = 531$ (520 to 542).

The open triangles in Fig. IV-26 are \bar{P} values for ${}_0S_2^{+1}$. \bar{P} is the average power, found by integrating from period T_1 to T_2 or ± 3 discrete frequency points from the central peak value. The line fitted to the first 7 of these points gives $Q = 586$ (542 to 638).

The solid triangles in Fig. IV-26 are \bar{P} values from integrating across the entire multiplet (from $T_1 = 3304.34$ to $T_2 = 3130.70$, which corresponds to 33 discrete frequency points). The uncertainty in this fit represents about 10 percent of the measured value of Q of 556.

Having thus obtained Q measurements for 35 modes using individual recordings of 3 earthquakes, we performed inversion experiments to find Q models which satisfy these data. For the purposes of inversion, we added to this data set 5 modes — 3 toroidal and 2 spheroidal — whose Q values had been measured by stacking. We then had 40 modes: 21 were ${}_0S_l$ from ${}_0S_2$ to ${}_0S_{65}$; 7 radial modes ${}_0S_0$ to ${}_6S_0$; 8 high- Q spheroidal overtones; 3 toroidal modes; and 1 Stonely branch mode, ${}_1S_7$.

We employed two methods of inversion — inversion in the data space and in the parameter space. The method of Gilbert,³⁹ called "ranking and winnowing," takes into account the size of the observational errors in finding Lagrange multipliers for inversion in the data space. One of these inversion results is shown in Fig. IV-27. Model MM8 satisfies the data set of 40 modes with a relative rms residual of 0.416, and it predicts Q values higher than all those observed. The Q_μ model obtained by ranking and winnowing using these data and MM8 as a starting model has a relative rms of 0.196. Figure IV-27 shows that this model has $Q_\mu < 400$ in the lower mantle. Our inversions in the data space, which are free of prejudice regarding an initial choice of

parameterization of the model, failed to reveal any pronounced resolvable features in the lower mantle.

The parameter space inversion was performed for 2 or 3 shell models of Q in the mantle. For example, the simple model $Q_\mu = 353$ below 670 km, $Q_\mu = 110$ in the upper mantle, and $Q_K = \infty$ everywhere satisfies our data set with a relative rms of 0.203. However, this model, like all models we obtain when Q_K is assumed to be infinity, predicts Q values too high for all the radial modes. Thus, we allowed Q_K to vary in subsequent inversions. Because of the small size of this data set, we could not allow both Q_μ and Q_K to vary in more than one layer without obtaining a negative value for Q_K in the lower mantle. However, by assuming that $Q_K = \infty$ in the lower mantle, but allowing Q_K to assume a finite value in the upper mantle, we obtain a much better fit to the data. The model with $Q_\mu = 415$ in the lower mantle and 112 in the upper mantle, with $Q_K = 583$ in the upper mantle, has an rms of 0.185. This model satisfies the observations of radial modes better than models with $Q_K = \infty$, and provides indication that Q_K may be finite in the upper mantle. Further inversion studies and consideration of the resolution of the data will be needed to confirm this result.

R. V. Saylor[†]
A. M. Dziewonski

G. VELOCITY-DISPERSION KERNELS FOR FREQUENCY-DEPENDENT Q

Recently, numerous authors have drawn attention to the problem of velocity dispersion due to anelasticity. If the attenuating process has properties of a minimum phase filter, then the real and imaginary parts of the complex wavenumber $k(\omega)$ are interrelated through the Kramers-Krönig relationships:

$$\text{Re } [n(\omega) - n(0)] = \frac{2\omega^2}{\pi} P \int_0^\infty \frac{d\sigma \text{Im } n(\sigma)}{\sigma(\sigma^2 - \omega^2)} \quad (\text{IV-11a})$$

$$\text{Im } n(\omega) = -\frac{2\omega}{\pi} P \int_0^\infty \frac{d\sigma \text{Re } n(\sigma)}{\sigma^2 - \omega^2} \quad (\text{IV-11b})$$

where P denotes the Cauchy principal value; $n(\omega) = k(\omega)/(\omega/c)$, c being the nondispersive phase velocity; $\text{Im } n(\omega)$ corresponds to $1/2 Q(\omega)$ (see Ref. 40).

In inversion studies where both elastic and anelastic properties of the medium are investigated (see Sec. H below), it is important to establish the functional form of $\text{Im } n(\omega)$, in order to evaluate the integral Eq. (IV-11a). In most cases it is assumed that Q is frequency independent, at least within the seismic frequency band, and Eq. (IV-11a) then has a simple solution.^{40,41}

There is a growing body of evidence that this assumption may represent a fairly good approximation of reality.^{32,36,42} Yet, as the quality of the Q data improves, it may be necessary to consider Q that varies both with radius and frequency. We propose here a model that could be useful in the parameter space inversion studies.

Let us define $q_i \equiv Q_i^{-1}$ at a number of discrete frequencies ω_i , and let q decrease to zero, as a linear function of the logarithm of frequency, at ω_{i-1} and ω_{i+1} . Obviously, $q_1 = q_N = 0$. In this way, $q(\omega)$ is defined everywhere as a continuous function of frequency. For $\omega_i \leq \omega \leq \omega_{i+1}$, we have:

$$q(\omega) = \frac{[q_i \ln(\omega/\omega_{i+1}) - q_{i+1} \ln(\omega/\omega_i)]}{\ln(\omega_i/\omega_{i+1})}.$$

[†] Department of Geological Sciences, Harvard University, Cambridge, MA 02138.

The preceding equation could represent a basis for a linear inverse problem of retrieving $q_i(r)$ from attenuation data. The overall change in the refraction index is also linear with respect to q_i :

$$\operatorname{Re} [n(\omega) - n(0)] = \frac{1}{\pi} \sum_{i=2}^{N-1} q_i \cdot I_i(\omega) \quad . \quad (\text{IV-12})$$

Thus, $\operatorname{Re} [n(\omega) - n(0)]$ is a linear function of q_i multiplied by frequency-dependent kernels $I_i(\omega)$. These kernels are obtained by evaluation of the integrals:

$$I_i(\omega) = \omega^2 \left[\frac{1}{\ell n(\omega_i/\omega_{i-1})} \int_{\omega_{i-1}}^{\omega_i} \frac{(\ell n \sigma - \ell n \omega_{i-1}) d\sigma}{\sigma(\sigma^2 - \omega^2)} - \frac{1}{\ell n(\omega_{i+1}/\omega_i)} \int_{\omega_i}^{\omega_{i+1}} \frac{(\ell n \sigma - \ell n \omega_{i+1}) d\sigma}{\sigma(\sigma^2 - \omega^2)} \right] \quad . \quad (\text{IV-13})$$

The result of integration is:

$$I_i(\omega) = \frac{S_i - S_{i-1}}{\ell n(\omega_i/\omega_{i-1})} + \frac{S_i - S_{i+1}}{\ell n(\omega_{i+1}/\omega_i)} \quad (\text{IV-14})$$

where

$$S_j = \begin{cases} -F(x) & ; \quad x = \omega/\omega_j \quad \text{for } \omega < \omega_j \\ -\pi^2/24 & ; \quad \text{for } \omega = \omega_j \\ F(x) + \frac{1}{2} (\ell n x)^2 - \pi^2/12 & ; \quad x = \omega_j/\omega \quad \text{for } \omega > \omega_j \end{cases}$$

and

$$F(x) = \sum_{n=1}^{\infty} \left(\frac{1}{2n}\right)^2 x^{2n} \quad . \quad (\text{IV-15a})$$

The infinite sum above is rapidly converging for $x \leq 1/2$; for $1/2 \leq x < 1$, it is more economical to use the expression (due to F. Gilbert):

$$F(x) = \frac{\pi^2}{24} + \frac{1}{4} \sum_{n=1}^{\infty} \frac{n \ell n(1-x^2) - 1}{n^2} \cdot (1-x^2)^n \quad . \quad (\text{IV-15b})$$

In Fig. IV-28, a "triangular" $q(\omega)$ function is compared with an absorption-dispersion pair that leads to the same overall change in velocity: $v(\infty) - v(0)$. Functions that correspond to a change in velocity are very close to each other over the entire frequency range. Even the attenuation functions show great similarity. It appears that, for practical purposes, the triangular function $q(\omega)$ can be used as a simulator of absorption-dispersion pairs. Their advantage is that they are much more convenient in designing a desired $Q(\omega)$ function.

In Fig. IV-29, we compare four different functions $Q(\omega)$ and the relative changes in velocity associated with them; following Liu *et al.*,⁴¹ we determine

$$\delta v/v = \frac{[v(\omega) - v(2\pi)]}{v(\omega)} .$$

It is important to notice that the velocity dispersion for Q that varies with frequency can be very well matched, in a period range from 1 to 10,000 sec, by velocity dispersion for a constant Q in the seismic frequency band. Thus, there is an equivalent constant Q that gives approximately the same velocity dispersion as that computed for a $Q(\omega)$ function that varies by a factor 3 to 5 in the seismic frequency range. Kanamori and Anderson⁴³ indicate that this is an upper limit on the range of variation of Q in the seismic frequency band.

In both cases shown, this equivalent Q is only 20-percent higher than the average Q in the normal mode period range (100 to 3000 sec). We conclude that assumption of a constant Q model in inversion studies in which the attenuation data are represented by measurements of Q of normal modes should not lead to grossly erroneous results.

A. M. Dziewonski

H. FINITE-STRAIN EARTH MODEL WITH CONSIDERATION OF VELOCITY DISPERSION DUE TO ANELASTICITY

It has been pointed out in several recent studies^{44,44,45} that the effect of velocity dispersion due to attenuation within the range of periods from 1 to 3000 sec is several times greater than the errors in measurements of travel times of body waves or periods of free oscillations. In the first inversion study in which the effect of velocity dispersion was taken into account, Hart *et al.*⁴⁶ used only toroidal modes. Also, they have adopted a Q_μ model MM8 of Anderson *et al.*³³ in which Q in the lower mantle is approximately two times greater from recent estimates based on new, more accurate measurements of Q of normal modes.

This SATS contains preliminary results of an attempt at a simultaneous inversion for both elastic and anelastic parameters of the earth's structure. The data set includes 40 high-quality measurements of Q of normal modes (see Sec. F above), the free oscillation data of Gilbert and Dziewonski,²⁸ travel times for P ^{47,48} and S ^{49,50} (surface and deep focus), PKP,⁵¹ SKS,⁴⁹ PcP-P,⁵² and PKiKP-PcP.⁵³

Assuming that $q(r)$, where $q(r) \equiv Q^{-1}(r)$, is independent of frequency (see Sec. G above) and that it is our intention to derive a model valid at a 1-sec period,⁴¹ a perturbation in a period of free oscillation or a travel time of a body wave can be expressed as:

$$\frac{\delta T}{T} = \int_0^1 dr (\delta \rho R + \delta V_P P + \delta V_S S - \frac{\ell n \tau}{\pi} \delta q_\mu M - \frac{\ell n \tau}{\pi} \delta q_\kappa K) \quad (IV-16)$$

where R , P , S , M , and K are differential kernels for perturbations in density, compressional and shear velocity, q_μ and q_κ , respectively; τ designates the period of the wave under consideration ($\tau = T$ for free oscillations).

The expression for a change in attenuation of a mode or a body wave is:

$$\delta q = \int_0^1 dr (\delta q_\mu M + \delta q_\kappa K) \quad (IV-17)$$

Obviously, if the data are available for both Eqs. (IV-16) and (IV-17), the two systems can be solved simultaneously. The advantage of this procedure over solving for Eq. (IV-17) first

and then substituting $q_\mu(r)$ and $q_\kappa(r)$ into Eq. (IV-16) is the limited resolving power of the Q data and the fact that Eq. (IV-16) should impose additional constraints on q , if the data cover a rather broad band of frequencies (3-1/2 decades, in our case).

Following the results of Davies and Dziewonski,⁵⁴ we formulate the inverse problem for the elastic parameters in terms of the fourth-order finite-strain theory.⁵⁵ This is a further development of a parametric approach to the description of an earth model, first proposed by Hales *et al.*⁵⁶ and implemented by Dziewonski *et al.*,⁵⁷ who derived a family of parametric earth models (PEMs). The relevant expressions are

$$\left. \begin{aligned} \rho &= \rho_0(1 - 2\epsilon)^{3/2} \\ V_p &= [(1 - 2\epsilon)(L_1 + \epsilon L_2 + \frac{1}{2}\epsilon^2 L_3)/\rho_0]^{1/2} \\ V_s &= [(1 - 2\epsilon)(M_1 + \epsilon M_2 + \frac{1}{2}\epsilon^2 M_3)/\rho_0]^{1/2} \end{aligned} \right\} . \quad (IV-18)$$

The strain ϵ can be represented as a function of radius:

$$\epsilon(r) = \sum_{n=0}^N a_n r^{2n} . \quad (IV-19)$$

By perturbing Eqs. (IV-18) with respect to ϵ , zero pressure density ρ_0 , and parameters L and M , we express $\delta\rho$, δV_p , and δV_s in Eq. (IV-16) in terms of the parameters of the finite-strain theory. A further assumption that a perturbation in strain can be represented by

$$\delta\epsilon(r) = \sum_{n=0}^N b_n r^{2n} \quad (IV-20)$$

completes parametrization of the linearized equation (IV-16).

The finite-strain approach has been applied to three regions of the earth's interior: lower mantle, outer core, and inner core. Because of the superadiabatic gradients and lack of knowledge of the details of the upper-mantle structure, the PEM-like representation was retained for depths less than 670 km.

Table IV-2 compares the strain function and the finite-strain parameters of the model FSQMK (finite strain, Q_μ , and Q_κ) with those of a finite-strain model FS, which was constructed ignoring the effect of velocity dispersion. The density and seismic velocities in the radius range from 0 to 5701 km can be easily reconstructed by substitution of appropriate parameters into Eqs. (IV-18). The seismic parameters for the upper mantle and the crust are listed in Table IV-3. The attenuation model is presented in Table IV-4; it is quite similar, in principle, to that described by Sailor and Dziewonski in Sec. F above. For periods other than 1 sec, the velocities of model FSQMK must be corrected according to the formulas:

$$\begin{aligned} V_s(r, T) &= V_s(r, 1) \cdot [1 - Q_\mu^{-1}(r) \cdot \ln T/\pi] \\ V_p(r, T) &= V_p(r, 1) \left\{ 1 - \frac{\ln T}{\pi} \left[\frac{4}{3} \frac{v_s^2}{v_p^2} Q_\mu^{-1}(r) + \left(1 - \frac{4}{3} \frac{v_s^2}{v_p^2} \right) Q_\kappa^{-1}(r) \right] \right\} . \end{aligned} \quad (IV-21)$$

TABLE IV-2

STRAIN AS A FUNCTION OF SQUARED RADIUS, $Z = (r/a)^2$, AND FINITE-STRAIN PARAMETERS FOR TWO EARTH MODELS FSQMK (FINITE STRAIN, Q_μ , AND Q_κ) AND FS (FINITE STRAIN, NO VELOCITY DISPERSION) FOR THE INNER CORE, OUTER CORE, AND LOWER MANTLE. PARAMETERS FOR FSQMK ARE VALID AT 1-sec PERIOD.

Region and Radius Range (km)	Strain		Finite-Strain Parameters (g/cm ³ or Mb)		
	FSQMK	FS		FSQMK	FS
Inner Core (0 to 1226.6)	-0.27054 +0.37951 · Z	-0.27062 +0.38196 · Z	ρ_0	6.81054	6.82124
			L_1	2.08429	2.08069
			L_2	-12.11473	-12.15641
			L_3	6.99397	7.07030
			M_1	0.56027	0.55099
			M_2	-0.24501	-0.20576
			M_3	-1.24501	-1.42100
Outer Core (1225.5 to 3484.5)	-0.26742 +0.31067 · Z +0.15940 · Z ²	-0.26798 +0.30803 · Z +0.16041 · Z ²	ρ_0	6.51551	6.52092
			L_1	1.26970	1.22990
			L_2	-10.80603	-10.56040
			L_3	17.49536	20.68498
Lower Mantle (3484.5 to 5701.0)	-0.18517 +0.21237 · Z -0.02661 · Z ²	-0.18392 +0.21180 · Z -0.02802 · Z ²	ρ_0	3.99624	3.98614
			L_1	3.81621	3.81471
			L_2	-21.85339	-21.73004
			L_3	-61.33473	-59.40508
			M_1	1.24459	1.22405
			M_2	-5.84662	-6.02182
			M_3	-36.51793	-38.44252

TABLE IV-3						
DENSITY AND SEISMIC VELOCITIES OF THE UPPER MANTLE AND THE CRUST OF EARTH MODELS FSQMK (FINITE STRAIN, Q_μ , AND Q_κ ; VALID AT 1-sec PERIOD) AND FS (FINITE STRAIN, ATTENUATION NOT ACCOUNTED FOR)						
Radius (km)	FSQMK			FS		
	Density (g/cm ³)	V _p (km/sec)	V _s (km/sec)	Density (g/cm ³)	V _p (km/sec)	V _s (km/sec)
5701	4.077	10.034	5.499	4.076	10.009	5.459
5801	3.955	9.828	5.331	3.954	9.806	5.290
5901	3.830	9.620	5.159	3.829	9.601	5.119
5951	3.767	9.514	5.073	3.766	9.496	5.032
5951	3.522	9.198	4.908	3.549	9.022	4.818
6051	3.463	8.887	4.738	3.489	8.703	4.645
6151	3.403	8.571	4.565	3.429	8.378	4.469
6151	3.403	7.885	4.400	3.429	7.892	4.336
6291	3.316	7.885	4.400	3.343	7.892	4.336
6291	3.316	7.924	4.716	3.343	7.931	4.689
6352	3.278	7.924	4.716	3.305	7.931	4.683
6352	2.898	6.500	3.750	2.898	6.500	3.750
6357	2.898	6.500	3.750	2.898	6.500	3.750
6357	2.798	5.000	3.550	2.798	6.000	3.550
6368	2.798	6.000	3.550	2.798	6.000	3.550
6368	1.030	1.500	—	1.030	1.500	—
6371	1.030	1.500	—	1.030	1.500	—

TABLE IV-4 Q _μ AND Q _κ IN THE EARTH MODEL FSQMK. Q IS INFINITE FOR DEPTH INTERVALS OTHER THAN SPECIFIED IN THE TABLE.		
Depth Range (km)	Q _μ	Q _κ
3 to 80	450	∞
80 to 420	93	412
420 to 670	183	412
670 to 2886.5	366	∞

The differences between FSQMK and FS models are similar, in general, to those between QM1 (Ref. 46) and C2 (Ref. 58). The largest differences are in the upper mantle, particularly in the depth range from 220 to 420 km; in our model, there was also an appreciable increase in the compressional velocity in this depth range. Overall, the increase in shear velocity in the upper mantle is somewhat less than 2 percent estimated by Hart *et al.*⁴⁶ On the other hand, our increase in shear velocity in the lower mantle is roughly twice that of Hart *et al.*⁴⁶ this is clearly related to the fact that our Q_μ in this region is only one-half of that used to derive model QM1 (Ref. 46).

Model FSQMK gives only marginally worse fit to the normal-mode data than other recent earth models. The relative rms error for 1049 normal-mode data is 0.205 percent for FSQMK, 0.180 percent for FS, 0.186 percent for PEM-A (Ref. 57), and 0.182 percent for 1066B (Ref. 28). The error for FSQMK may be reduced in further iterations.

It is interesting to compare the travel times computed for the models FSQMK and FS with the observed travel-time data. In Fig. IV-30, we show the P travel times for a surface and a deep focus. The baseline predicted for the model FSQMK is practically identical to that of "1968 Tables" (Ref. 47); in addition, for a focus at 550 km depth, agreement is also reached with the data of Sengupta and Julian.⁴⁸ In Fig. IV-31, we compare S travel times; the agreement with smoothed observations of Hales and Roberts⁴⁹ is nearly perfect; it is also good for the deep-focus data of Sengupta,⁵⁰ although there is a systematic difference of slightly over 1 sec at distances greater than 75°. As this difference has the opposite sense from that obtained for the surface focus, one may suspect discrepancies between the data sets. Also, the fit could be improved by increasing the assumed period of the deep-focus S waves.

What is important is that we have found an excellent agreement between the baselines predicted from our model and those derived from the travel-time observations using land-based stations. We also satisfy within 0.4 sec the average vertical ScS travel time of Sipkin and Jordan.⁵⁹ Assuming that the travel-time baseline values are not biased, one could conclude that the differences between the harmonic average velocities under oceans and continents are rather small; this appears to agree with the conclusions of Okal and Anderson.⁶⁰

A. M. Dziewonski

I. CORRELATION OF SEISMIC ACTIVITY WITH CHANGES IN THE RATE OF ROTATION OF THE EARTH

Previous work^{61,62} suggested that seismic activity varies with time in a nonrandom fashion, since it appears to be possible to correlate these variations across many of the seismic regions of the globe. The mechanism for these changes in seismicity was not discussed in these studies, though it is clear that only global mechanisms are candidates, and from the rather limited number of possibilities the rate of rotation of the earth must be a leading contender.⁶³

Detailed analysis of earthquake time-series from many different areas indicated that the following features appear quite commonly: A small trough in seismicity during late 1964 is followed by a high during 1965, and then a period of unusually low activity extends from mid-1966 through most of 1967. Activity commonly increases during 1968, and then becomes much less coherent from the period 1969 to 1973, though there is a suggestion of an increase in activity in 1971.

Changes in the rate of rotation of the earth (i.e., in the length of the day) have been well-documented since 1955, when atomic clocks were introduced. Figure IV-32 shows the length of the day from mid-1955 to mid-1976, using data sampled at 30-day intervals, supplied to us by Dr. L. V. Morrison (Royal Greenwich Observatory, private communication). A very strong seasonal term with amplitude approximately 1 msec and containing 6- and 12-month components⁶⁴ is apparent. These seasonal terms are effectively removed by passing a sliding 12-month averaging window through the data. The resulting curve is labeled "Annual Means" in Fig. IV-32.

This mean variation in rotation rate has a great amount of structure. In particular, notice the rapid increases in the length of day (corresponding to decelerations of the earth) during 1956-57, 1963-64, and 1971. Smaller increases are clear in 1965 and 1968.

Anderson⁶³ has suggested that the large number of earthquakes in the period 1900 to 1910 may have been associated with the very rapid change in the length of day that began about 1890. It therefore seems logical to compare seismicity with the rate of change of the length of day in Fig. IV-32. Interestingly, the periods of most-rapid change all seem to be associated with high seismic activity. Figure IV-33 shows counts of large earthquakes during the period 1955 to 1976, and peaks in 1956-57 and 1971 are noticeable. There is no clear peak associated with the 1963-64 change, though this culminated in two large earthquakes - the Kurile Island (1963) and Alaska (1964) events. Figure IV-34 shows seismic-energy release during the same period, and now all three peaks emerge. However, the calculation of energy requires reliable estimates of the magnitude of large events, and this is notoriously difficult. In particular, it has been necessary to use the Duda⁶⁵ catalog for the period 1955 to 1964, and it is not clear that the listed magnitudes in this catalog are very reliable.

Comparing the rate of change of the length of day with the earthquake time series described earlier shows an interesting agreement. In particular, the change in rotation rate was small during the latter part of 1964, and was very low during the period 1966-67, as was the seismicity.

The preliminary conclusion of this study is that there seems to be sufficient correlation between changes in seismic activity and changes in the rate of rotation of the earth to warrant further investigation. It is interesting to note that the rate of rotation is decreasing during 1976, perhaps at a significantly fast rate. We also note that there have been a number of large earthquakes during 1976. This somewhat speculative correlation will be examined further as more rotation-rate data become available.

M. A. Chinnery

REFERENCES

1. J. Capon, "High-Resolution Frequency-Wavenumber Spectrum Analysis," *Proc. IEEE* 57, 1408-1418 (1969), DDC AD-696880.
2. R. B. Blackman and J. W. Tukey, The Measurement of Power Spectra from the Point of View of Communications Engineering (Dover Press, New York, 1956).
3. R. H. Jones, "A Reappraisal of the Periodogram in Spectral Analysis," *Technometrics* 7, 531-542 (1965).
4. R. T. Lacoss, "Data Adaptive Spectral Analysis Methods," *Geophysics* 36, 661-675 (1971).
5. T. J. Ulrych, "Maximum Entropy Power Spectrum of Truncated Sinusoids," *J. Geophys. Res.* 77, 1396-1400 (1972).
6. T. J. Ulrych and T. N. Bishop, "Maximum Entropy Spectral Analysis and Autoregressive Decomposition," *Rev. Geophys. Space Phys.* 13, 183-200 (1975).
7. M. Kavah and G. R. Cooper, "An Empirical Investigation of the Properties of the Autoregressive Spectral Estimator," *IEEE Trans. Inform. Theory* IT-22, 313-323 (1976).
8. J. P. Burg, "Maximum Entropy Spectral Analysis," paper presented at the 37th Annual International SEG Meeting, Oklahoma City, OK, 31 October 1967.
9. E. Parzen, "Multiple Time Series: Determining the Order of Approximating Autoregressive Schemes," Technical Report No. 23, State University of New York, Buffalo, NY (1975).
10. J. P. Burg, "Maximum Entropy Spectral Estimator," Ph. D. Dissertation, Stanford University, Stanford, CA (1975).
11. R. Kromer, "Asymptotic Properties of the Autoregressive Spectral Estimator," Ph. D. Dissertation, Stanford University, Stanford, CA (1970).
12. A. H. Nuttal, "Fortran Program for Multivariate Linear Predictive Spectral Analysis, Employing Forward and Backward Averaging," Technical Report No. 5419, Naval Underwater Systems Center, San Diego, CA (1976).
13. H. Akaike, "Autoregressive Model Fitting for Control," *Ann. Inst. Statist. Math.* 23, 163-180 (1971).
14. ———, "A New Look at the Statistical Model Identification," *IEEE Trans. Automat. Contr.* AC-19, 716-723 (1974).
15. Seismic Discrimination SATS, Lincoln Laboratory, M.I.T. (30 June 1973), DDC AD-766559/9.
16. Earthquake Data Report, U.S. Geological Survey, EDR #13-76, 31-32 (14 October 1976).
17. P. D. Marshall and P. W. Basham, "Discrimination Between Earthquakes and Underground Explosions Employing an Improved M_s Scale," *Geophys. J. R. Astron. Soc.* 28, 431-458 (1972).
18. T. E. Landers and R. T. Lacoss, "Some Geophysical Applications of Autoregressive Spectral Estimates," *IEEE Trans. Geosci. Electron.* GE-15, 26-31 (1977).
19. A. V. Oppenheim and R. W. Schaffer, Digital Signal Processing, Chap. 10 (Prentice-Hall, New York, 1975).
20. J. M. Tribolet, "A New Phase Unwrapping Algorithm," *IEEE Trans. Acoust., Speech, and Signal Processing* (in press).
21. Seismic Discrimination SATS, Lincoln Laboratory, M.I.T. (31 December 1974), pp. 11-12, DDC AD-A006194/5.
22. Ibid. (30 June 1975), DDC AD-A014793/4.

23. C.B. Archambeau, J.A. Bradford, P.W. Broome, W.C. Dean, E.A. Flinn, and R.L. Sax, "Data Processing Techniques for the Detection and Interpretation of Teleseismic Signals," *Proc. IEEE* 53, 1860-1884 (1965).
24. R. Chander, L.E. Alsop, and J. Oliver, "On the Synthesis of Shear Coupled P₁ Waves," *Bull. Seismol. Soc. Am.* 58, 1849-1877 (1968).
25. N.A. Haskell, "The Dispersion of Surface Waves on Multilayered Media," *Bull. Seismol. Soc. Am.* 43, 17-33 (1953).
26. A. Ben-Menahem, "Radiation of Seismic Surface Waves from Finite Moving Sources," *Bull. Seismol. Soc. Am.* 51, 401-433 (1961).
27. H. Kanamori and D.L. Anderson, "Amplitude of the Earth's Free Oscillations and Long Period Characteristics of the Earthquake Source," *J. Geophys. Res.* 80, 1075-1078 (1975).
28. F. Gilbert and A.M. Dziewonski, "An Application of Normal Mode Theory to the Retrieval of Structural Parameters and Source Mechanisms from Seismic Spectra," *Philos. Trans. R. Soc. Lond.* 278, 187-269 (1975).
29. F. Gilbert, "Excitation of the Normal Modes of the Earth by Earthquake Sources," *Geophys. J. R. Astron. Soc.* 22, 223-226 (1970).
30. G. Backus, "Geophysical Interpretation of Measurements of Average Phase Velocities of Surface Waves Over Great Circular and Great Semi Circular Paths," *Bull. Seismol. Soc. Am.* 54, 571-610 (1964).
31. F.A. Dahlen, "The Correction of Great Circular Surface Wave Phase Velocity Measurements for the Rotation and Ellipticity of the Earth," *J. Geophys. Res.* 80, 4895-4903 (1975).
32. Seismic Discrimination SATS, Lincoln Laboratory, M.I.T. (31 December 1975), pp. 23-25, DDC AD-A025777/4.
33. D.L. Anderson, A. Ben-Menahem, and C.B. Archambeau, "Attenuation of Seismic Energy in the Upper Mantle," *J. Geophys. Res.* 70, 1441-1448 (1965).
34. S.W. Smith, "The Anelasticity of the Mantle," *Tectonophysics* 13, 601-622 (1972).
35. R.L. Kovach and D.L. Anderson, "Attenuation of Shear Waves in the Upper and Lower Mantle," *Bull. Seismol. Soc. Am.* 54, 1855-1864 (1964).
36. T.H. Jordan and S.A. Sipkin, "Estimation of the Attenuation Operator for Multiple ScS Waves," *Geophys. Res. Lett.* (in press).
37. N.F. Ness, J.C. Harrison, and L.B. Slichter, "Observations of the Free Oscillations of the Earth," *J. Geophys. Res.* 66, 621-629 (1961).
38. L.B. Slichter, "Free Oscillations of the Earth," in *Dictionary of Geophysics*, Vol. I, S.K. Runcorn, Ed. (Pergamon Press, London, 1967), pp. 331-343.
39. F. Gilbert, "Ranking and Winnowing Gross Earth Data for Inversion and Resolution," *Geophys. J. R. Astron. Soc.* 22, 125-128 (1971).
40. W.L. Futterman, "Dispersion Body Waves," *J. Geophys. Res.* 67, 5279-5291 (1962).
41. H-P. Liu, D.L. Anderson, and H. Kanamori, "Velocity Dispersion Due to Anelasticity; Implications for Seismology and Mantle Composition," *Geophys. J. R. Astron. Soc.* 47, 41-58 (1976).
42. J.N. Brune, "Q of Shear Waves Estimated from S-SS Spectral Ratios," *Geophys. Res. Lett.* 4, 179-181 (1977).
43. H. Kanamori and D.L. Anderson, "Importance of Physical Dispersion in Surface Wave and Free Oscillation Problems: Review," *Rev. Geophys. Space Phys.* 15, 105-112 (1977).
44. S. Akopyan, V.N. Zharkov, and V.M. Lubimov, "On the Dynamic Shear Modulus of the Earth's Interior," *Dokl. Akad. Nauk SSSR* 223, No. 1 (1975), translated from Russian by R.V. Sailor.

45. M. J. Randall, "Attenuative Dispersion and Frequency Shifts of the Earth's Free Oscillations," *Phys. Earth Planet. Int.* 12, P1-P4 (1976).
46. R. S. Hart, D. L. Anderson, and H. Kanamori, "Shear Velocity and Density of an Attenuating Earth," *Earth Planet. Sci. Lett.* 32, 25-34 (1976).
47. "1968 Seismological Tables for P Phases," E. Herrin (Chairman), *Bull. Seismol. Soc. Am.* 58, 1193-1241 (1968).
48. M. Sengupta and B. R. Julian, "P-Wave Travel Times for Deep Earthquakes," *Bull. Seismol. Soc. Am.* 66, 1555-1580 (1976).
49. A. L. Hales and J. L. Roberts, "The Travel Times of S and SKS," *Bull. Seismol. Soc. Am.* 60, 461-489 (1970).
50. M. Sengupta, "The Structure of the Earth's Mantle from Body Wave Observations," Ph. D. Thesis, Massachusetts Institute of Technology (1975).
51. J. H. Whitcomb, "A Study of the Velocity Structure of the Earth by the Use of Core Phases," Part I of Ph. D. Thesis, California Institute of Technology (1973).
52. E. R. Engdahl and L. E. Johnson, "Differential PcP Travel Times and the Radius of the Core," *Geophys. J. R. Astron. Soc.* 39, 435-456 (1974).
53. E. R. Engdahl, E. A. Flinn, and R. P. Masse, "Differential PKiKP Travel Times and the Radius of the Inner Core," *Geophys. J. R. Astron. Soc.* 39, 457-464 (1974).
54. G. F. Davies and A. M. Dziewonski, "Homogeneity and Constitution of the Earth's Lower Mantle and Outer Core," *Phys. Earth Planet. Int.* 10, 336-343 (1975).
55. G. F. Davies, "Quasi-Harmonic Finite Strain Equations of State of Solids," *J. Phys. Chem. Solids* 34, 1417-1429 (1973).
56. A. L. Hales, E. R. Lapwood, and A. M. Dziewonski, "Parameterization of a Spherically Symmetric Earth Model with Special References to the Upper Mantle," *Phys. Earth Planet. Int.* 9, 9-12 (1974).
57. A. M. Dziewonski, A. L. Hales, and E. R. Lapwood, "Parametrically Simple Earth Models Consistent with Geophysical Data," *Phys. Earth Planet. Int.* 10, 12-48 (1975).
58. D. L. Anderson and R. S. Hart, "An Earth Model Based on Free Oscillations and Body Waves," *J. Geophys. Res.* 81, 1461-1475 (1976).
59. S. A. Sipkin and T. H. Jordan, "Lateral Heterogeneity of the Upper Mantle Determined from the Travel Times of Multiple ScS," *J. Geophys. Res.* 81, 6307-6320 (1976).
60. E. A. Okal and D. L. Anderson, "A Study of Lateral Inhomogeneities in the Upper Mantle by Multiple ScS Travel Time Residuals," *Geophys. Res. Lett.* 2, 313-316 (1975).
61. Seismic Discrimination SATS, Lincoln Laboratory, M.I.T. (30 June 1975), DDC AD-A014793/4.
62. M. A. Chinnery and T. E. Landers, "Evidence for Earthquake Triggering Stress," *Nature* 258, 490-493 (1975), DDC AD-A024230/5.
63. D. L. Anderson, "Earthquakes and the Rotation of the Earth," *Science* 186, 49 (1974).
64. R. A. Challinor, "Variations in the Rate of Rotation of the Earth," *Science* 172, 1022-1025 (1971).
65. S. J. Duda, "Secular Seismic Energy Release in the Circum-Pacific Belt," *Tectonophysics* 2, 409-452 (1965).

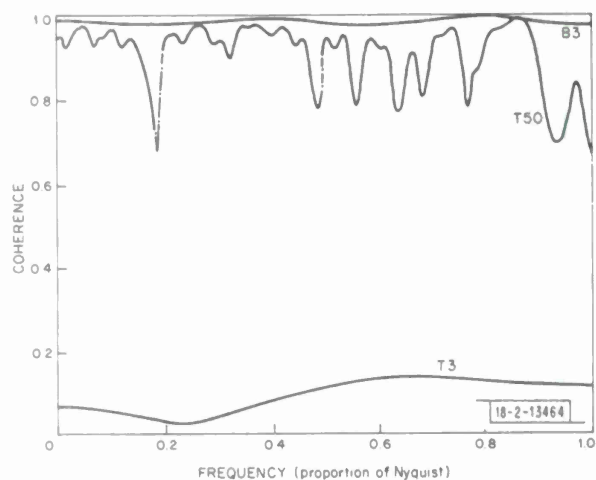


Fig. IV-1. Coherence spectra of correlated white processes. B3 is Burg Estimator of order 3; T3 is Taper and Transform Estimator of lag 3; T50 is Taper and Transform Estimator of lag 50.

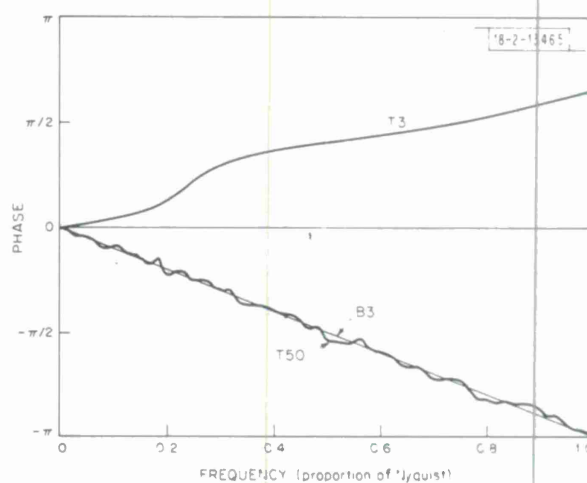


Fig. IV-2. Phase spectra of correlated white processes. B3 is Burg Estimator of order 3; T3 is Taper and Transform Estimator of lag 3; T50 is Taper and Transform Estimator of lag 50.

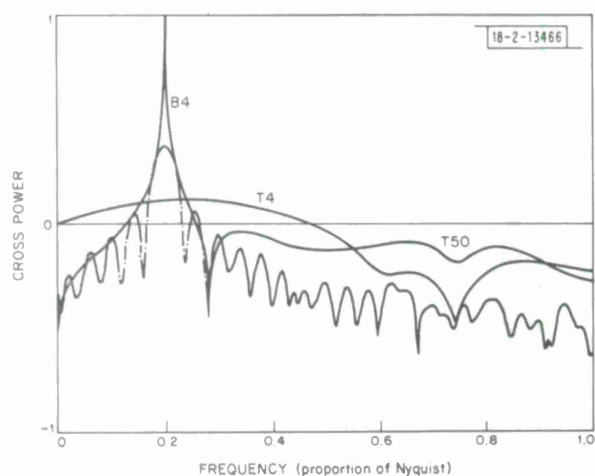


Fig. IV-3. Cross-spectral amplitudes of single sinusoid. B4 is Burg Estimator of order 4; T4 is Taper and Transform Estimator of lag 4; T50 is Taper and Transform Estimator of lag 50.

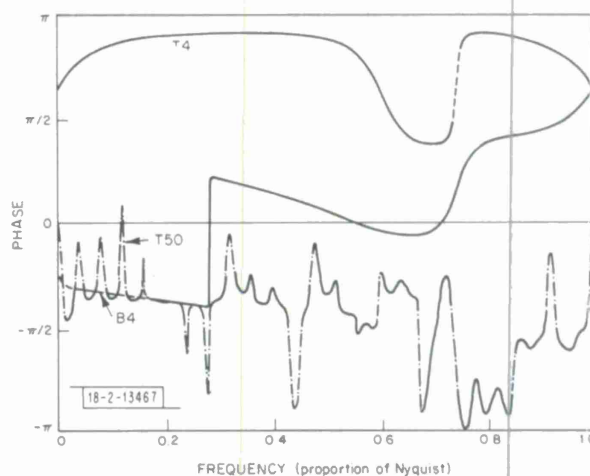


Fig. IV-4. Phase spectra of single sinusoid. B4 is Burg Estimator of order 4; T4 is Taper and Transform Estimator of lag 4; T50 is Taper and Transform Estimator of lag 50.

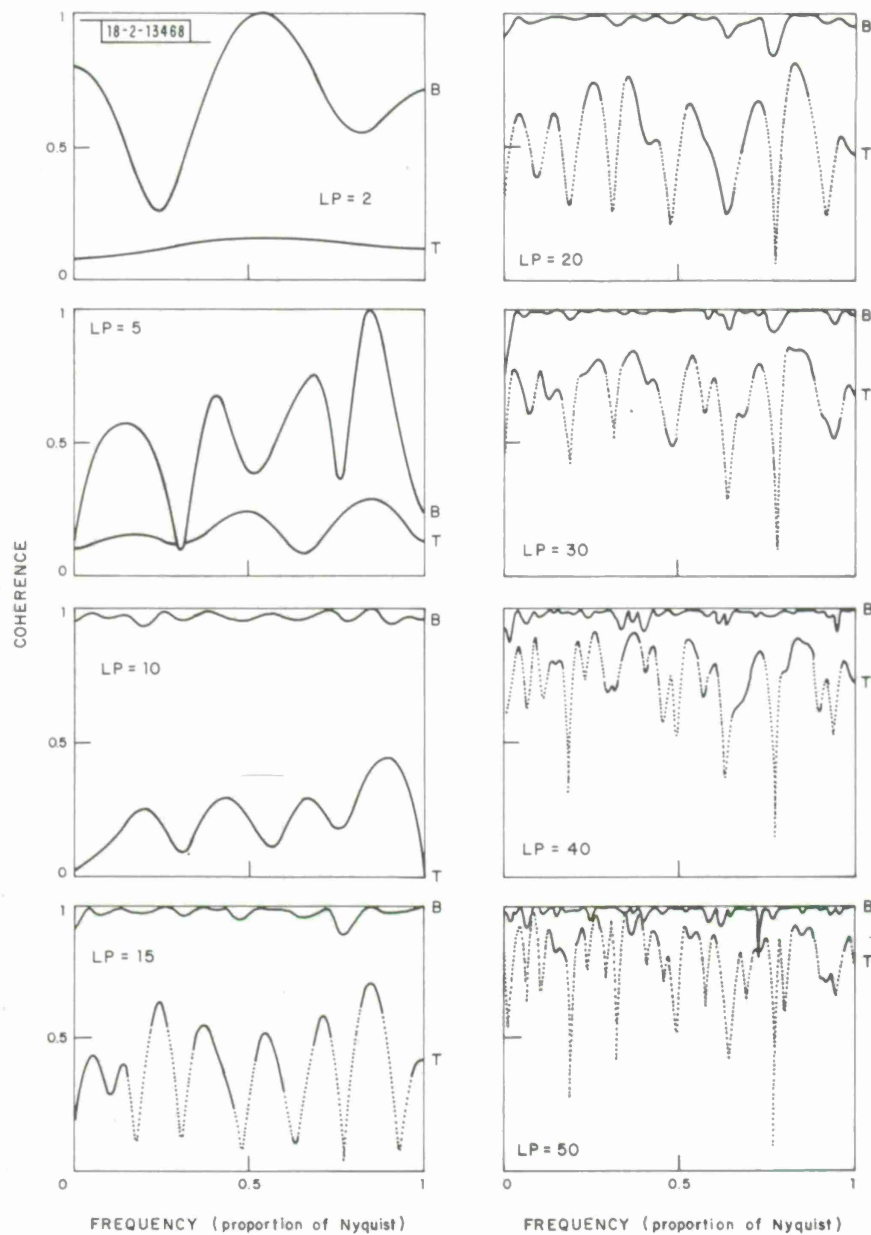


Fig. IV-5. Coherence spectra generated by autoregressive estimators of orders 2, 5, 10, 15, 20, 30, 40, 50.

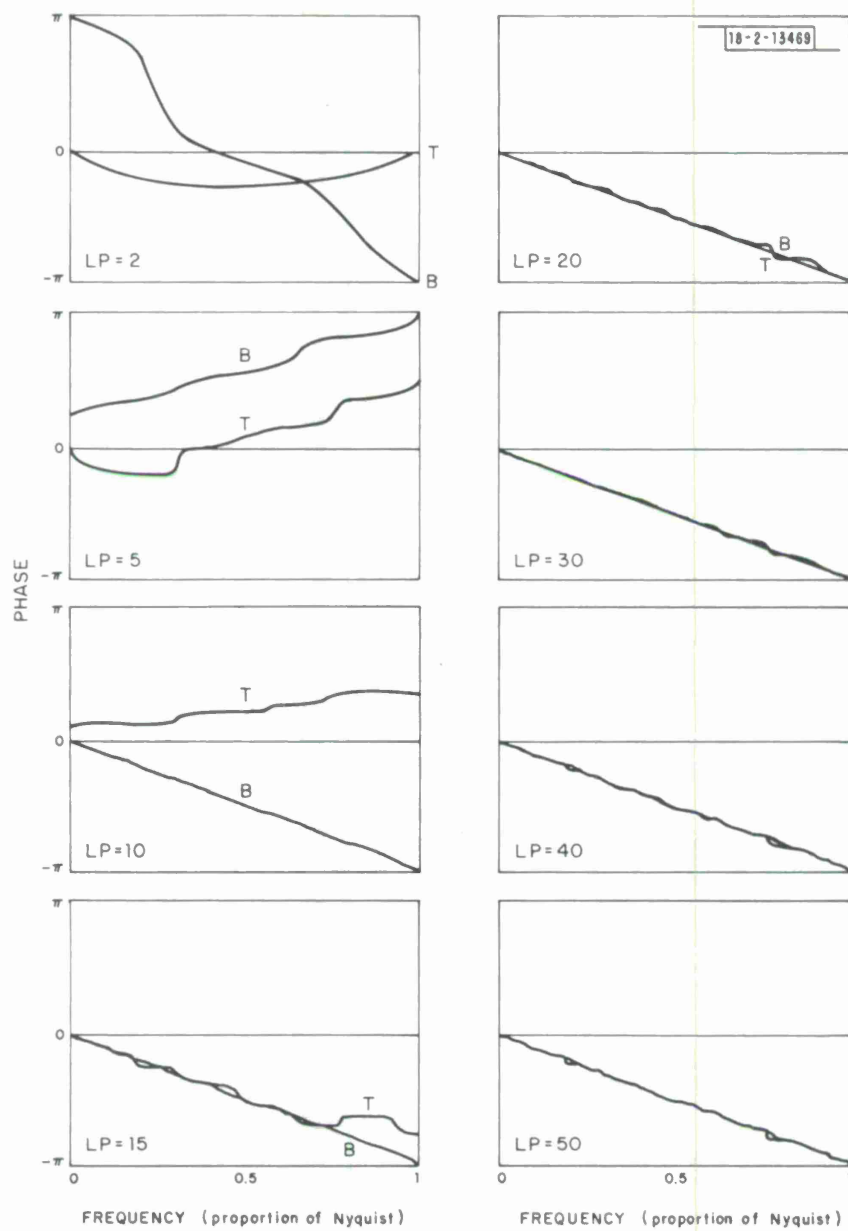


Fig. IV-6. Phase spectra generated by autoregressive estimators of orders 2, 5, 10, 15, 20, 30, 40, 50.

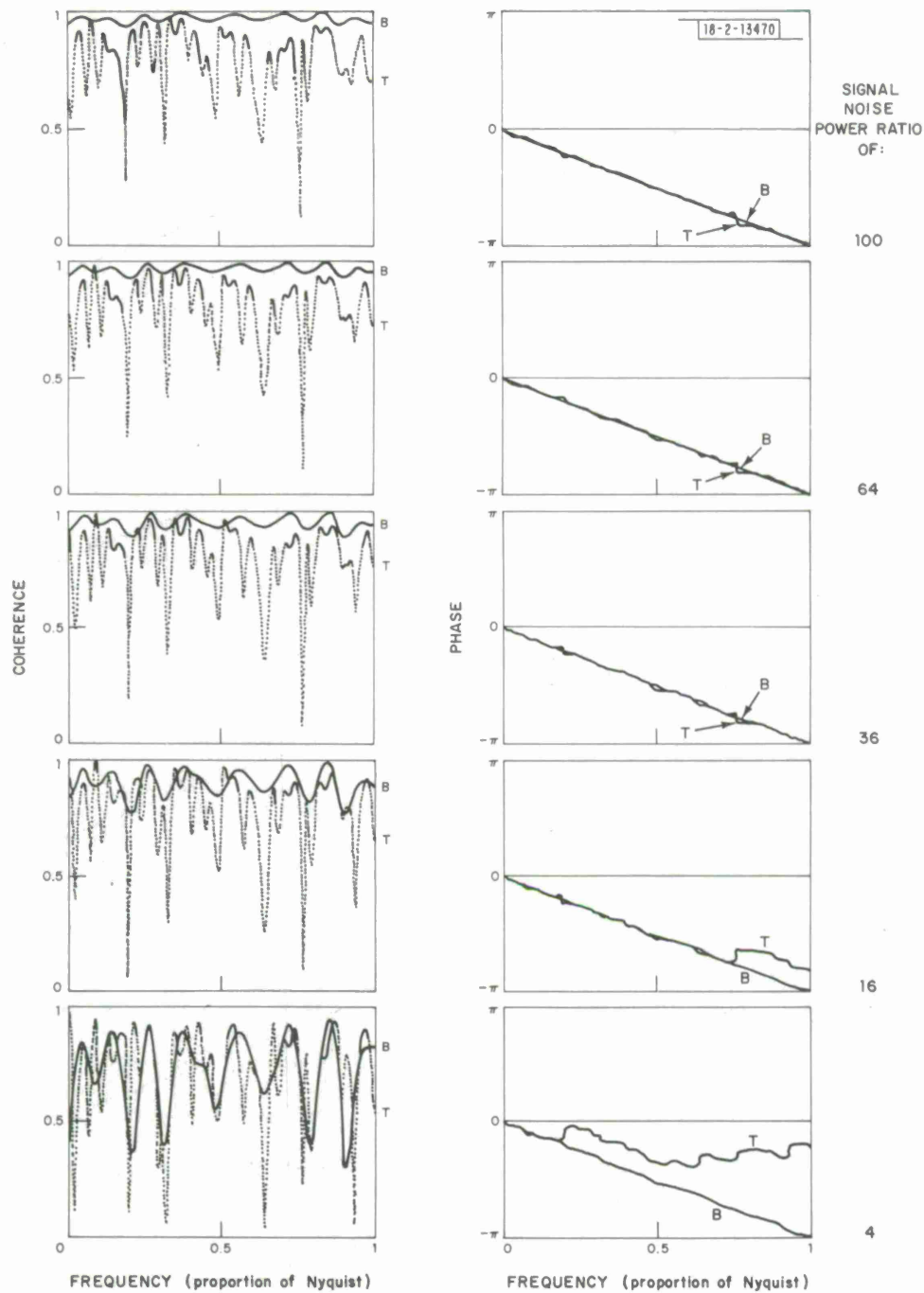


Fig. IV-7. Coherence and phase spectra for varying SNR.

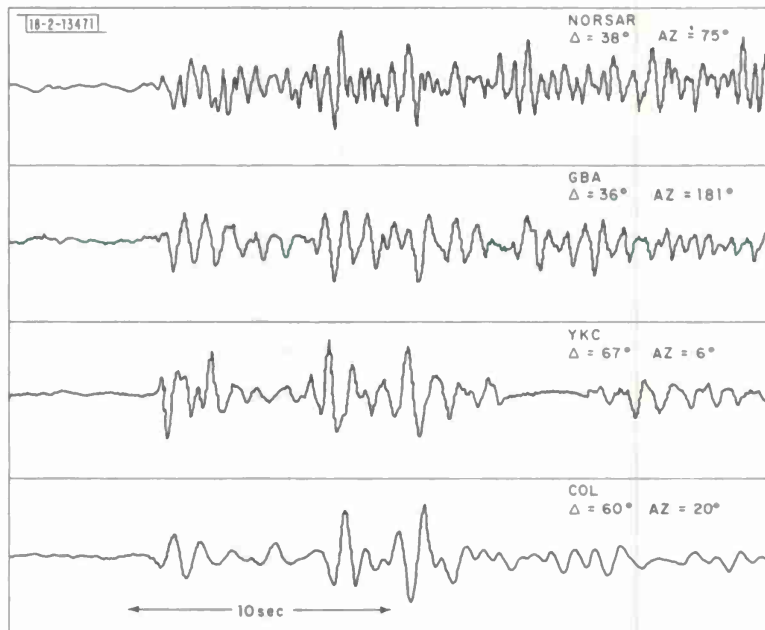


Fig. IV-8. 20 March 1976 event recorded at NOR SAR, GBA, YKC, and COL.

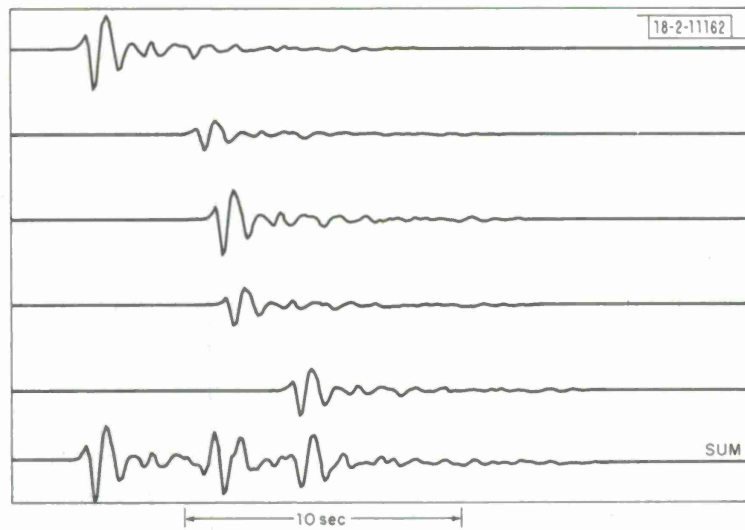


Fig. IV-9. Sum of eight identical SP waveforms to simulate pP.

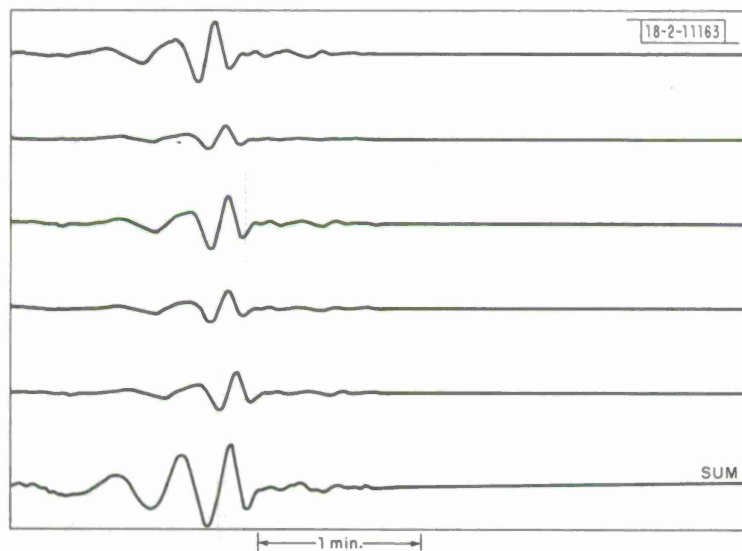


Fig. IV-10. Same as Fig. IV-9 for Rayleigh wave.

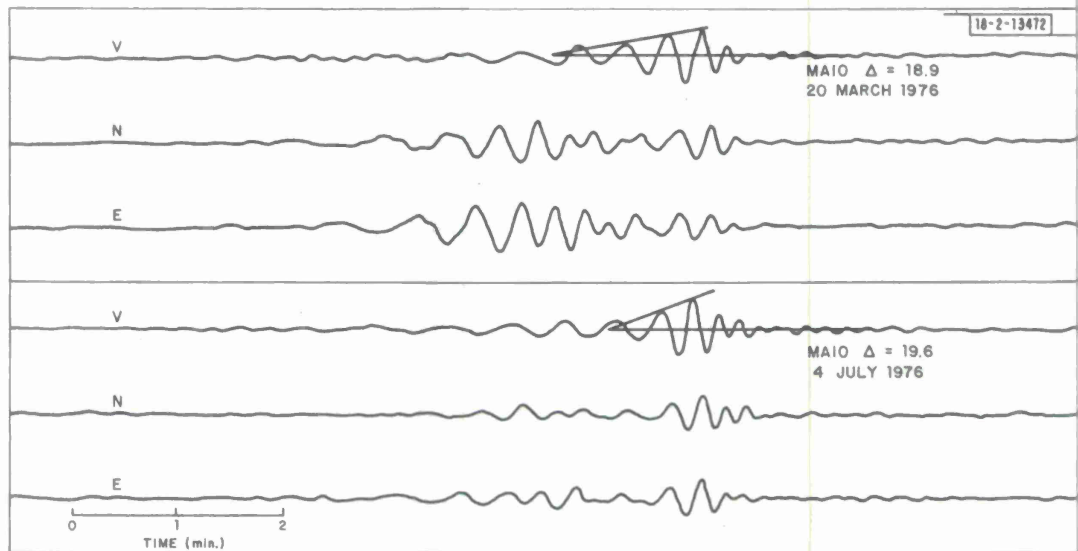
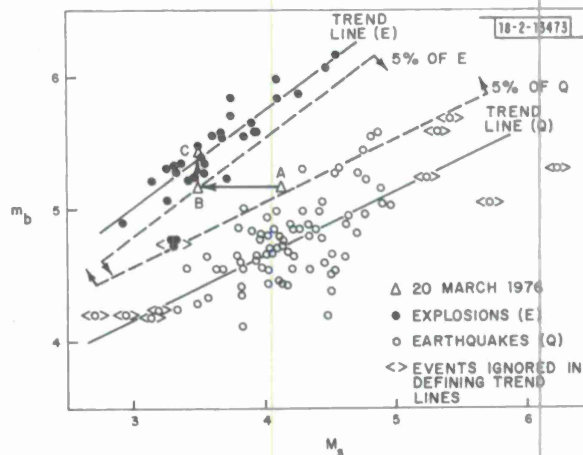


Fig. IV-11. Surface waves recorded at SRO, MAIO for 20 March 1976 event and 4 July 1976 explosion with same epicenter.

Fig. IV-12. M_S - m_b for 20 March 1976 event (point A) superimposed on Marshall and Basham's¹⁷ M_S - m_b data for Kazakhstan. Assuming 4 multiple events contribute to surfaces equally, M_S - m_b for each event moves to point B. Assuming average body-wave amplitude per event is 1.5 bigger than first event, M_S - m_b falls squarely on explosion trend line (point C).



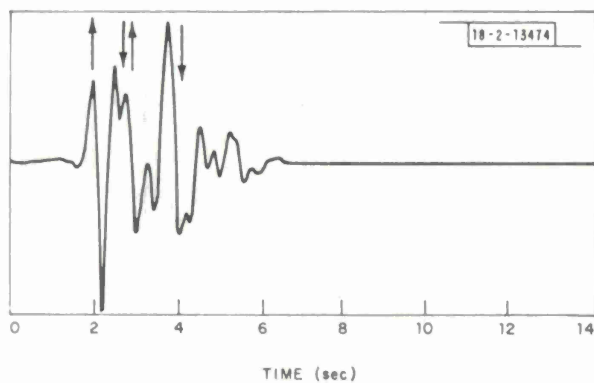
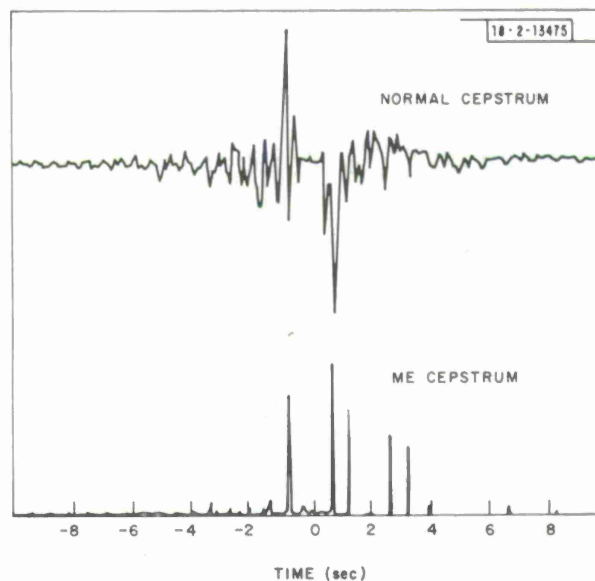


Fig. IV-13. First 4 sec of SP seismogram recorded at Yellowknife for 20 March 1976 event. Arrows indicate interpretation of cepstrum.

Fig. IV-14. Cepstrum of seismogram in Fig. IV-13 indicating two events, the second larger than the first and arriving about 0.9 sec later. Both depth phases are at approximately 0.8 sec, indicating very shallow (a kilometer or so) events.



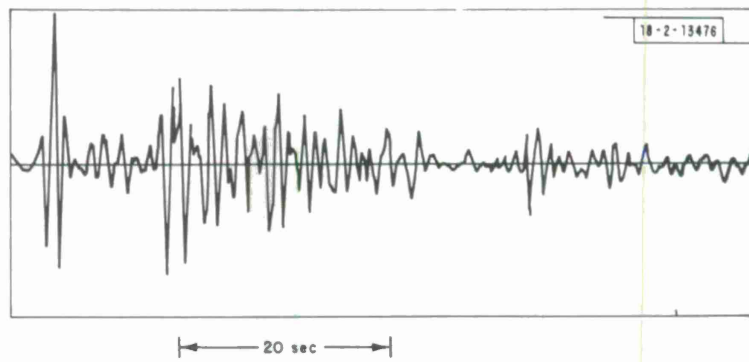


Fig. IV-15. Kurile Island event.

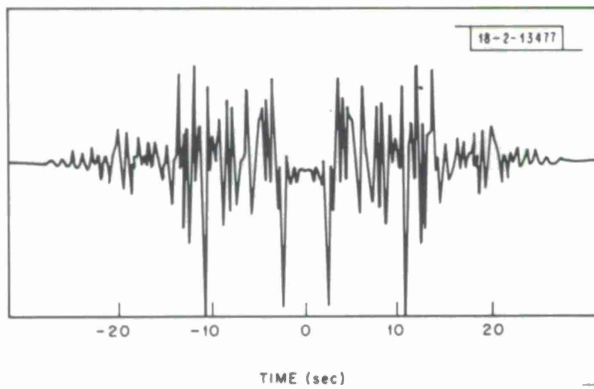


Fig. IV-16. Low-pass cepstrum of Kurile Island event.

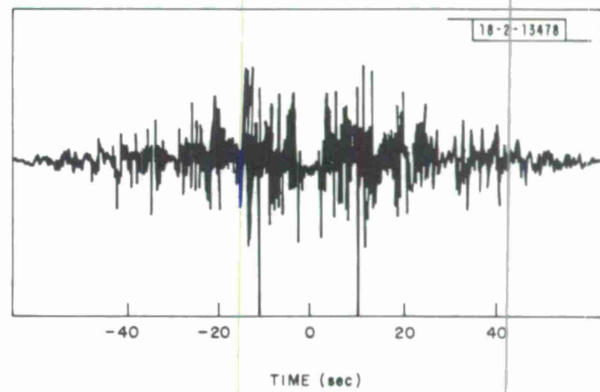


Fig. IV-17. Cepstrum of Kurile Island event.

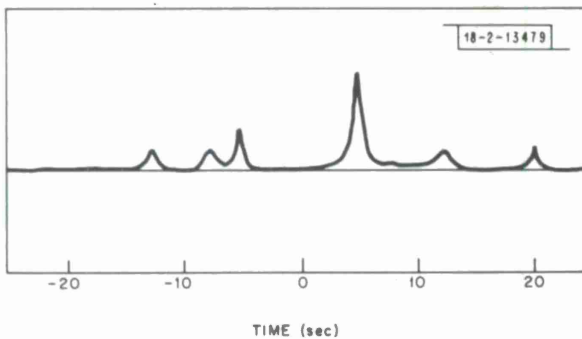


Fig. IV-18. MEM cepstrum of order 60.

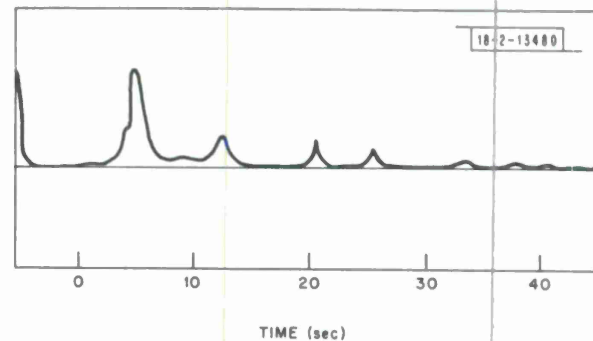


Fig. IV-19. Order 99 MEM cepstrum.

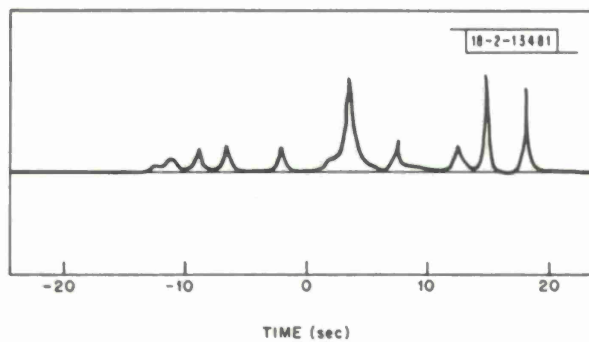


Fig. IV-20. ME cepstrum of pP portion only.

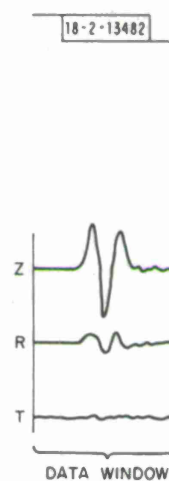
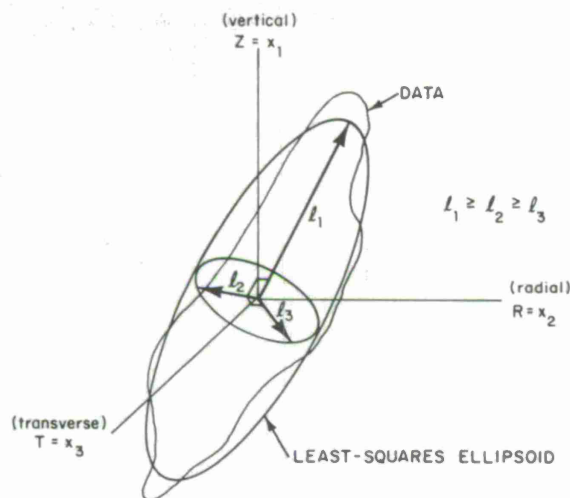


Fig. IV-21. Window of 3-component data and its corresponding particle-motion ellipsoid which is least-squares approximation to actual particle motion. Ellipsoid axes have lengths l_1 , l_2 , and l_3 , where l_1 is called principal component of data.

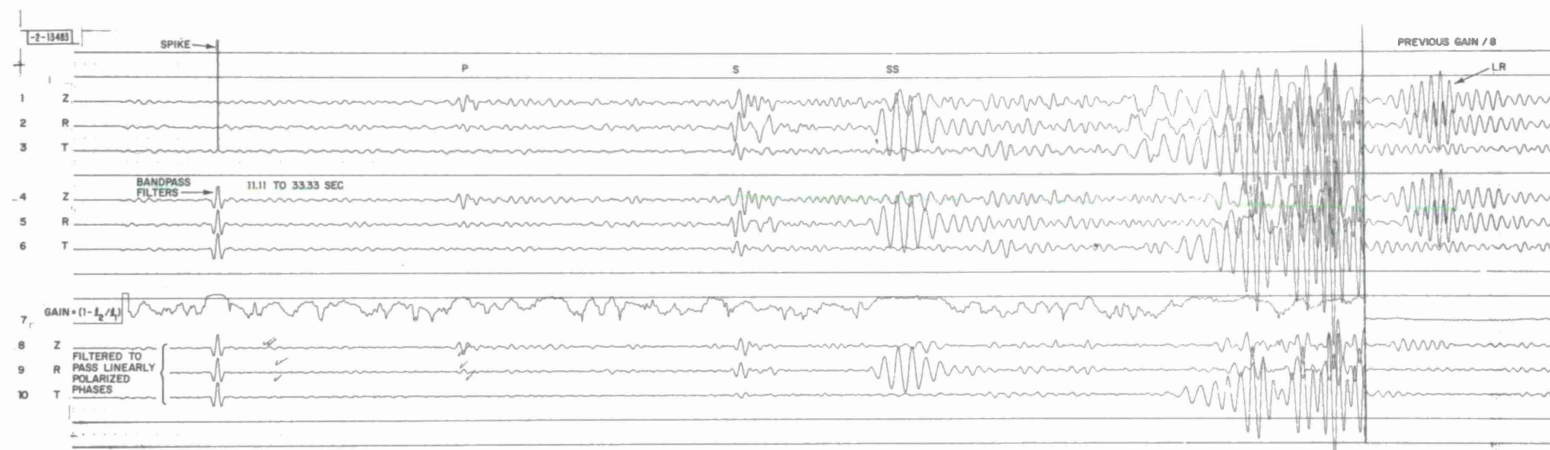


Fig. IV-22. Example of polarization filtering applied to an earthquake in Kuriles, mb 5.4, recorded at MAIO 66° away. Traces 1 to 3 are Z, R, and T components of unfiltered data beginning at origin time. Traces 4 to 6 are same components filtered to pass periods from 11.11 to 33.33 sec. Trace 7 is instantaneous gain factor used in polarization scheme. Traces 8 to 10 are polarized traces obtained by projecting principal component of ellipsoid onto data, scaled by gain factor.

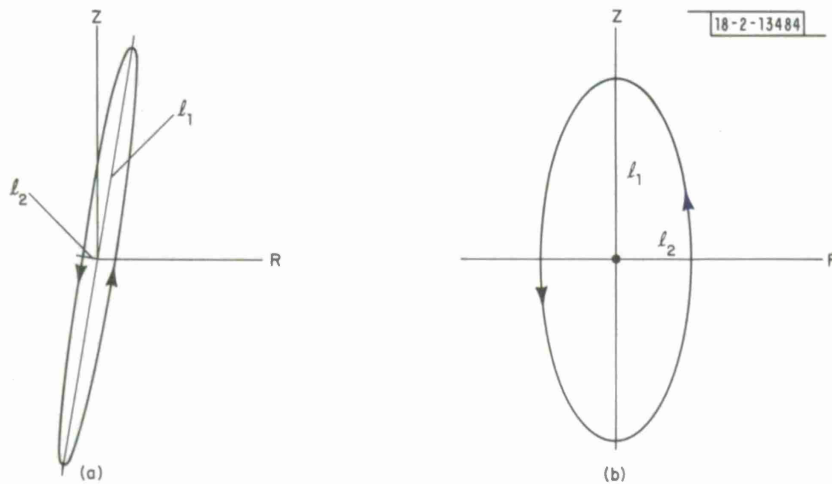


Fig. IV-23. Two-component particle motions for (a) idealized P waves and (b) Rayleigh wave. If R component of surface wave is Hilbert transformed, particle motion is changed from elliptically to linearly polarized. For P waves, motion is converted from linear to elliptical.

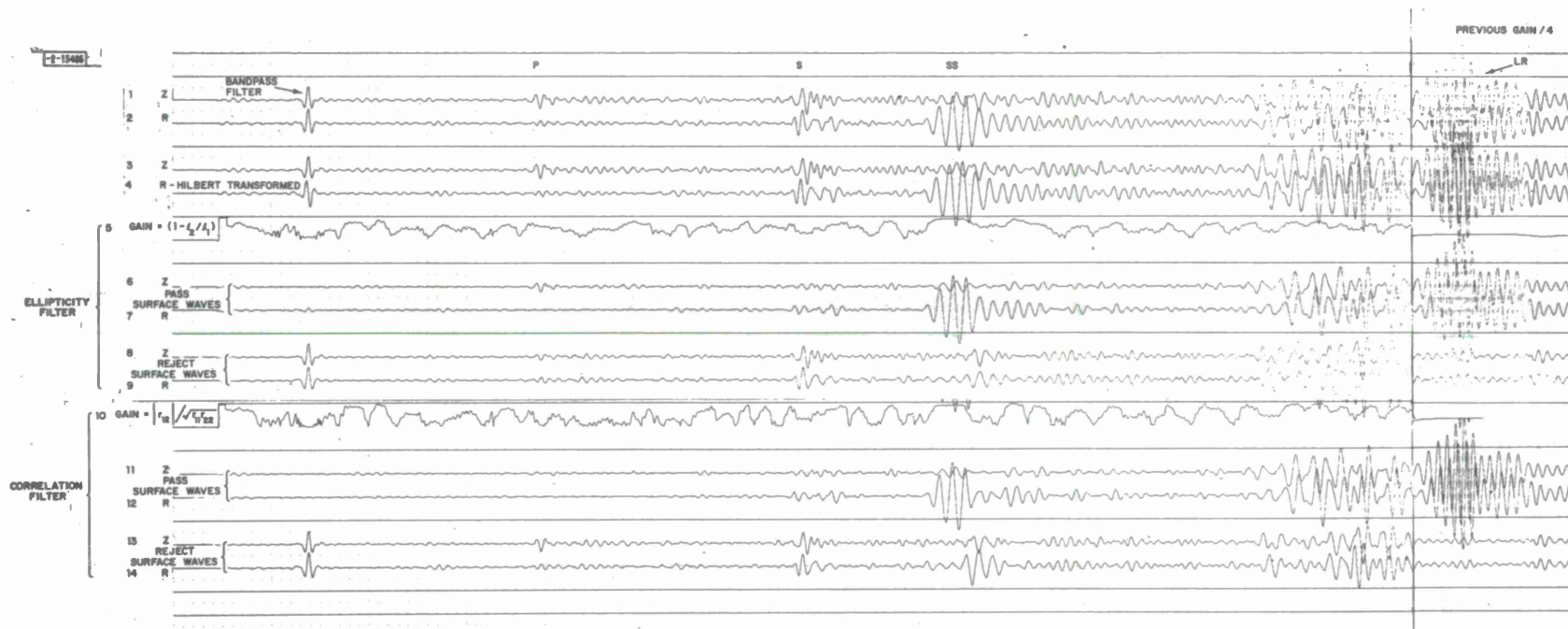


Fig. IV-24. Example of polarization filtering applied to two components Z and R of Fig. IV-22. Traces 1 and 2 are bandpassed components. Trace 4 is R component after being Hilbert transformed. Using a gain based on ellipticity only, trace 5, surface waves can be passed or rejected, as shown respectively by trace pairs 6 and 7, 8 and 9. An improved gain factor given by correlation coefficient, trace 10, produced better rejection of body waves in traces 11 and 12, while passing surface-wave motion. Traces 13 and 14 preserve body phases while surface waves are subtracted from data.

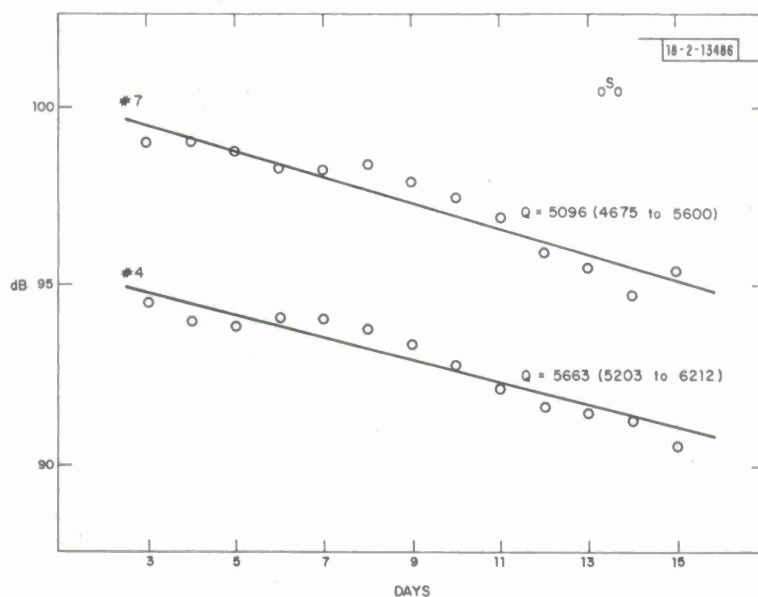


Fig. IV-25. Attenuation of $0S_0$ following 1964 Alaskan earthquake as observed on UCLA gravimeters #4 and #7. Each point represents power in decibels in a different 6-day window, centered at the value given on horizontal axis. Maximum value of power in first window (0 to 6 days) is given reference value of 100 dB. Range of Q given corresponds to plus-or-minus one standard deviation of $1/Q$ as obtained from regression.

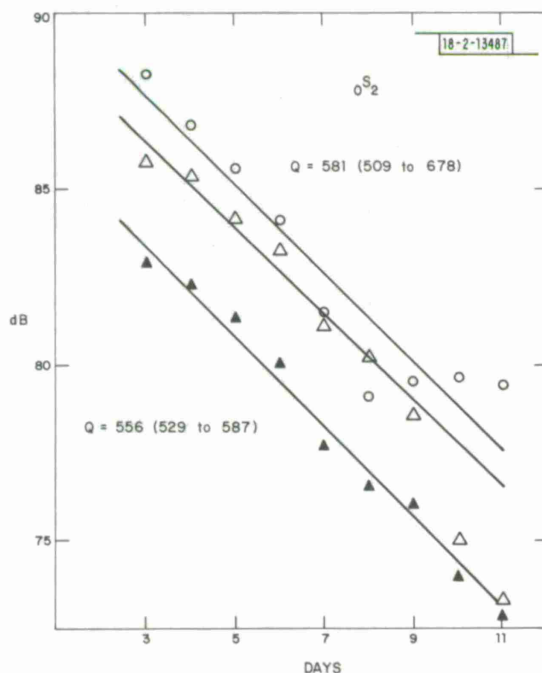


Fig. IV-26. Attenuation of $0S_2$ singlets and integrated multiplet on UCLA gravimeter #4. Q can be measured separately for two distinct peaks $0S_2^{-1}$ and $0S_2^{+1}$. For explanation, see text.

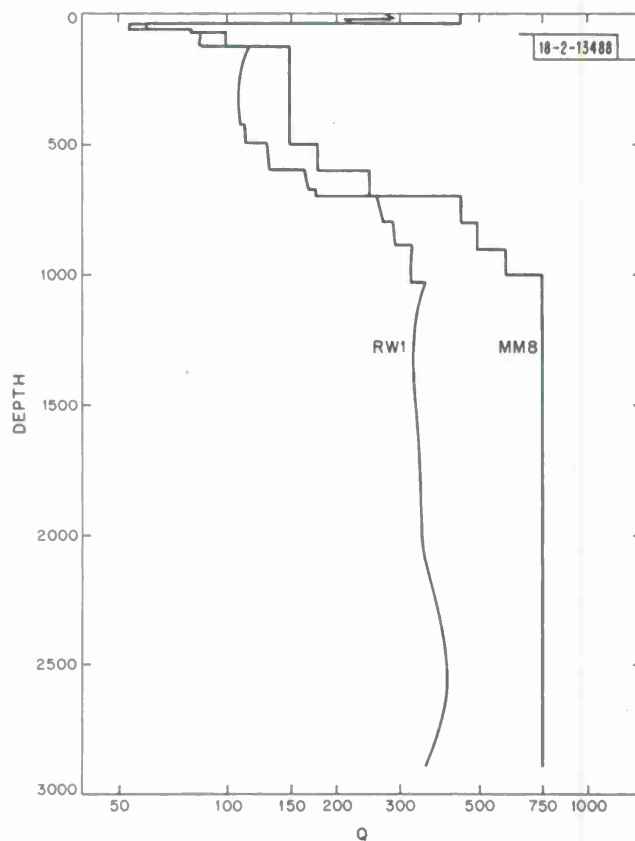


Fig. IV-27. Two Q_{μ} models of mantle, MM8 and RW1. Model MM8 of Anderson *et al.*³³ was used as a starting model in "ranking and winnowing" data-space inversion to obtain model RW1. We used observed values and corresponding standard errors for a representative set of 40 modes (3 toroidal, 7 radial, ${}_1S_7$, 8 high-Q overtones, and 21 ${}_0S_1$). Relative rms residual for model MM8 is 0.416; this was reduced to 0.196 for final model, RW1.

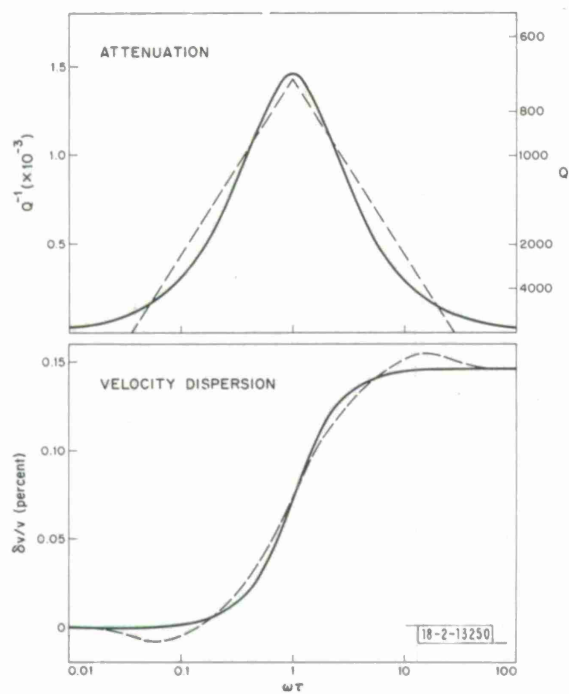


Fig. IV-28. Comparison of velocity dispersion associated with a "triangular" attenuation function and that due to an absorption-dispersion pair.⁴¹

Fig. IV-29. Velocity dispersion due to four attenuation functions. Note that dispersion curves corresponding to attenuation functions 1a and 1b as well as 2a and 2b are very similar, respectively.

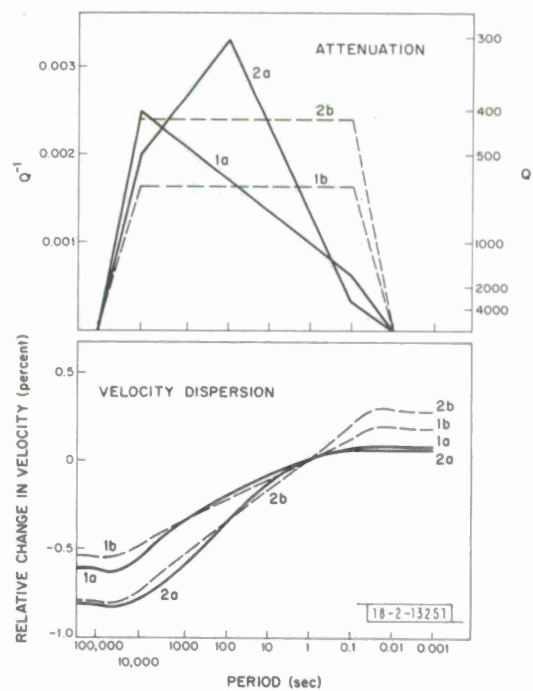


Fig. IV-30. Comparison of observed and computed travel times for P waves.

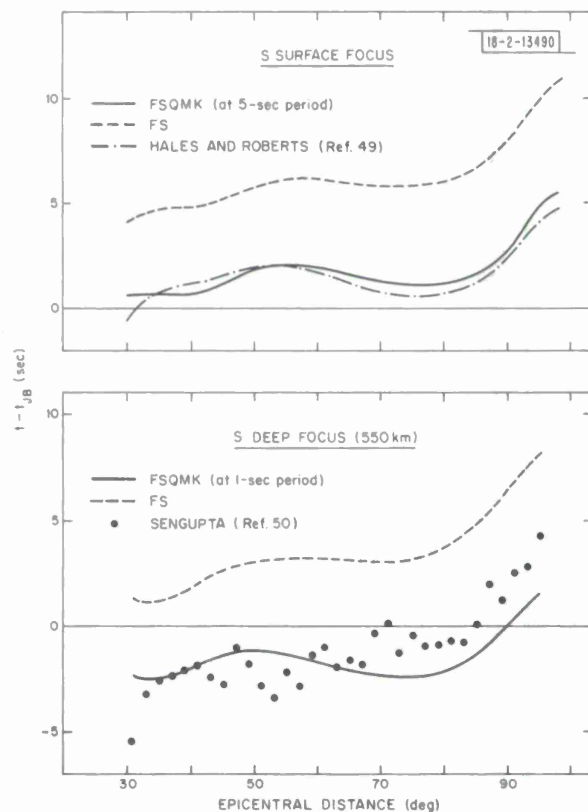
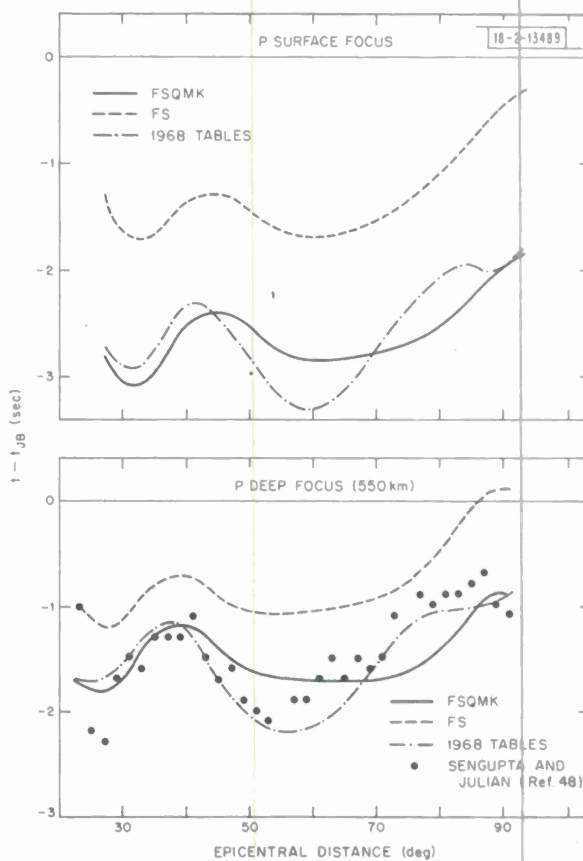


Fig. IV-31. Comparison of observed and computed travel times for S waves.

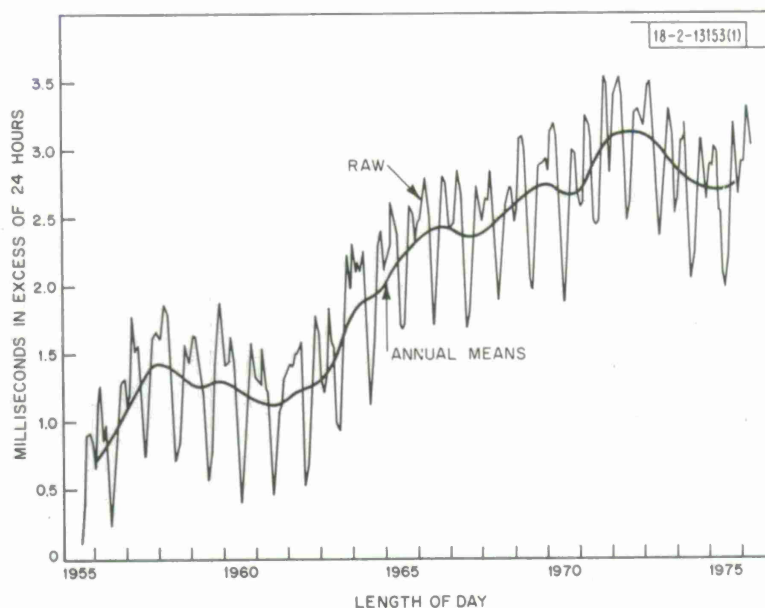


Fig. IV-32. Length of day from mid-1965 to mid-1976, plotted at 30-day intervals.

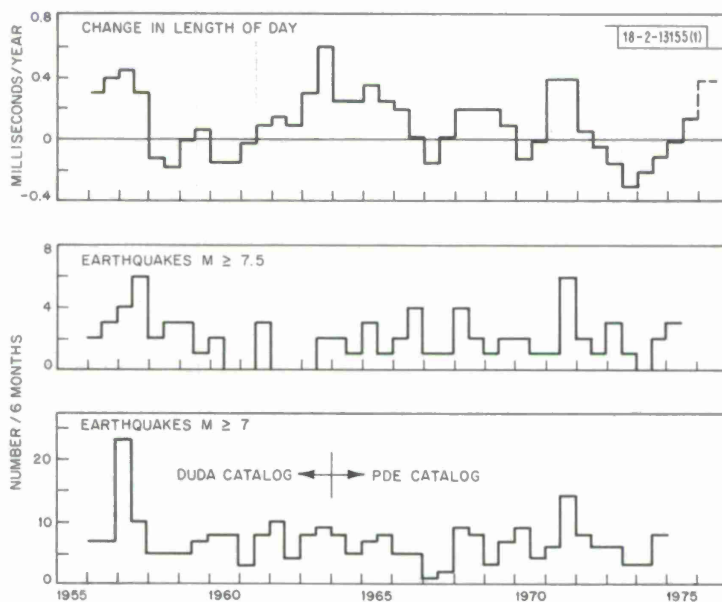


Fig. IV-33. Comparison of rate of change of length of day with counts of large earthquakes.

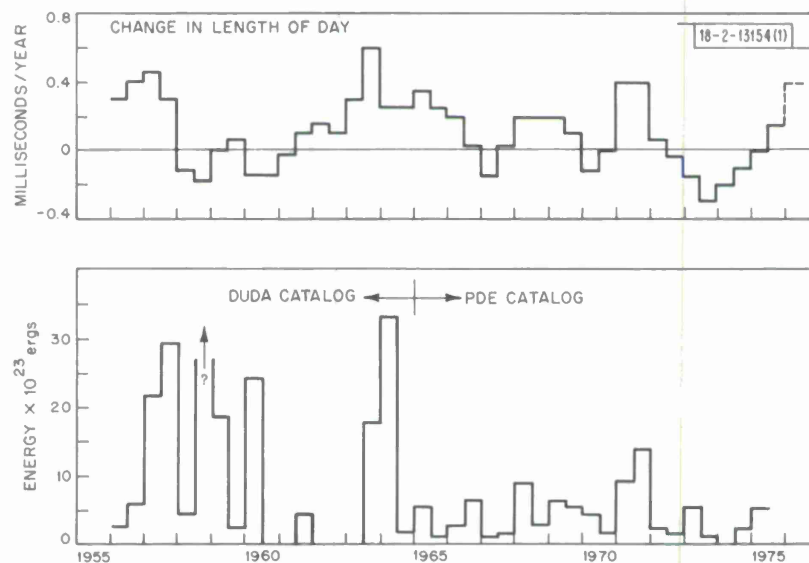


Fig. IV-34. Comparison of rate of change of length of day with seismic-energy release in 6-month intervals.

V. DATA SYSTEMS

A. PDP-11 COMPUTER FACILITY

The PDP-11 computer is presently configured as a time-sharing system running the UNIX operating system. The central processor is a PDP-11-50 with 112K words of memory. Also included in the configuration are a number of terminals, on-line and off-line data-storage facilities, a Versatec printer plotter, a card reader, a floating-point processor, and a connection to the ARPANET. Terminals include 4 Tektronix 4014 graphics terminals, 5 DEC VT52 video terminals, 5 DEC LA36 hard-copy terminals, and 1 Diablo typewriter terminal. Data-storage devices include 4 disk drives and 2 tape drives. There are two types of disk drives: two 40M-byte DIVA DD52 drives used for user file storage, and two 2.5M-byte DEC RK05 drives used for system storage and swapping. The tape drives include a 7- and a 9-track drive. This system supports a user community of about 40 people doing a variety of computer tasks. These tasks include some limited Fortran number-crunching programs, computer graphics in both Fortran and C, access to the ARPANET, and the development of user and system software.

In addition to normal software maintenance and the incorporation of externally acquired software into our system, there has been significant progress on our graphics software, our software to access the datacomputer, and our methods of locally dealing with SRO data. The following information is concerned with all these areas.

The UNIX graphics system is a device-independent user-oriented graphics system. It is designed to be implemented for a variety of devices ranging from Tektronix displays, to refresh scopes, to Versatec plotters. The device independence is accomplished through a universal graphics language (UGL) which is based on the network graphics protocol as described in the ARPANET Protocol Handbook. UGL allows the user to execute a set of graphics primitives which combine to form a display structure. The structure represents a graphics picture which can be manipulated with additional graphics primitives. The graphics primitives are implemented through a set of subroutines for both Fortran and C.

The basic conceptual building block of the UNIX graphics system is the picture segment. A picture segment is a logically related grouping of vectors, points, and character strings which represent a portion of the picture. A complete picture can therefore be thought of as one or more picture segments.

Manipulation of a picture is accomplished through the execution of a number of graphics primitives on individual picture segments. Segments may be created, destroyed, duplicated, translated, or scaled independently in x and y. They may also be displayed (posted) or kept hidden (unposted) in the actual picture being displayed. An unposted segment is still logically part of the picture, although it is not actually visible.

The manipulation of picture segments and the retention of the entire picture in a data file allow the user to change portions of a picture without recomputing the unchanged portions. In addition, the stored-picture data file also allows the user to move a created picture from one graphics device to another by simply moving the data file. A special command is provided which reads back the existing graphics data file from one device and sends it to another graphics device.

All the overhead of maintaining the picture data file and the manipulation of segments is done by a process separate from the user program. This frees the user from having to allocate and maintain storage space to support the graphics-picture file.

In some cases, there are special features associated with a graphics device which are not implemented in the hardware of the other devices, e.g., the multiple character sizes and the manipulation of a cursor on the Tektronix. We decided that these features should not be sacrificed for the sake of compatibility. The commands which implement these features are either simulated in software for the other devices or result in a warning message to the user's error file.

Graphics is implemented through the use of graphics daemons (free-running UNIX processes) which are always present in the system. Each graphics device has its own daemon which is responsible for maintaining the software overhead for that device. The user communicates with a graphics daemon through a set of subroutines which send graphics commands to the desired graphics daemon using UNIX interprocess as communication-channels called ports. Each daemon sets up an input and an output port during system initialization and makes them accessible to all users in the system. Each graphics subroutine sends a message over the port corresponding to a graphics command and its parameters. The graphics daemon receives the command messages and stores them in a display file. The display file is a structured file which, in addition to the graphics commands, maintains the information necessary to identify picture segments and their status. This is done with a picture-segment table containing pointers to buffers of device-dependent graphics commands and with flags indicating the status of each segment. The display file also contains the x and y translation and scaling for each picture segment. The paint command causes the graphics daemon to transform the display file into device-dependent commands, and to transmit these commands to the appropriate graphics device.

The currently implemented graphics system is limited to Tektronix graphics. Work on a Versatec plotter is about 70-percent complete. There are no plans to implement the graphics system for any other specific devices at the present time, although the design does allow for future expansion.

Our basic access to the datacomputer is presently by means of DCI, which is a new program that provides a convenient terminal interface between our local UNIX system and the datacomputer. This program was designed to work in either of two basic situations:

- (1) The user has a prepared datalanguage "program" which he wishes to transmit to the datacomputer with a minimum of effort.
- (2) The user wishes to work with the datacomputer in an interactive manner, such as when he is trying out new sequences of datalanguage.

Some of the main features of DCI are summarized in the following paragraphs.

The datacomputer sends the user a great variety of messages. Because of the large volume of these messages, DCI allows the user to choose between three different verbosity levels: under FULL, all messages will be typed out; under NORMAL, only error messages and urgent informational messages will be output; and under SILENT, all messages will be suppressed.

When the user has a sequence of datalanguage and DCI commands that will be used frequently, he may create a UNIX file that contains these commands, and then direct DCI to take its input from this file. A command file may also contain comment lines and references to other command files up to three levels of nesting. Another verbosity level, called MONITOR, will cause each line from the command file to be typed out on the user's terminal as it is processed by DCI.

Using DCI, data may be transferred in either direction between the datacomputer and a UNIX file, using either the default datalanguage connection or a separate data connection. The user

may establish a separate connection by specifying only the direction of transfer, the byte size, and the datacomputer port involved. DCI handles the details of selecting a socket number and informing the datacomputer of the connection.

DCI will write all messages and commands, regardless of verbosity level, to a file called `dc1.script`. This will provide the user with a complete record of his datacomputer session. This record is easily discarded if it is not needed by the user, but is an invaluable source of information when there are problems in a transaction.

While DCI is running, the user may request status information which will include what state the program is in, what separate connections exist (if any), and, if data are being transferred, the elapsed time of the transfer and the number of bytes that have been passed. The user may also return to the UNIX shell and edit command files or inspect the script file before returning to DCI.

The third item to discuss is our local handling of SRO data. Much of our SRO data and some other seismic data are currently on magnetic tape in waveform data unit format. The format assigns a tape file to each seismogram. The file contains the seismogram plus alphanumeric information describing the seismogram. As discussed in our previous SATS, this tape format is quite general and is the primary medium for the transfer of waveform data between our PDP-7 and PDP-11 systems. Two PDP-11 programs have now been written to exchange data on such tapes with a waveform database which can be kept in the UNIX system. Within UNIX, the individual seismograms continue to reside in separate files, but the alphanumeric information is combined into a single index file on the disk. That file contains the identification information from the waveform data unit tape plus the UNIX file names of the files containing the actual seismograms. The seismograms themselves are stored as binary floating-point numbers.

The two programs which have been written are DUREAD and DUWRITE. DUREAD reads all or part of a waveform data unit tape and either adds the data to an existing database or will create a new one. On input, data are converted from binary-gain-ranged or 18-bit binary integers into PDP-11 floating point. The DUWRITE program outputs all of a specified database onto a waveform data unit tape. All alphanumeric information will be preserved but the representation of data samples is modified from floating-point to 16-bit integer format on the tape, so the user must take care to avoid having sample values which are too large. These programs are temporary until more sophisticated ones can be developed.

L. J. Turek
J. Sax

B. INTERACTIONS WITH THE DATACOMPUTER

We have started to use our datacomputer interface program DCI to store data on the datacomputer and to fetch data from it. Three current applications of DCI are described in this section. Other applications are being developed, as are alternative software modules to fetch and store data.

The ISC seismic bibliography for the years 1965-1973 has been stored on the datacomputer under the `seismic.lincoln.biblio` node. This database contains information about 14,230 published seismic works: accession number, title, journal/publisher code, volume, number, year, page, authors, and keywords. The file is inverted on keyword value and author surname so that searches involving these items will be optimized. A local UNIX program, LOOKUP, will use DCI to connect to the datacomputer, log into the biblio node, and open the appropriate files and

output ports. When initialization is complete, it will accept any user lookup requests that can be expressed in datalanguage. When the results are received, the output may be typed out on the user's terminal or written into a UNIX file.

There now exists in the datacomputer a preliminary event summary file (PESF) containing event locations obtained by using the large arrays, and selected SP stations. The PESF file is updated frequently and is about 7 to 8 weeks behind real time for bulletin listings. These preliminary epicenters are very useful to us for determining the time periods of interest for the SRO digital data. The PESF file is created and maintained by the Seismic Data Analysis Center and is suitably protected against unauthorized access. On a routine basis, we read data from the PESF files and transfer the data into our UNIX system. There is a small amount of re-formatting that occurs during transfer between the mass store and UNIX. Once the data are within UNIX, they are reformatted again and additional information such as geographic region name and seismic region name is added to the list. The files are then divided into monthly periods and maintained on-line for immediate local access.

The International Seismological Center (ISC) also makes available computer tapes containing event lists and the individual reports from stations for these events. This is a large database which is difficult to use because of its size and the complexities and variabilities of its formats. We are currently in the process of storing these data on the datacomputer for the time period 1964 to 1973. The event information is already entered, and the supporting station data are now being entered. When these data are entered, they can be of use to all members of our group with greater convenience than would be possible were the data kept on tape or in some other computer system with a large amount of disk storage.

The datalanguage file description for the ISC epicenter database has several inverted containers. Some of the inverted containers are year, magnitude, hemisphere, and geographic region numbers along with a few other pointers, including a sequence-number counter. The corresponding event station readings are loaded into a second database, one file per year. Since each event has a sequence number, this number is carried over into the station-reading database. This event number is the pointer from one file into the other. The ten station-readings files have identical format descriptions, thus enabling a user to treat them as a group (a special datacomputer feature) when performing searches on this database. The volume of data contained within the station-readings file is far greater than the data contained in the epicenter file. The average number of readings per year in the station-readings file is over 400,000. The total volume of bits stored for the station readings will eventually exceed 1400 megabits for the 10-year database. Some of the containers that are inverted in the station-readings list are station name, phase code, and event number. This event number is the pointer back into the event database for the correct event parameters that are associated with the station reading.

R. M. Sheppard
L. J. Turek

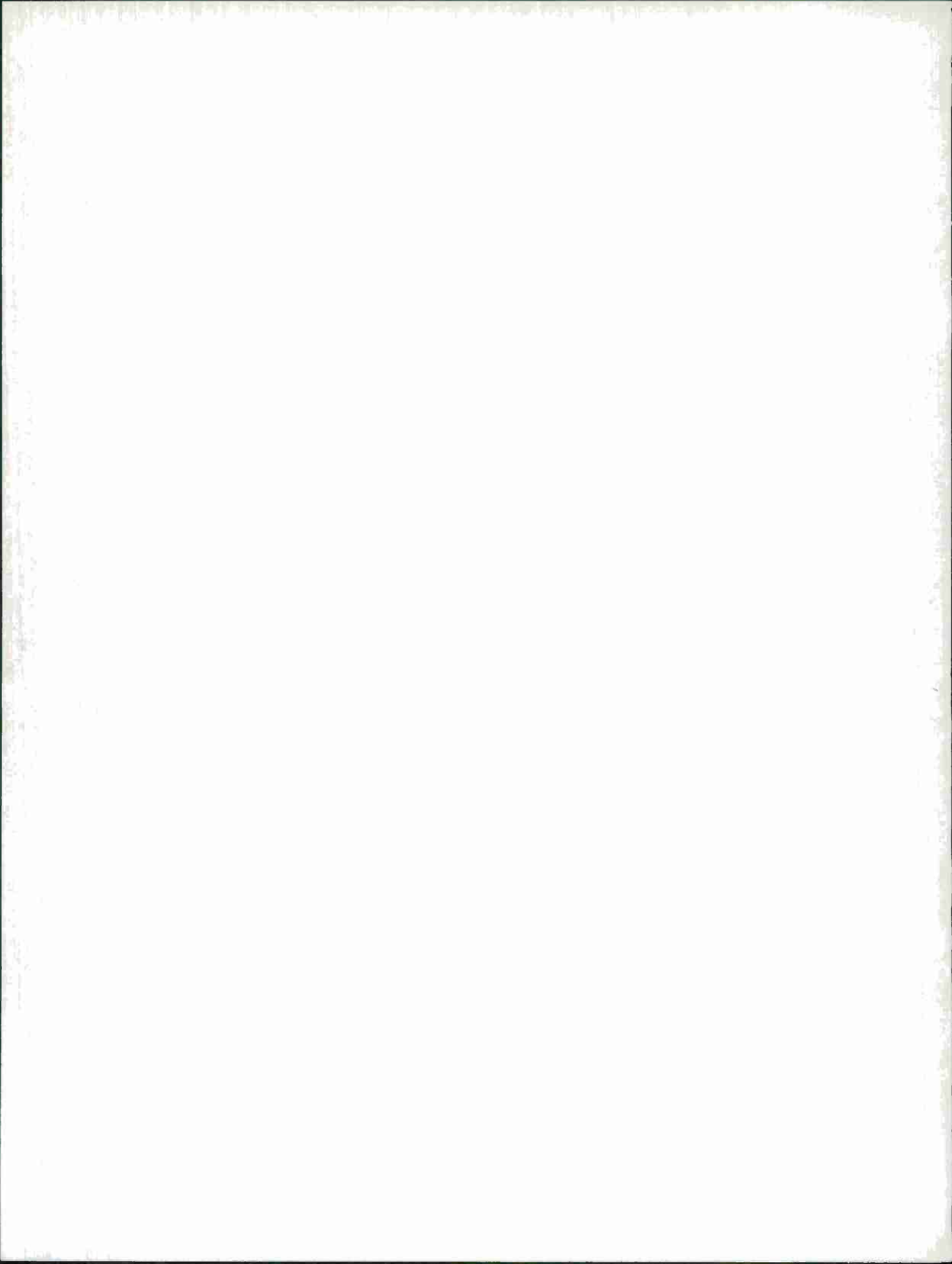
VI. PUBLICATIONS LIST

The following list contains an update to the Seismic Discrimination publications list printed in the 31 December 1975 SATS (DDC AD-A025777/4).

Requests for these reports or reprints should be addressed to:

The secretary
Lincoln Laboratory Group 22
42 Carleton Street
Cambridge, MA 02142

151. Seismic Discrimination Semiannual Technical Summary, Lincoln Laboratory, M.I.T. (31 December 1975), DDC AD-A025777/4.
152. T. J. Fitch and J. M. W. Rynn, "Inversion for V_P/V_S in Shallow Source Regions," *Geophys. J. R. Astr. Soc.* 44, 253-267 (1976).
153. D. W. McCowan, "Moment Tensor Representation of Surface Wave Sources," *Geophys. J. R. Astr. Soc.* 44, 595-599 (1976), DDC AD-A037625.
154. K. Aki, A. Christoffersson, and E. S. Husebye, "Three-Dimensional Seismic Structure of the Lithosphere under Montana LASA," *Bull. Seismol. Soc. Am.* 66, 501-524 (1976), DDC AD-A028458/8.
155. P. G. Richards and C. W. Frasier, "Scattering of Elastic Waves from Depth-Dependent Inhomogeneities," *Geophysics* 41, 441-458 (1976).
156. R. T. Lacoss and A. F. Shakal, "More $A_1E + EA_2 = -D$ and $\dot{X} = A_1X + XA_2 + D, X(0) = C$," *IEEE Trans. Automat. Contr.* AC-21, 405-406 (1976), DDC AD-A029287/0.
157. M. K. Sengupta and B. R. Julian, "P-Wave Travel Times from Deep Earthquakes," *Bull. Seismol. Soc. Am.* 66, 1555-1579 (1976).
158. R. G. North and A. M. Dziewonski, "A Note on Rayleigh-Wave Flattening Corrections," *Bull. Seismol. Soc. Am.* 66, 1873-1879 (1976).
159. R. J. O'Connell and A. M. Dziewonski, "Excitation of the Chandler Wobble by Large Earthquakes," *Nature* 262, 259-262 (1976).
160. A. M. Dziewonski and R. V. Sailor, "Comments on 'The Correction of Great Circular Surface Wave Phase Velocity Measurements From the Rotation and Ellipticity of the Earth' by F. A. Dahlen," *J. Geophys. Res.* 81, 4947-4950 (1976), DDC AD-A037624.
161. Seismic Discrimination Semiannual Technical Summary, Lincoln Laboratory, M.I.T. (30 June 1976), DDC AD-A032754/4.
162. A. M. Dziewonski, B. H. Hager, and R. J. O'Connell, "Large-Scale Heterogeneities in the Lower Mantle," *J. Geophys. Res.* 82, 239-255 (1977).
163. K. Aki, A. Christoffersson, and E. S. Husebye, "Determination of the Three-Dimensional Seismic Structure of the Lithosphere," *J. Geophys. Res.* 82, 277-296 (1977).
164. D. W. McCowan, P. Glover, and S. S. Alexander, "A Static and Dynamic Finite Element Analysis of the 1971 San Fernando, California Earthquake," *Geophys. J. R. Astr. Soc.* 48, 163-185 (1977).
165. R. G. North, "Seismic Moment, Source Dimensions, and Stresses Associated with Earthquakes in the Mediterranean and Middle East," *Geophys. J. R. Astr. Soc.* 48, 137-161 (1977).
166. T. E. Landers and R. T. Lacoss, "Some Geophysical Applications of Autoregressive Spectral Estimates," *IEEE Trans. Geosci. Electron.* GE-15, 26-32 (1977).



GLOSSARY

A-D	Analog to Digital
ALPA	Alaska Long-Period Array
ARPANET	DARPA Computer Network
DCI	Datacomputer Interface
DEC	Digital Equipment Corporation
DSS	Deep Seismic Sounding
FFT	Fast Fourier Transform
GMT	Greenwich Mean Time
IFFT	Inverse Fast Fourier Transform
ISC	International Seismological Center
J-B	Jeffreys-Bullen (Tables)
LASA	Large Aperture Seismic Array
LP	Long Period
LRSM	Long Range Seismic Measurements
MEM	Maximum Entropy Method
MESA	Maximum Entropy Spectral Analysis
NEIS	National Earthquake Information Service
NORSAR	Norwegian Seismic Array
NTS	Nevada Test Site
PDE	Preliminary Determination of Epicenters
PEM	Parametric Earth Model
PESF	Preliminary Event Summary File
SATS	Semiannual Technical Summary
S. D.	Standard Deviation
SNR	Signal-to-Noise Ratio
SP	Short Period
SPZ	Short Period, Vertical Component
SRO	Seismic Research Observatory
UCLA	University of California at Los Angeles
UGL	Universal Graphics Language
USGS	U.S. Geological Survey
WWSSN	World-Wide Standard Seismograph Network

UNCLASSIFIED

SECURITY CLASSIFICATION OF THIS PAGE (When Data Entered)

REPORT DOCUMENTATION PAGE		READ INSTRUCTIONS BEFORE COMPLETING FORM
1. REPORT NUMBER ESD-TR-77-71	2. GOVT ACCESSION NO.	3. RECIPIENT'S CATALOG NUMBER
4. TITLE (and Subtitle) Seismic Discrimination		5. TYPE OF REPORT & PERIOD COVERED Semiannual Technical Summary 1 July 1976 - 31 March 1977
		6. PERFORMING ORG. REPORT NUMBER
7. AUTHOR(s) Michael A. Chinnery		8. CONTRACT OR GRANT NUMBER(s) F19628-76-C-0002
9. PERFORMING ORGANIZATION NAME AND ADDRESS Lincoln Laboratory, M. I. T. P. O. Box 73 Lexington, MA 02173		10. PROGRAM ELEMENT, PROJECT, TASK AREA & WORK UNIT NUMBERS Program Element No. 62701E Project No. 7F10
11. CONTROLLING OFFICE NAME AND ADDRESS Defense Advanced Research Projects Agency 1400 Wilson Boulevard Arlington, VA 22209		12. REPORT DATE 31 March 1977
		13. NUMBER OF PAGES 138
14. MONITORING AGENCY NAME & ADDRESS (if different from Controlling Office) Electronic Systems Division Hanscom AFB Bedford, MA 01731		15. SECURITY CLASS. (of this report) Unclassified
		15a. DECLASSIFICATION DOWNGRADING SCHEDULE
16. DISTRIBUTION STATEMENT (of this Report) Approved for public release; distribution unlimited.		
17. DISTRIBUTION STATEMENT (of the abstract entered in Block 20, if different from Report)		
18. SUPPLEMENTARY NOTES None		
19. KEY WORDS (Continue on reverse side if necessary and identify by block number)		
seismic discrimination seismic array seismology	surface waves body waves LASA	NORSAR ARPANET
20. ABSTRACT (Continue on reverse side if necessary and identify by block number)		
<p>This report describes 31 investigations in the field of seismic discrimination. These are grouped as follows: body-wave studies (6 contributions), surface-wave studies (5 contributions), studies of long- and short-period magnitude, explosion yield, and seismic energy (9 contributions), miscellaneous studies (9 contributions), and recent developments in our data and computer systems (2 contributions).</p>		

DD FORM 1473 EDITION OF 1 NOV 65 IS OBSOLETE
1 JAN 73

UNCLASSIFIED

